

**Low-Energy Physical Properties  
of Edge States in Nano-Graphites**

**Katsunori Wakabayashi**

**Doctoral Program in Engineering**

**University of Tsukuba**

**March 2000**



In this thesis, I present the low-energy physical properties of edge states in nano-graphites. Nanographite is a new class of mesoscopic systems which is situated between aromatic molecules and bulk graphites. In nanosize carbon systems, the topology of  $sp^2$  carbon networks crucially affect their  $\pi$  electronic states which govern the electronic properties near the Fermi level. In this thesis, I emphasize that the presence of edges and their shapes play an important role in the electronic, magnetic and transport properties of nanographites.

The works presented in this thesis have been done in four years from the summer of 1995 to the summer of 1999, and partially published in the following publications. Therefore, I did not include the recent advances concerning the transport properties of nanographite such as double-barrier problem and weak disorder problems. However, the results presented here are sufficient to recognize the importance of the presence of edges and their shapes for the low-energy physics of nanographites.

- K. Wakabayashi, and M. Sigrist,  
*Zero-Conductance Resonances due to Flux States in Nanographite Ribbon Junctions*,  
Phys. Rev. Lett., in press, cond-mat/9907212.
- K. Wakabayashi, M. Fujita, H. Ajiki, and M. Sigrist  
*Electronic and Magnetic Properties of Nanographite Ribbons*,  
Phys. Rev. B **59**, 8271-8282 (1999).
- K. Wakabayashi, M. Sigrist, and M. Fujita,  
*Spin Wave Mode of Edge-Localized Magnetic States in Nanographite Zigzag Ribbons*,  
J. Phys. Soc. Jpn. **67**, 2089-2094 (1998).
- M. Fujita, K. Wakabayashi, K. Nakada, and K. Kusakabe,  
*Peculiar Localized State at Zigzag Graphite Edge*,  
J. Phys. Soc. Jpn. **65**, 1920-1923 (1996).

Here I would like to express my thanks. I am deeply indebted to Manfred Sigrist, who has supervised my thesis with great attention and diligence, for teaching me a scientific research style, for his availability for long hours of debate, for his expertise in writing. I also express my sincerest for late Mitsutaka Fujita, who introduced me to the new and interesting field of condensed matter physics, nanoscopic carbon systems.

I am also indebted to Prof. Koichi Kusakabe and Prof. Hiroshi Ajiki for their long-term collaboration and long-hours discussion. I also would like to thank my colleagues, Masatsura Igami, Kyoko Nakada, Susumu Okada, and Yoshiteru Takagi for long-term collaboration and helpful discussions.

I would like to also thank Prof. Toshiaki Enoki and Prof. Chuhei Oshima for many helpful discussions concerning the experiments of nanographite systems. I also thank Atsuko Nakayama, B. L. V. Prasad, and Yoshiyuki Shibayama for detail discussions concerning activated carbon fibers and nanographites.

My thanks also go to the people of the Yukawa Institute for Theoretical Physics, Kyoto University, the colleagues in the Condensed Matter Theory Group, Institute of Materials Science, University of Tsukuba, and the people at the Institute for Theoretical Physics, Eidgenössische Technische Hochschule (ETH), Zürich, Switzerland.

I am also very grateful to Prof. Kenji Nakao, Prof. Takahisa Arima, Prof. Koki Takita, Prof. Hirokazu Tsunetsugu for examining the present thesis and giving valuable suggestions. I acknowledge Prof. Riichiro Saito, Dr. Kikuo Harigaya, Dr. Hidefumi Hiura, and Dr. Mitsuho Yoshida for sending me some references and help for my numerical works. I acknowledge the financial support of the Japan Society for the Promotion of Science for Young Scientist.

I wish to thank my parents and sisters and brothers for their continual encouragement and support throughout my education.

*Katsunori Wakabayashi*  
*January, 2000*  
*Kyoto*



# Contents

<b>1</b>	<b>From Graphite to Nanographite</b>	<b>1</b>
1.1	Nanosize Carbon Systems with Closed Boundary . . . . .	1
1.2	Nanosize Carbon Systems with Open Boundary . . . . .	3
1.2.1	Edge states . . . . .	3
1.2.2	Nanographites . . . . .	7
1.3	Nanographite Systems . . . . .	8
1.3.1	Activated Carbon Fibers . . . . .	8
1.3.2	Graphitized Nano-diamonds . . . . .	9
1.3.3	Technological application of nano-graphites . . . . .	10
1.4	Synthesis of Nanographite Ribbons . . . . .	10
1.5	The Organization of this Thesis . . . . .	12
<b>2</b>	<b>Electronic States</b>	<b>13</b>
2.1	Tight Binding Model in a Magnetic Field . . . . .	13
2.1.1	Harper's equation . . . . .	15
2.1.2	The $\mathbf{k} \cdot \mathbf{p}$ equation . . . . .	16
2.2	Edge States . . . . .	17
2.3	Energy Gap . . . . .	18
2.4	Graphene Sheet in a Magnetic Field . . . . .	20
2.4.1	Harper's equation approach . . . . .	20
2.4.2	$\mathbf{k} \cdot \mathbf{p}$ equation approach . . . . .	21
2.5	Graphene Ribbon in Magnetic Field . . . . .	22
2.5.1	Edge states in a magnetic field . . . . .	25
2.6	Bearded Edge and Cove Edge . . . . .	26
2.7	$\mathbf{k} \cdot \mathbf{p}$ Theory . . . . .	27
2.7.1	Solutions with the translational symmetry of zigzag axis . . . . .	28
2.7.2	Envelope functions on graphite ribbons . . . . .	29
2.8	Connection with Anisotropic Superconductivity . . . . .	32
2.8.1	Bound states at [110]-surface of $d_{x^2-y^2}$ -wave superconductor . . . . .	32
2.8.2	Graphite as an odd-parity superconductor . . . . .	34
2.9	Summary . . . . .	35
<b>3</b>	<b>Magnetic Properties</b>	<b>37</b>
3.1	Orbital Diamagnetism and Pauli Paramagnetism . . . . .	37
3.2	Orbital Magnetization and Susceptibility . . . . .	37
3.2.1	Large orbital diamagnetism of graphene sheet . . . . .	38
3.2.2	Orbital diamagnetism of graphene ribbons . . . . .	39
3.3	Pauli Paramagnetism . . . . .	41
3.4	Magnetic Instability . . . . .	42
3.4.1	Mean field treatment in graphite ribbons . . . . .	42
3.4.2	Spin wave mode in graphite ribbons . . . . .	45
3.5	Summary and Discussion . . . . .	47

<b>4</b>	<b>Transport Properties</b>	<b>49</b>
4.1	Multi-Channel Landauer Formula . . . . .	49
4.1.1	Zigzag ribbon as a lead line . . . . .	50
4.1.2	The scattering problem . . . . .	51
4.1.3	Recursive relation of the Green function . . . . .	53
4.2	Single-Barrier Nanographite Ribbon Junctions . . . . .	53
4.2.1	Design of single-barrier nanographite ribbon junctions . . . . .	53
4.2.2	Fermi energy dependence of conductance . . . . .	55
4.2.3	Behavior of electron waves . . . . .	57
4.2.4	Flux states and large induced current vortex . . . . .	58
4.2.5	Origin of the zero-conductance resonance . . . . .	62
4.2.6	Negative magneto-resistance . . . . .	65
4.3	Effects of Single Non-magnetic Impurity or a Lattice Vacancy . . . . .	66
4.3.1	Single non-magnetic impurity in graphene sheet . . . . .	66
4.3.2	Influence on transport properties . . . . .	67
4.4	Summary . . . . .	68
<b>5</b>	<b>Conclusions and Outlooks</b>	<b>69</b>

---

## Chapter 1

# From Graphite to Nanographite

---

In this chapter, I present an overview on various graphite-related materials. The graphite-related materials have a long scientific, technological and industrial history. The recent discovery of fullerene molecules and carbon nanotubes has opened the door to new physics of nanometer-sized carbon systems. In these systems, the network topology of  $sp^2$  carbon atoms plays crucial roles in their electronic, magnetic and transport properties. Besides nano-size carbon systems with closed boundaries, I will emphasize the importance of the presence of edges and their shapes in nano-size carbon systems, based on graphene<sup>1</sup> ribbon models.

### 1.1 Nanosize Carbon Systems with Closed Boundary

Carbon-related materials<sup>2</sup> are surely important from industrial and scientific viewpoints, and we can also say that carbon materials are the most familiar materials for human being, because they have existed as soot, charcoal, activated carbon, graphite, diamond and so on. For a long time, many people have studied carbon related materials in order to improve our daily life, beginning in 18th century. The original purpose of these studies on carbon-related materials, especially activated carbons, is for the purification and refinement of materials. It is also owing to the development and improvement of activated carbons that we can now easily obtain safe and clean drinkable water. The research and development of new types of carbon fibers is carried out in many companies and universities, because of their technological importance. Carbon fibers/resin composites have strength-to-weight properties superior to those of any other materials. This property has brought a revolution in aircraft design. Since this makes it possible to reduce the weight of vehicles, modern civilian and military aircraft are increasingly using carbon fiber composites in all but their main structural components. Recently developed carbon fibers show high charge-discharge properties, which are useful for the development of Li-battery. This aspect has brought us very small and light portable electronic tools. Thus, carbon-related materials have many functionalities, and are technologically important. However, the microscopic origin of these various functionalities is still not clear, because these systems have very disordered structures. One assumes that carbon fibers, activated carbon and so on consist of the ensembles of graphite fragments, where fragment sizes are ranging from nano-meter up to micro-meter. The variety of functionalities of carbon related materials might very likely originate from this structural variety.

The structural variety of carbon related materials originates from many possible ways of hybridization of atomic orbitals of carbon. Carbon is the sixth element of the periodic table and is listed at the top of column IV. Each carbon atom has six electrons which occupy  $1s^2$ ,  $2s^2$  and  $2p^2$  atomic orbitals. The  $1s^2$ -orbital has two strongly bound electrons. However, the four electrons which occupy  $2s^2 2p^2$  orbitals are weakly bound electrons. These electrons play an important role in forming covalent bonds in carbon materials. Since the energy difference between the upper  $2p$  energy levels and the lower  $2s$  level in carbon is small compared with the binding energy of the chemical bonds, the electronic wave functions for these four electrons can readily mix with each other, thereby changing the occupation of the  $2s$  and three  $2p$  atomic orbitals so as to enhance the binding energy of the carbon atom with its neighboring atoms. This mixing of  $2s$  and  $2p$  atomic orbitals is called hybridization. The mixing of a single  $2s$  electron with  $n = 1, 2, 3$   $2p$  electrons is called  $sp^n$  hybridization. From

---

<sup>1</sup>One layer of graphite is called “graphene”, and the stack of graphenes is called “graphite”.

<sup>2</sup>As reviews of this section, see references [1–12].

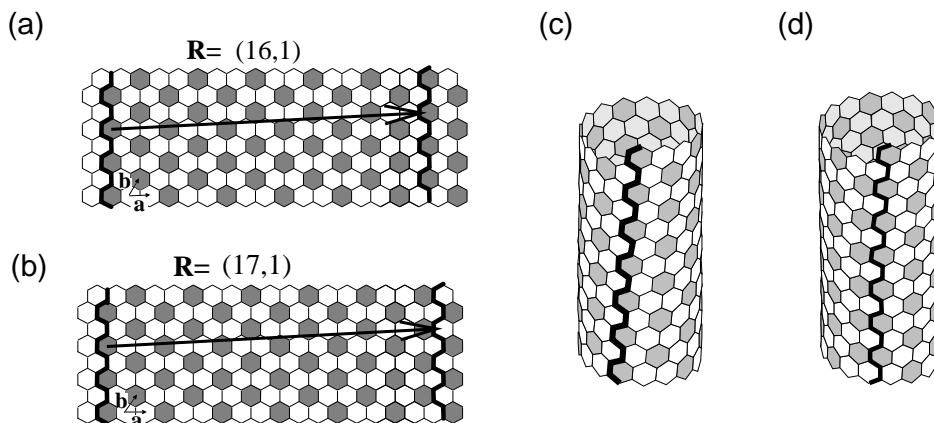


Figure 1.1: The development map of carbon nanotube of (a)  $\mathbf{R} = (16, 1)$  and (b)  $\mathbf{R} = (17, 1)$ . (c) The metallic carbon nanotube with  $\mathbf{R} = (16, 1)$  can roll up without the misfit of the Kekulé pattern, but (d) semi-conducting carbon nanotube with  $\mathbf{R} = (17, 1)$  induce the misfit.

the viewpoint of molecular chemistry, we can see this variety of hybridization as the following structural variety of molecules:  $sp$ ,  $sp^2$  and  $sp^3$  carbons form straight molecules as polyacetylene, planer molecules as benzene and stereoscopic molecules as methane, respectively. On the other hand, from the viewpoint of crystallography, the variety of hybridization appears as:  $sp^2$  and  $sp^3$  carbons form graphite and diamond. Therefore, carbon can take various structures because of these possibilities of hybridization of atomic orbitals. Since the other column IV elements like Si are cannot form  $sp$  or  $sp^2$  like hybridization, this structural variety of carbon is the significant difference between Carbon and other column IV elements such as Si, Ge.

In many years, it was considered that carbon-related materials consisting of  $sp^2$  carbon have only planer structures. However, soccer ball shape molecule  $C_{60}$ , discovered by H. Kroto and R. Smally in 1985 [13], showed that  $sp^2$  carbon can form closed cage structure. In 1990 Krätschmer and co-workers have developed a new method to synthesize  $C_{60}$  clusters in large quantities [14], this experimental success has initiated the research of fullerene molecules. Successively, rugby ball shape molecule  $C_{70}$  and other fullerene molecules of larger number of carbon atoms or fullerene molecules having metal elements in their cages have been discovered.

In  $sp^2$  carbon materials, each  $sp^2$  carbon atom has three  $\sigma$ -bonds which connect neighboring atoms, and has a single  $\pi$ -electron. The  $\pi$ -orbital is perpendicular to  $\sigma$ -orbitals. Since these  $\pi$ -electrons govern the electronic states near the Fermi level, the topology of the  $\pi$ -electron network significantly influence the electronic structures of  $sp^2$  carbon materials.

A simple and significant example, in which the network topology of  $sp^2$  carbons plays important roles, is carbon nanotube system. The carbon nanotubes were discovered by S. Iijima in 1991, and showed that  $sp^2$  carbon networks can be rolled up into cylindrical form with nanometer scale diameter and micrometer scale length [15]. The diameter and helicity of a nanotube are uniquely determined by the chiral vector  $\mathbf{R} = m\mathbf{a} + n\mathbf{b} = (m, n)$ , where  $n$  and  $m$  are integers. In the simple tight-binding approach, a carbon nanotube becomes metallic when  $m - n$  is divisible by three, otherwise semi-conducting [16–18]. This rule can be understood geometrically. This rule can be illustrated as follows: First we paint one of three sublattice sites in a graphite sheet as shown in Fig. 1.1 (a) and (b). The cylindrical fullerene tubule can be made by cutting out a strip whose width is specified by the vector  $\vec{R}$  and by rolling it into a cylinder where  $|\vec{R}|$  corresponds to the circumference. If we can roll it without misfit of the decoration (Fig.1.1(c)), the tubule becomes metallic, otherwise insulating (Fig.1.1(d)). Mathematically it is represented by  $\vec{R} = (m, n)$ , the tubule is metallic in the case that  $m - n$  is a multiple of 3, otherwise insulating. Hereafter we call the condition for the circumferential vector  $\vec{R}$  to give a metallic tubule as “the Kekulé rule”. Recent studies with scanning tunneling microscopy and spectroscopy have confirmed this interplay between the geometry of  $sp^2$  carbon and their electronic states [19, 20]. Thus the geometry of  $sp^2$  carbon networks is substantial in nanoscale carbon systems.

The role of a pentagonal ring in a single graphite sheet is displayed in Fig.1.2(a) where we see around an apical pentagonal ring a conical surface consisting of hexagons is formed. While if you put a heptagonal ring in a sheet as well, a saddle-shaped surface appears around it (Fig.1.2(b), which means a surface with negative curvature is introduced by a heptagon. A polygonal ring except a hexagon can be regarded as a defect on a graphitic sheet.

Introduction of negative curvature makes it possible to construct topologically more complicated structures than those of normal fullerenes which are topologically equivalent to a sphere. When we introduce twelve pairs

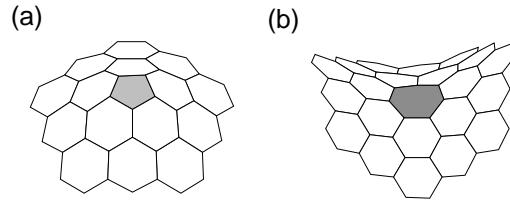


Figure 1.2: (a) A five-membered ring and (b) a seven-membered ring in a graphite sheet.

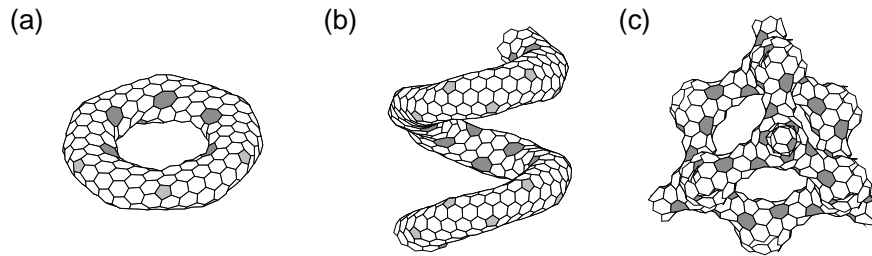


Figure 1.3: (a) Fullerene torus  $C_{504}$ , (b) Coiled tubule and (c) graphitic spongy.

of pentagonal and heptagonal rings, we can construct a fullerene torus as shown in Fig. 1.2 (a). If we joint the units of an unclosed torus one after another, we obtain a coiled fullerene tubule as shown Fig. 1.2 (b). The coiled fullerene tubule have been already synthesized and their electronic states are intensively examined now. Based on the theory of periodic minimal surfaces [21, 22], the existence of periodic graphite surfaces with negative curvature were suggested, including heptagonal or octagonal rings in three dimensional space, called “graphitic spongy” [23–27]. Based on the simple tight binding model, Fujita and co-workers have found that some of graphitic spongy systems have a flat band at the Fermi energy all over the Brillouin zone [27]. If we remind that a graphene sheet is a zero-gap semiconductor whose density of states is zero at the Fermi level, the appearance of the flat band is a surprising result.<sup>3</sup>

Thus, the existence of the polygonal defects in nano-size carbon systems drastically changes the  $\pi$  electronic states. However, we have to be aware of the existence of the other important element which drastically changes the  $\pi$  electronic states in nano-size systems. The element is the “graphite edge”. In next section, I briefly introduce the effect of graphite edge on  $\pi$  electronic states.

## 1.2 Nanosize Carbon Systems with Open Boundary

### 1.2.1 Edge states

There are two typical shapes of a graphite edge, called *armchair* and *zigzag*. These two edges have  $30^\circ$  degree difference in their cutting direction (see Fig1.4). Here I briefly introduce the fact that the existence of the edges drastically changes the  $\pi$  electronic structures. Especially, a zigzag edge provides the edge localized state, while an armchair does not show such localized states. We hereafter call this localized state “edge state”<sup>4</sup>. The existence of the edge states was pointed out analytically and numerically by Fujita, Wakabayashi, Nakada and Kusakabe. The results presented in this section are published in Ref [32].

A simple and useful model to study the edge and size effect is the graphene ribbon models as shown in Fig1.5. We define the width of graphene ribbons as  $N$ , by the number of the dimer lines for the armchair ribbon and by the number of the zigzag lines for the zigzag ribbon, respectively. It is assumed that all dangling bonds at the edge are terminated by hydrogen atoms, and thus give no contribution to the electronic states near the Fermi level. We employ a single-orbital tight binding model for the  $\pi$  electron network. This model has been successfully used for the calculation of electronic states of fullerene molecules, carbon nanotubes and

<sup>3</sup>The appearance of flat bands in the superlattice structures with hexagonal symmetry is discussed by Shima and Aoki, see reference [28].

<sup>4</sup>The edge localized states was pointed in the context of large size aromatic molecules which contain hundreds of carbon atoms, however the origin of the edge states and analytic representation was not clarified there [29–31].

other carbon-related materials [17, 33]. The Hamiltonian is written as,

$$H = \sum_{\langle i,j \rangle} t_{ij} c_i^\dagger c_j \quad (1.1)$$

where the operator  $c_i^\dagger$  creates an electron on the site  $i$ ,  $\langle i, j \rangle$  denotes the summation over the nearest neighbor sites. Transfer integrals are set at  $t$  between all the nearest neighbor sites for simplicity, because here we aim to reveal the intrinsic difference in the electronic states originating from the topological nature of each system.

Prior to the discussion of the  $\pi$ -electronic states of graphene ribbon systems, we shall briefly review the  $\pi$ -band structure of a graphene sheet [9, 33–37]. The band structure of graphene ribbons can be predicted from that of the graphene sheet, which is a zero-gap semiconductor. In Fig.1.6(a) and (b), it is shown unit cells and Brillouin zones of two dimensional graphite. The vectors,  $\mathbf{a}$  and  $\mathbf{b}$ , are usually taken as unit vectors in Fig.1.6(a). In the  $x - y$  coordinates shown in the Fig.1.6(a), real space unit vectors  $\mathbf{a}$  and  $\mathbf{b}$  are expressed as

$$\mathbf{a} = \left( -\frac{3a}{2}, \frac{\sqrt{3}a}{2} \right) \quad \mathbf{b} = \left( \frac{3a}{2}, \frac{\sqrt{3}a}{2} \right), \quad (1.2)$$

where  $a=1.42\text{\AA}$  is the lattice constant of the graphene sheet. The corresponding unit vectors  $\mathbf{a}^*$  and  $\mathbf{b}^*$  of the reciprocal lattice are given by

$$\mathbf{a}^* = \left( -\frac{2\pi}{3a}, \frac{2\pi}{\sqrt{3}a} \right) \quad \mathbf{b}^* = \left( \frac{2\pi}{3a}, \frac{2\pi}{\sqrt{3}a} \right). \quad (1.3)$$

Then the 1st BZ has a hexagonal shape as shown in the Fig1.6, where the corner of this hexagonal 1st BZ is called  $\mathbf{K}$  (or  $\mathbf{K}'$ ) point. We call the two inequivalent sites in a unit cell A and B site, and define the electron creation operator at A-site [B-site] of a unit cell called  $\alpha$  as  $c_\alpha^\dagger(\text{A})[c_\alpha^\dagger(\text{B})]$ . By the Fourier transformation defined as

$$c_{\mathbf{k}}^\dagger(i) = \frac{1}{\sqrt{N}} \sum_{\alpha} c_\alpha^\dagger(i) e^{i\mathbf{k}\mathbf{r}_\alpha} \quad (i = \text{A}, \text{B}), \quad (1.4)$$

the tight binding Hamiltonian of the 2D graphite in the  $\mathbf{k}$ -space is written as

$$H = \sum_{\mathbf{k}} \epsilon_{\mathbf{k}} c_{\mathbf{k}}^\dagger(\text{B}) c_{\mathbf{k}}(\text{A}) + \text{h.c.}, \quad (1.5)$$

where

$$\epsilon_{\mathbf{k}} = -t \left[ e^{ik_x a} + e^{-i\left(\frac{k_x a}{2} + \frac{k_y \sqrt{3}a}{2}\right)} + e^{-i\left(\frac{k_x a}{2} - \frac{k_y \sqrt{3}a}{2}\right)} \right] \quad (1.6)$$

and the summation of  $\mathbf{k}$  is taken over the 1st BZ. The above equation can be diagonalized as

$$H = \sum_{\mathbf{k}\sigma} (\epsilon_{\mathbf{k}}^- \alpha_{\mathbf{k}\sigma}^\dagger \alpha_{\mathbf{k}\sigma} + \epsilon_{\mathbf{k}}^+ \beta_{\mathbf{k}\sigma}^\dagger \beta_{\mathbf{k}\sigma}), \quad (1.7)$$

where  $\epsilon_{\mathbf{k}}^\pm$  is written as

$$\epsilon_{\mathbf{k}}^\pm = \pm t \sqrt{3 + 2 \cos\left(\frac{3k_x a}{2} + \frac{\sqrt{3}k_y a}{2}\right) + 2 \cos\left(\frac{3k_x a}{2} - \frac{\sqrt{3}k_y a}{2}\right) + 2 \cos(\sqrt{3}k_y a)}, \quad (1.8)$$

and this  $\epsilon_{\mathbf{k}}^\pm$  gives the energy dispersion relation of 2D graphite. Here  $\alpha_{\mathbf{k}}^\dagger$  [ $\beta_{\mathbf{k}}^\dagger$ ] is an electron creation operator on  $\epsilon_{\mathbf{k}}^-$  [ $\epsilon_{\mathbf{k}}^+$ ]-band. Since one carbon site has one  $\pi$ -electron on average, only  $\epsilon_{\mathbf{k}}^-$ -band is completely occupied. Hereafter, we call  $\epsilon_{\mathbf{k}}^-$  [ $\epsilon_{\mathbf{k}}^+$ ] valence [conduction] band.

In Fig.1.6 (c) and (d), the energy dispersion of  $\pi$ -bands in the 1st BZ and the density of states are depicted, respectively. Let us explain some features of energy-band near three high symmetry points,  $\Gamma$ ,  $M$ , and  $K$  in 1st BZ. Near the  $\Gamma$  point, that is, the bottom of the valence band or the top of the conduction band, the energy dispersion has the quadratic form of  $k_x$  and  $k_y$  like free electron energy band in a simple metal. Near the  $M$  points at the middle of a side of the hexagonal BZ, the saddle point of energy dispersion appears where the

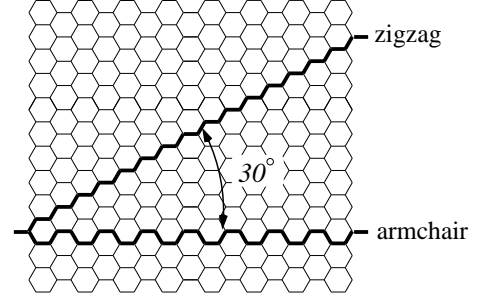


Figure 1.4: The typical graphite edge, *armchair* and *zigzag*.

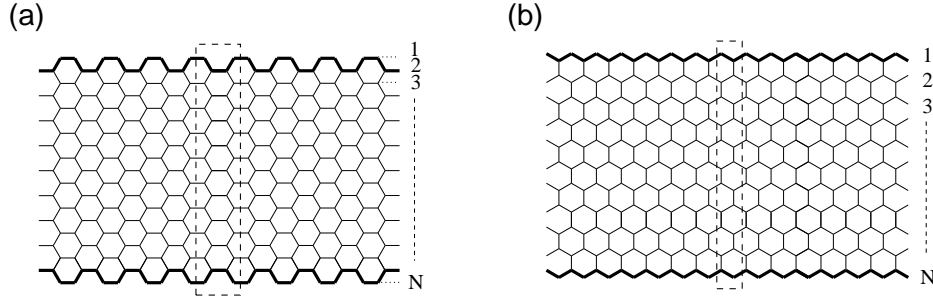


Figure 1.5: The structure of graphene ribbon with (a) armchair edges (b) zigzag edges. The rectangle with the dashed line is the unit cell.

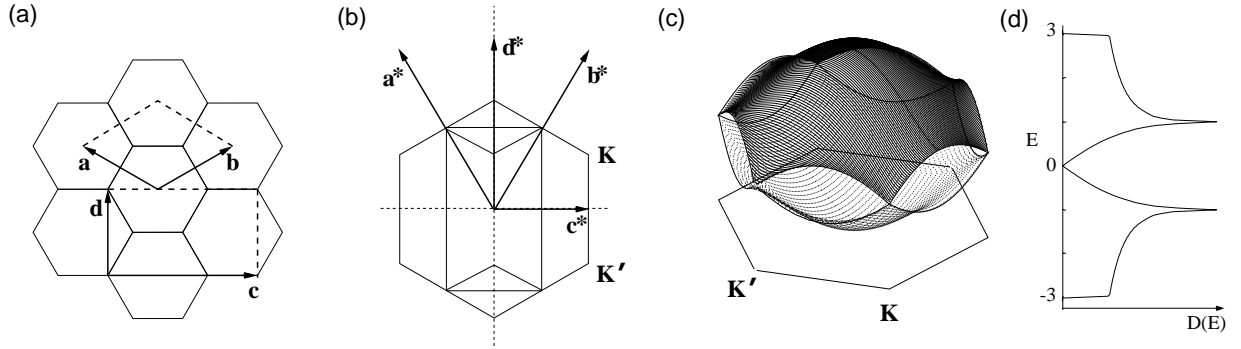


Figure 1.6: The unit cells (a) in real space and (b) reciprocal space of graphene sheet. The vectors  $\mathbf{c}$  and  $\mathbf{c}^*$  ( $\mathbf{d}$  and  $\mathbf{d}^*$ ) relate to armchair (zigzag) ribbons in (a) and (b). (c) The  $\pi$  band structure and (d) the density of states of graphene sheet. The valence and conduction bands make contact at the degeneracy point K and K'.

effective masses along  $k_x$  and  $k_y$  axes have a different sign and the density of states diverges logarithmically. The absolute value of  $\epsilon(k)$  is  $t$  at M point. Near K point of the corner of hexagonal 1st BZ, the energy dispersion is linear in the magnitude of wave vector,

$$\epsilon(k) = \frac{3}{2}ta|\mathbf{k}|, \quad (1.9)$$

where the density of states linearly depends on the energy. The Fermi energy is located at the K points and there is no energy gap at these points, since  $\epsilon(k)$  vanishes at this point by the hexagonal symmetry. Thus, the graphene sheet is a zero-gap semi-conductor on this 2D model.

Next we shall consider the  $\pi$  electronic structures of graphene ribbon models. We take a rectangular unit cell, by folding the the BZ into a rectangle, which is half as large as the hexagonal BZ shown in Fig.1.6 (b). The unit vector  $\mathbf{c}$  ( $\mathbf{d}$ ) denotes the translational axis of an armchair (zigzag) ribbon, and the shorter (longer) side of the rectangular BZ is the one-dimensional BZ of armchair (zigzag) ribbons. The global band structure of graphene ribbons having armchair (zigzag) edges is then predicted by projecting that of 2D graphite onto the corresponding axis  $\mathbf{c}^*$  ( $\mathbf{d}^*$ ) using the zone-folding technique. The linear dispersion relations stemming from the original K point are expected to appear around  $k = 0$  ( $k = 2\pi/3$ ) for armchair (zigzag) ribbons.

The calculated band structures of armchair ribbons are shown in Figs.1.7 (a)-(c), for three different ribbon widths, together with the density of states. The wave number  $k$  is normalized by the primitive translation vector of each graphene ribbon, and the energy  $E$  is scaled by the transfer integral  $t$ . The top of the valence band and the bottom of the conduction band are located at  $k = 0$ , as expected. It should be noted that the ribbon width critically controls whether the system is metallic or semiconducting. As shown in Fig.1.7 (b), the system is metallic when  $N = 3M - 1$ , where M is an integer. This periodicity can be analytically understood by regarding the system at  $k = 0$  as a ladder network, described in the later chapter. For the semiconducting ribbons, the direct gap decreases with increasing ribbon width and tends to zero in the limit of very large  $N$ . In Fig.1.7 (d), we show the calculated band structure of an armchair ribbon ( $N = 30$ ) together with the band structure of 2D graphite projected onto an armchair axis[Fig.1.7 (e)]. It is seen that the projected band structure of 2D graphite is almost reproduced by that of a wide armchair ribbon.

For zigzag ribbons, however, a remarkable new feature arises in the band structure, as shown in Figs.1.8 (a)-(c). We see that the highest valence band and lowest conduction band are always degenerate at  $k = \pi$ ,

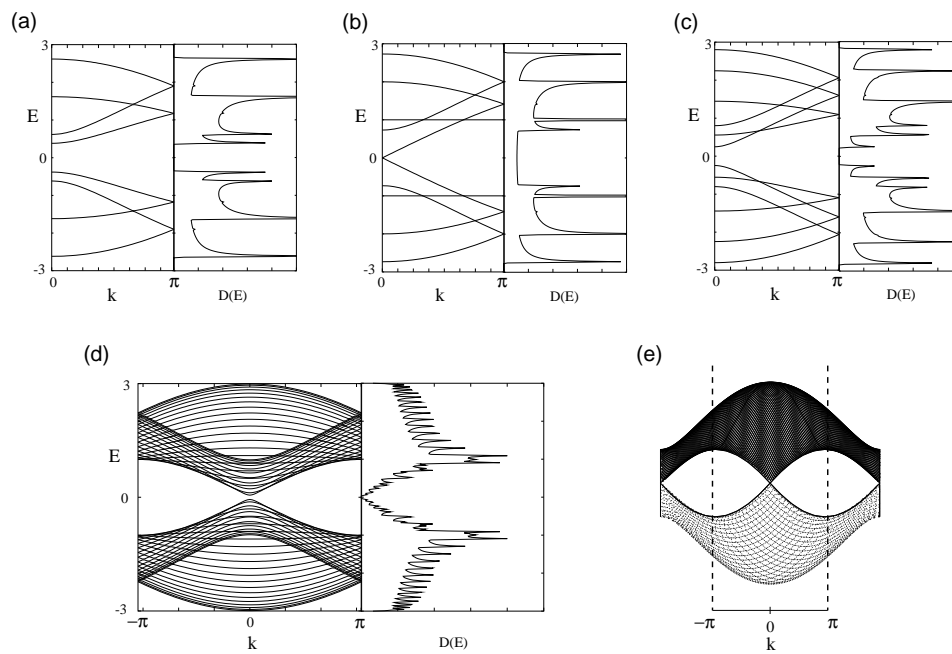


Figure 1.7: Energy band structure  $E(k)$  and density of states  $D(E)$  of armchair ribbons of various widths [(a)  $N=4$ , (b) 5 and (c) 6 ], (d) calculated band structure of an armchair ribbon of  $N = 30$  and (e) expected band structure for

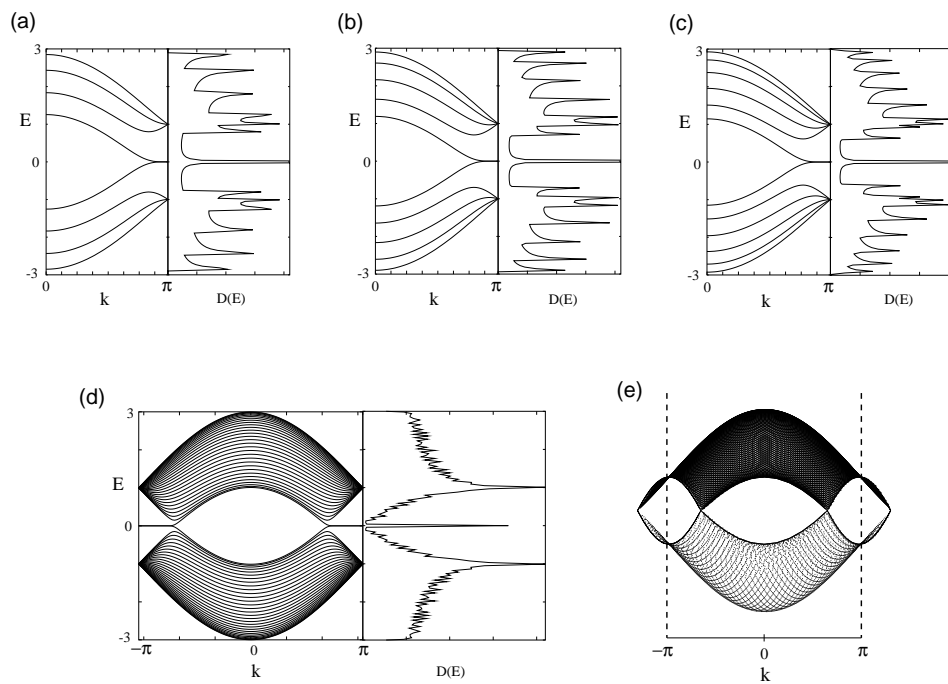


Figure 1.8: Energy band structure  $E(k)$  and density of states  $D(E)$  of zigzag ribbons of various widths [(a)  $N=4$ , (b) 5 and (c) 6 ], (d) calculated band structure of a zigzag ribbon of  $N = 30$  and (e) expected band structure for

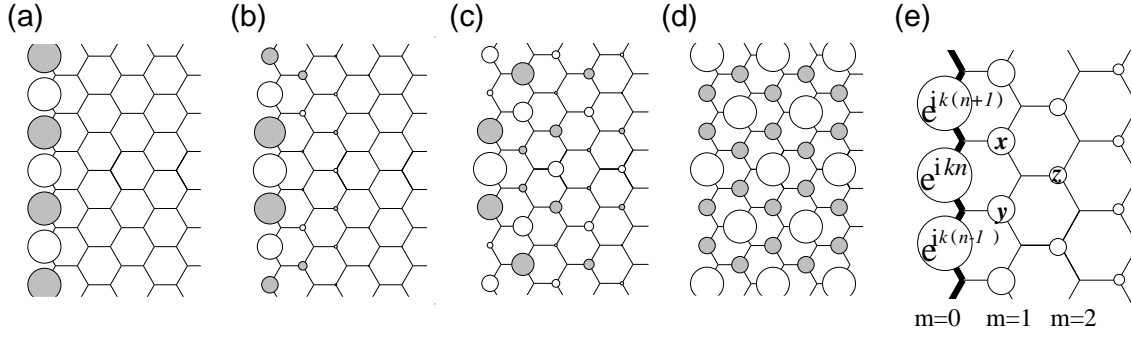


Figure 1.9: Schematic figures of the real part of analytic solutions for the Edge State in a semi-infinite graphite, when (a)  $k = \pi$ , (b)  $8\pi/9$ , (c)  $7\pi/9$  and (d)  $2\pi/3$ . (e) An analytic form of the edge state for a semi-infinite graphene sheet with a zigzag edge, which is emphasized by bold lines. Each carbon site is specified by a location index  $n$  on the zigzag chain and by a chain order index  $m$  from the edge. The magnitude of the charge density at each site, such as  $x$ ,  $y$  and  $z$ , is obtained analytically (see text). The radius of each circle is proportional to the charge density on each site, and the drawing is made for  $k = 7\pi/9$ .

though the degeneracy is expected to appear at  $k = 2\pi/3$  on the basis of the projected band structure of 2D graphite. We find that the degeneracy of the center bands at  $k = \pi$  does not originate from the intrinsic band structure of 2D graphite, and the corresponding wave functions are completely localized on the edge sites. These two special center bands get flatter with increasing ribbon width. We show the band structure for the zigzag ribbon ( $N = 30$ ) together with the projected band structure of 2D graphite in Figs.1.8 (d) and (e). A pair of almost flat bands appears within the region of  $2\pi/3 \leq k \leq \pi$  where the bands sit in the vicinity of the Fermi level. No such flat band is expected for the projected band structure of 2D graphite. As seen in Fig. 1.8(d) the second lowest conduction band shows a dip near  $k = 2\pi/3$ , where the highest valence band below the center bands shows a rise, approaching closer to each other as  $N$  increases, thereby the electronic state around the original K point in 2D graphite.

The electronic state in the almost flat bands of the zigzag ribbons is found to be characterized as the localized state near the zigzag edge by examining the charge density distribution [26, 38]. Here we show that the puzzle for the emergence of the edge state can be solved by considering a semi-infinite graphene sheet with a zigzag edge. The analytic form of the wave function is depicted in Fig.1.9. Previous to show the analytic form, we depict the real part of the wave function in the flat band states for some wave numbers in Fig.1.9, where the amplitude is proportional to the radius, and the shading denotes the sign. The wave function has values on one of the sublattices which includes the edge sites. It is completely localized at the edge site when  $k = \pi$ , and starts to gradually penetrate into the inner sites as  $k$  deviates from  $\pi$  reaching the extended state at  $k = 2\pi/3$ .

Considering the translational symmetry, we can start constructing the analytic solution for the edge state by letting the Bloch components of the linear combination of atomic orbitals (LCAO) wavefunction be  $\dots, e^{ik(n-1)}, e^{ikn}, e^{ik(n+1)}, \dots$  on successive edge sites, where  $n$  denotes a site location on the edge. Then the mathematical condition necessary for the wave function to be exact for  $E = 0$  is that the total sum of the components of the complex wave function over the nearest-neighbor sites should vanish. In Fig.1.9, the above condition is  $e^{ik(n+1)} + e^{ikn} + x = 0$ ,  $e^{ikn} + e^{ik(n-1)} + y = 0$  and  $x + y + z = 0$ . Therefore, the wave function components  $x$ ,  $y$  and  $z$  are found to be  $[-2 \cos(k/2)]e^{ik(n+1/2)}$ ,  $[-2 \cos(k/2)]e^{ik(n-1/2)}$ ,  $[-2 \cos(k/2)]^2 e^{ikn}$ , respectively. We can thus see that the charge density is proportional to  $[2 \cos(k/2)]^{2(m-1)}$  at each non-nodal site of the  $m$ -th zigzag chain from the edge. Then the convergence condition of  $|-2 \cos(k/2)| \leq 1$  is required, for otherwise the wave function would diverge in a semi-infinite graphene sheet. This convergence condition defines the region  $2\pi/3 \leq |k| \leq \pi$  where the flat band appears.

Thus the appearance of the partly flat bands is due to the edge localized states. The edge states survive for the more generic edges which are the mixture of armchair and zigzag [39]. The reason why the edge states strongly tend to survive is discussed in the chapter 2 with the continuum approach.

### 1.2.2 Nanographites

The appearance of the edge states makes a sharp peak around  $E = 0$  of the density of states, while the graphene sheet and aromatic molecules do not show such a peak in their density of states. This fact implies that the nanosize carbon systems with open boundaries might have quite different electronic states from the aromatic molecules and bulk graphites. Consequently, we expect that magnetic and transport properties also are quite

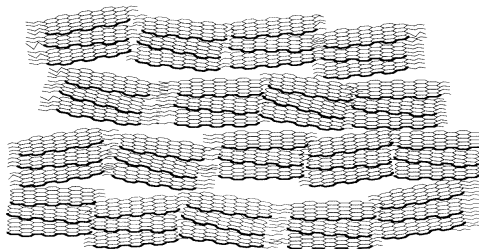


Figure 1.10: A proposed structure model of activated carbon fibers (Ref. [42]).

different from the aromatic molecules and bulk graphites. From now on, we call the group of the nanosize carbon systems with open boundaries “nanographite”, as a new class of carbon systems<sup>5</sup>.

## 1.3 Nanographite Systems

In this section, I briefly review recent advances of nanosize carbon-related materials. I especially focus on activated carbon fiber and graphitized nano-diamonds, which are considered as a assembly of nano-graphites. Activated carbons and carbon fibers are industrially important and scientifically interesting materials. These materials are used in many daily industrial products, for instance, a water-purifying device for home use and deodorants used in refrigerators. There are many kinds of carbons which are classified by the production processes, i.e. Carbon blacks, evaporated carbon films, anthracite carbon powders, glassy carbons, activated carbons, carbon fibers and activated carbon fibers. In general, it is considered that these materials consist of an assembly of many micro- and nano-graphite fragments which are composed of disordered stacks of three or four graphene sheets with a size ranging from  $nm$  up to  $\mu m$  order.

### 1.3.1 Activated Carbon Fibers

Activated carbon fibers (ACF) developed by Osaka Gas Chemical Co., Ltd. are microporous carbon systems which have enormous specific surface areas (SSA) ranging from 700 to 3000  $m^2/g$ . The manufacturing process called “activation” gives the porous structure to the fibers, resulting in making SSA larger than other porous materials. Studies with X-ray diffraction, Raman spectra, transmission electron microscope observations and gas adsorption clarified the porous ACF structure. A total structural model proposed by Kaneko and co-workers is shown in Fig.1.10. ACFs consist of an assembly of many nanometer-sized graphites which form disordered stacks of three to four graphene sheets with a dimension of ca.  $20 \times 20 \text{Å}^2$  [42–44]. An assembly of many nano-graphites form a network structure, resulting in the presence of micropores with the dimension of 10 to 20Å. The average micropore size estimated by the nitrogen adsorption is 0.4, 1.0 and 0.8 nm for ACF1000, ACF2000 and ACF3000 having the SSA of 1000, 2000 and 3000  $m^2/g$ , respectively. There are dangling bonds and functional groups at the peripheries of nano-pores, which give localized spins. The pore structure is the origin of the enormous specific surface areas, which provides huge amount of gaseous materials [45]. Interestingly, the magnitude of SSA of 3000  $m^2/g$  exceeds the theoretical upper limit of SSA, which is 2630  $m^2/g$  interpreted for a single layer of adsorbed molecules covering both surface of a single layer [42].

The electrical conductivities of ACFs show semi-conducting behavior, while bulk graphites show semi-metallic conducting behavior [46–48]. This feature is modified by heat-treatment, particularly, in the temperature range above 800°C; that is, the heat treatment around 800°C starts stripping functional groups off from the marginal regions of nano-graphites, making contact more enhanced between nano-graphite domains without an increase in the mean in-plane size. Further heat-treatment at higher temperatures increases the in-plane size and it regularizes the structure of the nano-graphite network. This brings about the development of percolation paths for electron transport between domains, resulting in the occurrence of an insulator-to-metal transition around the heat treatment temperature of 1200-1300°C.

The heat-treatment also changes the magnetic properties. ACFs show qualitatively different magnetic properties from bulk graphites which show large diamagnetic susceptibility [49–53]. In Fig.1.11, the temperature dependence of the magnetic susceptibility  $\chi$  for HTT800-1500 is shown. It is considered that the contamination by magnetic impurities can be excluded in the ACF samples. For the  $\text{HTT} \leq 1100^\circ\text{C}$  samples (L-HTT ACFs),  $\chi$

<sup>5</sup>Recently, it is also discussed the extension of the edge states to the 3-dimensional networks, called “hypergraphite”, where the peculiar electronic properties are expected [40, 41]. The names “nanographite” and “hypergraphite” were proposed by late Mitsutaka Fujita.

obeys the Curie-Weiss law with negative Weiss temperatures  $\sim 2-3\text{K}$  in the whole temperature range, revealing the presence of weakly antiferromagnetic interactions. The antiferromagnetic interactions are also confirmed by the non-linear field dependence of the magnetization curves. The localized spin concentration is estimated at about 1 spin per graphene fraction for as-prepared ACF. Heat-treatment reduces the spin concentration monotonically, approaching 0.5 spin per concentration in the heat-treatment process below  $1600^\circ\text{C}$ , which suggests the absence of a serious change in the spin concentration in the heat-treatment process below  $1600^\circ\text{C}$ . In any case, the experimental finding proves that each graphene fraction has about 1 spin irrespective of the heat-treatment temperature. The fact that each graphene fraction has about 1 spin, therefore, reveals that the observed antiferromagnetic interaction is characterized as inter-nano-graphite-domain interaction having a long range feature. Further, an interesting point is observed around the threshold of the percolation-type metal-insulator transition. The magnetic susceptibility indicates an anomalous behaviors at low temperatures as shown in the inset of Fig.1.11. Namely, it takes a cusp around 4-7K, which has a large field cooling effect in the vicinity of the cusp. The magnetization curves at low temperatures is subjected to a random distribution in the strength of antiferromagnetic interactions. Accordingly, the characteristic features of the cusp-like susceptibility demonstrates the occurrence of a spin glass state in the randomly networked nano-graphite spin systems [51, 52].

### 1.3.2 Graphitized Nano-diamonds

In connection with carbon-based nanoparticles, it is well-known that nanosized-diamond particles, prepared by explosion-induced high-pressure techniques, have a regular atomic arrangement of a diamond structure with sized of  $\sim 5\text{ nm}$ . According to X-ray diffractions, transmission electron microscope observation and Raman spectra, heat-treatment at  $900^\circ\text{C}$  converts only the surfaces of the particles into graphite. The higher heat-treatment temperature increases the fraction of graphite, and eventually, the particles are completely converted to graphite over  $\text{HTT } 1600^\circ\text{C}$ , where they form polyhedra with hollows in their inside, whose facets consist of 3-6 planar graphene sheets with an in-plane size of 7-8 nm and an intersheet distance of 0.353 nm. This intersheet distance is larger than that of bulk graphite ( 0.3354 nm ), resulting in a large reduction in the strength of interlayer interaction, thereby, the nano-graphite are considered to be an assembly of non-interacting nano-graphene sheets.

Figure 1.12 shows the temperature dependence of the magnetic susceptibility for the nano-graphite sample prepared by the heat-treatment at  $1600^\circ\text{C}$ , where the observed susceptibility is analyzed in terms of the contributions of the Curie paramagnetism, Pauli paramagnetism, orbital diamagnetism and core diamagnetism [55]. The orbital diamagnetic susceptibility of  $\pi$  electrons  $\chi_{orb}$ , which has a weak temperature dependence, was analyzed in terms of the Kotosonov equation. The observed values give an estimate of the Fermi energy of  $E_F \sim 0.10\text{eV}$  in addition to the presence of disorder-induced energy level broadening. The Curie paramagnetism is explained with presence of defects. Interestingly, the Pauli paramagnetic susceptibility is one to two orders of magnitudes larger than that for bulk graphite. This proves the presence of an additional contribution to the density of states around the Fermi energy superimposed with the conduction  $\pi$ -band. This observed enhancement of the density of states at the Fermi level can be explained by the contribution of the edge states. The connection between this magnetic behavior and the edge states will be discussed in Chapter 3.

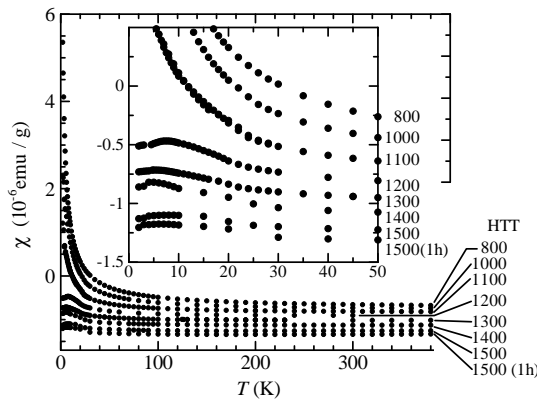


Figure 1.11: Temperature dependence of the magnetic susceptibility  $\chi$  for the ACFs heat-treated up to  $1500^\circ\text{C}$ . The inset is the detailed behavior at low temperature (Ref. [52]).

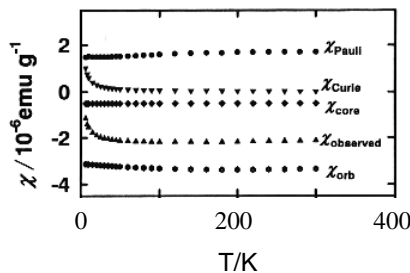


Figure 1.12: Temperature dependence of the magnetic susceptibility  $\chi$  for the ACFs heat-treated up to 1500°C. The inset is the detailed behavior at low temperature (Ref. [55]).

### 1.3.3 Technological application of nano-graphites

Recent incredible down-sizing of mobile electronic equipments such as handy-phone, video-camera and laptop-computer increases the demand for smaller, lighter and long-lasting re-chargeable secondary batteries. Nowadays, primary cells with Lithium metal anodes have attracted much industrial and technological attention as a high-energy density, high-voltage and low-self-discharge rate secondary battery. Li ions electrochemically can be stored into the interlayers of graphites, resulting in forming a stage compounds called graphite intercalation compound (GIC). Since this storage process is reversible, graphite can be used instead of metallic Li as the negative electrode in Li secondary batteries [56–59].  $\text{LiC}_6$  is a first stage GIC and the compound with greatest concentration of intercalated-atoms, where Li ions form a  $\sqrt{3} \times \sqrt{3}$  structure on a honeycomb lattice. However, in the small graphite clusters that are pyrolytically synthesized from hydrocarbons, such as poly-paraphenylene (PPP) and phenol-formaldehyde (polyacene semiconductors, PAS), the graphite cluster can accept three times as many Li ions ( $\text{LiC}_2$ ) [60]. This fact offers promise for enhanced battery performance relative to the graphite host material.

Recently Saito and co-workers have pointed out that the mechanism of the excess acceptance of Li ions can be connected to the existence unoccupied non-bonding edge state near the Fermi levels [61,62]. When Li ions are near the zigzag edges, the charge transfer will occur from Li ions to the edge states, because the unoccupied non-bonding edge states of the zigzag edges are near the Fermi energy, which have a lower energy than the 2s states of a Li atom. Significant insight into the Li-C binding mechanism has been obtained by looking for the most active sites for lithium binding on to a graphene cluster, calculating the amount of charge transfer between the carbon cluster and the lithium ions and determining the stability of various edge sites in comparison to the bulk sites. Since the disordered carbons are normally prepared from organic hydrogen-containing precursors (such as polyparaphenylene), the stability of Li binding sites in the absence and presence of hydrogen has been considered. Figure 1.13 (a) shows a  $\text{C}_{96}$  graphene cluster to which a single Li (shaded) is attached. This figure shows the optimal distances for the lithium atom from the surrounding carbon atoms at the edges for this particular binding site in the figure. Also given in the figure are the magnitudes and signs of the charge on the various neighboring sites. The charge transfer from the Li ion to the graphene cluster is located at the edge region. However, the ionicities of the two nearest-neighbor carbon atoms are almost zero. When the dangling bonds on the cluster are terminated by hydrogen atoms, different sites are favored for Li as shown in 1.13(b). For example, weak bonding to an out-of-plane site for Li attachment is found in this case, as shown in Fig. 1.13(b). Similar high-reactivity of graphite edges are also pointed out in the fluorinated-ACFs [63,64].

## 1.4 Synthesis of Nanographite Ribbons

In the previous section, we have seen that nanographites have quite different  $\pi$  electronic states from those of both aromatic molecules and a graphite sheet, and their edge shapes also crucially affect their electronic states and chemical reactivity. We have already pointed out some example systems consisting of nanographites, i.e. activated carbon fibers, nanographites derived from nanodiamonds and defective carbon nanotubes. However, the size and shapes of these systems are rather difficult to control experimentally. Here we introduce two recent experimental efforts in this direction. One is the direct manipulation and fabrication of graphites by using scanning tunneling microscopes ( STM ), the other is the manufacturing of nano sized ribbon shaped graphites on a metal substrate by using a growth techniques of mono-layered graphite.

Hiura and co-workers proposed the idea of graphene fabrication, *graphite origami*, with an atomic force microscope (AFM) or a STM [65,66]. On the way to study the fabrication techniques, they found a folded graphene ribbons which spontaneously formed on highly oriented pyrolytic graphite (HOPG), as shown in Fig.

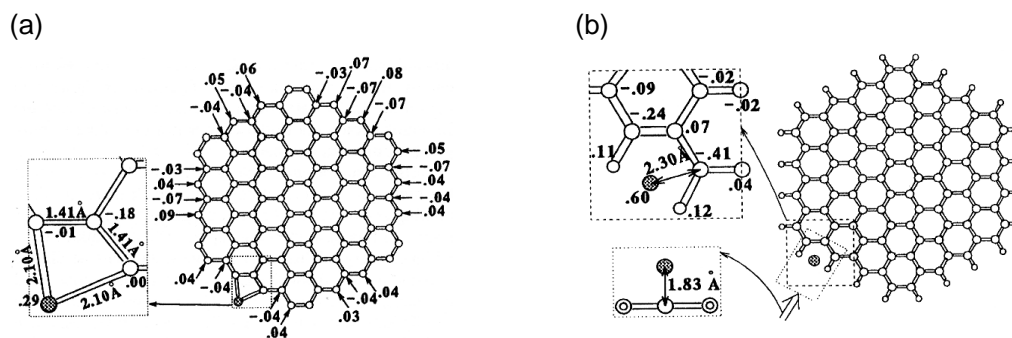


Figure 1.13: (a) An optimized Li geometry in the C<sub>96</sub> cluster. A Li ion is covalently bonded with the two nearest-neighbor carbon atoms. The charge transfer from the Li ion to the graphite cluster is located at the edge region. (b) An optimized Li geometry in the hydrogen-terminated C<sub>96</sub>H<sub>24</sub> cluster. Lithium binding can occur even when the edges are terminated by hydrogen atoms(Ref. [61]).

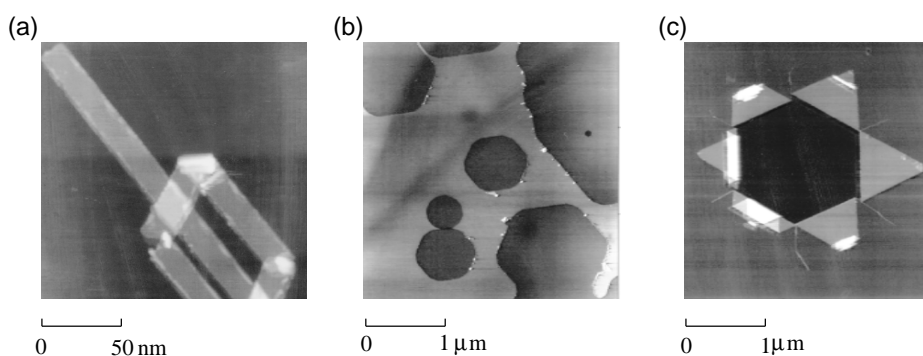


Figure 1.14: (a) AFM picture of a graphite ribbon folded 4 times on the surface of HOPG (Ref. [65]). (b) STM image of the surface of HOPG around the region where the electron beams are directly irradiated (Ref. [67]). (c) STM image of the surface of HOPG apart from directly irradiated region (Ref. [67]).

1.14(a). Interestingly, the graphite ribbon have dozens of *nm* width, and this means that ribbon shaped nanographite ribbons is stable in nature. Figure 1.14(b) and (c) show STM images of graphite surfaces after the irradiation of electron beams [67]. The Fig. 1.14(b) is the image around the region where the electron beams directly irradiated. The size of holes gets larger, the hexagonal symmetry of the holes becomes more clear. This fact indicates that if we cut graphite the zigzag or armchair edges are favored as the graphites rather than the mixture type edges of zigzag and armchair edges. In Fig. 1.14(c), the image in the region apart from directly irradiated region, we can find some hexagonal holes like a flower. Near the edges of these holes, it is expected the peculiar electronic states originated from the edge states.

Another formation of nanographites is by means of epitaxial growth on substrates having step edges [69] as shown in Fig. 1.15(a). Depending on the morphology of step edges, *e.g.*, terrace structure of a vicinal surface, ribbons with well-defined edge properties may be grown. In terms of these experimental trials, production control of nanographites are still difficult, and production of nanographite ribbons is rather accidental. However, it is important to notice that there is a difference in the growth properties of zigzag and armchair edges. From the studies on giant aromatic molecules, it is clear that armchair edges are thermodynamically more stable than zigzag edges, because the armchair edges do not have extra localized states near the Fermi level. On the other hand, because the localized states make zigzag edges chemically more reactive than armchair edges, zigzag edges will be favored rather than armchair edges in growth mechanism. In Fig. 1.15(b), a STM image of grown graphite on a metal substrate is shown. The large pattern in the image is due to the strong interaction between the metal substrate and first layer graphene sheet. It is clearly found that a small island of the second layer graphene is grown. In STM images, the atomic arrangements are not visible, but the periodicity of the atomic arrangements, so that when we observe graphite network by STM, we will find dual lattice of the graphite network, trigonal lattice. As shown in Fig. 1.15(b), for armchair (zigzag) edges, zigzag (straight) shape are observed in STM images. Actually, we can find that, since the second layer has straight, the zigzag edges are favored in growth experiments. Another group's experiment also confirmed this fact. Thus, it is considered

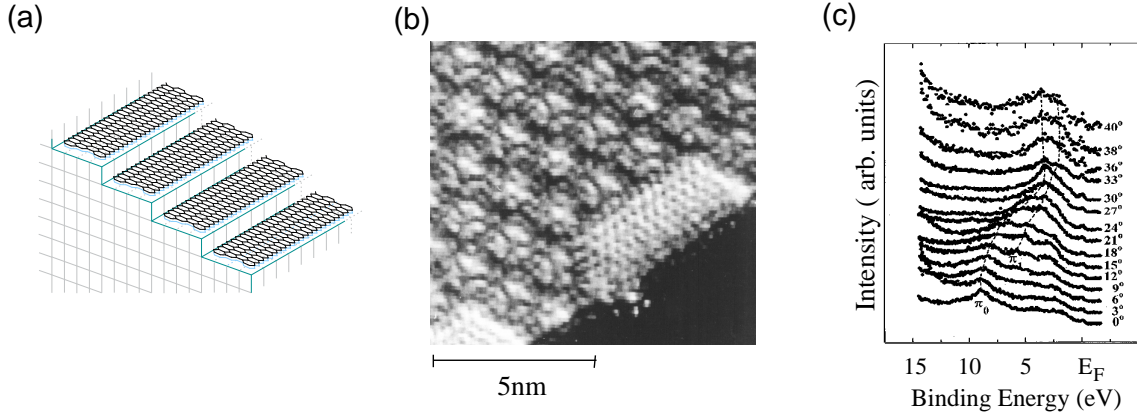


Figure 1.15: (a) The schematic figure of the epitaxial growth of graphene ribbon on metal substrate with terrace structures. (b) The STM image of the graphite-covered TaC(111) surface. The dark area in the lower right represents the lower terrace(Ref. [68]). (c) ARUPS spectra of the nanographene ribbons on the TiC(410) surface(Ref. [69]).

that the zigzag edges which is rather active than armchair edges are favored in growth mechanism. These facts also are intriguing for the studies on nanosize carbon systems. In Fig.1.15(c), it is shown the ARUPS spectra of the monolayer nanographite ribbon on the TiC(410) surface. The emission angle referred to the surface normal is denoted for each spectrum, and changes along the longer terrace direction. There are a few series of peaks due to graphite overlayer which are indicated by dashed lines. These peaks shift upwards as emission angle increases. It is considered that the line of peaks,  $\pi_0$ , corresponds to the  $\pi$  band bottom of the graphite, however, the other,  $\pi_1$ , and any other peaks are characteristic of the nanographite ribbon. The important point is that, in the spectra for the emission angle from  $30^\circ$  to  $38^\circ$ , the intensity of the peaks located just below  $E_F$  is much stronger than those for the other emission angles. Since such peaks are not seen in the monolayer graphite on flat substrate, these peaks can be interpreted as edge states [69, 70].

## 1.5 The Organization of this Thesis

The purpose of this thesis is to clarify the electronic, magnetic and transport properties in nano-size carbon systems. In this thesis, we point out that edge states, strongly localized states near zigzag edges, play important roles in the physical properties of nanosize graphite systems.

In chapter 2, we analyze the  $\pi$  electronic states of nanographites based on the graphene ribbon models in the absence and presence of magnetic field, where it is clarified that the existence of edges and their shapes crucially affect the  $\pi$  electronic states. The zigzag, bearded and cove edges show the non-bonding edge localized states (edge states), while the armchair edge does not show the edge states. The reason is given by the analogy with the mechanism of the Andreev bound states in anisotropic superconductor.

In chapter 3, we discuss the magnetic properties of nanographites. Since the edge states give the sharp peak in the density of states at the Fermi level, the strong paramagnetic response appears at low-temperature. Because this paramagnetic response is sensitive to the temperature, and shows Curie-like behaviors, the crossover from the high temperature diamagnetic response to low temperature paramagnetic response occurs in nanographite systems. The magnetic instability due to electron-electron interactions is also discussed in the chapter 3, where the peculiar magnetic states are found.

In chapter 4, we study the transport properties in nanographite systems, where we find the new quantum state called ‘‘Flux State’’, which is visible as a Kekulé-like current vortex patterns. The junctions or non-magnetic impurities causes zero-conductance, which can be understood by the interference of two flux states.

In chapter 5, the conclusion and outlooks are presented.

---

# Chapter 2

## Electronic States

---

In this chapter, we analyze the electronic states of graphene ribbons near the Fermi energy in the absence and presence of magnetic fields based on the tight binding model and the  $\mathbf{k} \cdot \mathbf{p}$  theory. The edge shapes crucially affect the  $\pi$  electronic states of nanographites.

### 2.1 Tight Binding Model in a Magnetic Field

In this section, we consider the single-orbital tight binding model including a magnetic field. This model was successfully used in fullerene, carbon nanotube carbon-related systems. The Hamiltonian is written as,

$$H = \sum_{\langle i,j \rangle} t_{ij} c_i^\dagger c_j \quad (2.1)$$

where the operator  $c_i^\dagger$  creates an electron on the site  $i$ ,  $\langle i, j \rangle$  denotes the summation over the nearest neighbor sites, and  $t_{ij}$  is a transfer (or hopping) integral between the site  $i$  and the site  $j$ . Throughout this chapter, the transfer integrals are set to  $t$  between all the nearest neighbor sites and otherwise to 0 for a simplicity, because here we aim at the intrinsic difference in the electronic states originating from the topological nature of each system. The transfer integral  $t$  is used as the unit of the energy, and estimated about 3.03 eV from experiments. We neglect spin indices for the moment. The magnetic field  $\mathbf{B}$  perpendicular to the graphite plane is incorporated in the transfer integral  $t_{ij}$  by means of the Peierls phase [71, 72] defined as

$$t_{ij} \longrightarrow t_{ij} e^{i2\pi\phi_{i,j}}, \quad (2.2)$$

where  $\phi_{i,j}$  is given by the line integral of the vector potential from site  $i$  to site  $j$ ,

$$\phi_{i,j} = \frac{e}{ch} \int_i^j d\mathbf{l} \cdot \mathbf{A}. \quad (2.3)$$

The magnetic flux through the area  $S$  in units of the flux quantum  $\phi_0 = \frac{ch}{e}$  is

$$\frac{1}{\phi_0} \int d\mathbf{S} \cdot \mathbf{B} = \frac{e}{ch} \oint d\mathbf{l} \cdot \mathbf{A} = \sum_{\text{area } \mathbf{S}} \phi_{i,j}. \quad (2.4)$$

We define the magnitude of the magnetic flux passing through a single hexagon ring of graphene in the unit of the quantum flux as  $\phi$ . Since the single hexagon ring has the area  $S_{\text{hex}} = \frac{3\sqrt{3}}{2} a^2$ , where  $a = 1.42\text{\AA}$  is the lattice constant of the graphite, the  $\phi$  is given as

$$\phi = \frac{BS_{\text{hex}}}{\phi_0}. \quad (2.5)$$

Here  $B = |\mathbf{B}|$ , and  $\phi = 1$  corresponds to  $7.9 \times 10^4 \text{T}$ . The cyclotron radius ( magnetic length ),  $l$ , is given by

$$l = \sqrt{\frac{ch}{eB}}. \quad (2.6)$$

Table 2.1: Some example values of the magnetic flux, magnetic field and cyclotron diameter.

Magnetic flux $\phi$	Magnetic Field $B$ [T]	Cyclotron diameter
1/100000	0.78	406.7a
1/10000	7.8	128.6a
1/1000	78	40.7a
1/100	780	12.8a

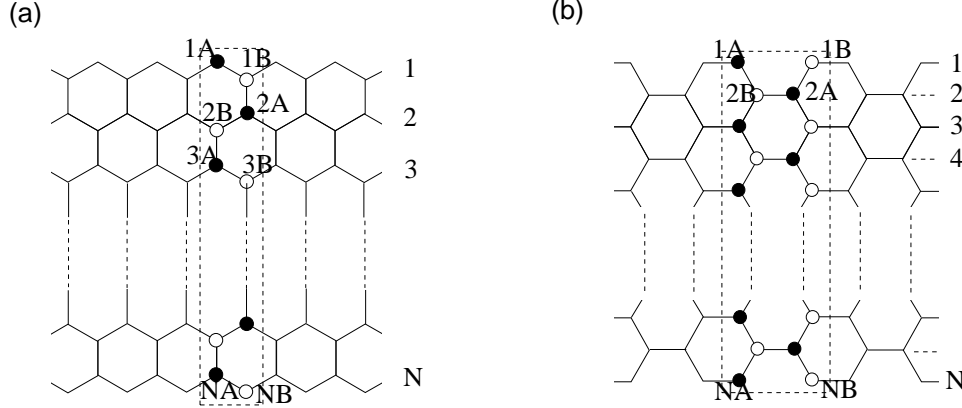


Figure 2.1: The structure of graphite ribbons with (a) zigzag edges and (b) armchair edges. The rectangle with the dashed line is the unit cell.

The some example values of the magnetic flux, magnetic field and cyclotron diameter is listed in Table 2.1.

The structure of graphite ribbons with zigzag and armchair edges are shown in Fig. 2.1, where we assume that all edge sites are terminated by hydrogen atoms. The ribbon width  $N$  is defined by the number of zigzag lines for the zigzag ribbon and by the number of dimer lines for the armchair ribbons. Since a hexagonal lattice can be divided by two sublattices, we call the A(B)-sublattice on the  $n$ -th zigzag or dimer line as  $nA$  ( $nB$ ) site. We use Landau gauge with  $\mathbf{A} = (0, Bx, 0)$ , where we define the translational invariant direction of each ribbon as the  $y$ -axis, and the  $x$ -axis lies perpendicular to  $y$ -axis. In this gauge, the unit cell of each ribbon can be taken as the rectangle shown in Fig. 2.1.

It should be noted that the same number  $N$  for both zigzag and armchair ribbons does not give the same ribbon width, when the ribbons are measured by the same unit of length. Therefore, when we compare physical quantities of zigzag and armchair ribbons with a same width  $W$ , we will use the following definition

$$W = \begin{cases} \frac{3}{2}Na - a & \equiv W_z & \text{zigzag ribbons} \\ (N-1)\frac{\sqrt{3}}{2}a & \equiv W_a & \text{armchair ribbons} \end{cases} \quad (2.7)$$

where  $a$  is the lattice constant.

In ribbon-shaped systems, the ratio between the width of a ribbon and cyclotron diameter effectively characterizes the electronic states of ribbon in a magnetic field. Therefore, we define the ratio between the ribbon width and the cyclotron diameter as the effective magnetic field  $\tilde{B}$  for a convenience, which is given by

$$\tilde{B} = \left(\frac{W}{d}\right)^2, \quad (2.8)$$

Table 2.2: Some example values of the graphene ribbon width.

$N$	Zigzag ribbon	Armchair ribbon
10	14.0a (2.0[nm])	7.8a (1.1[nm])
20	29.0a (4.1[nm])	16.5a (2.3[nm])
50	74.0a (10.5[nm])	42.4a (6.0[nm])
100	149.0a (21.2[nm])	85.7a (12.2[nm])
200	299.0a (42.5[nm])	172.3a (24.5[nm])

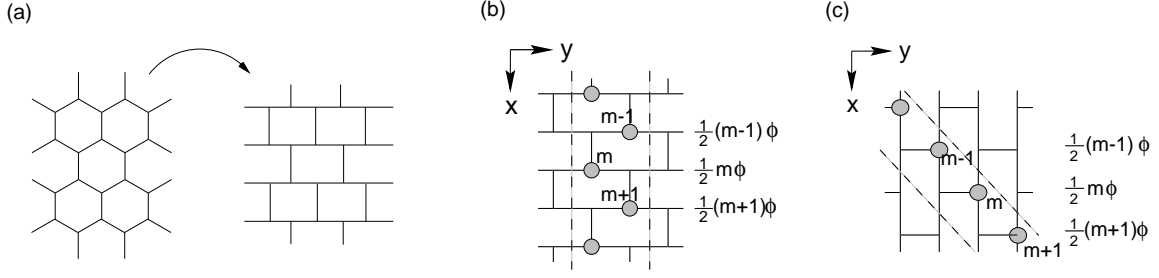


Figure 2.2: (a) The transformation from hexagonal lattice to brick type lattice, which does not change the lattice topology. The Peierls phase for Landau gauge on (b) zigzag ribbons and (c) armchair ribbons.

where  $d = 2l$ . Depending on the strength of the effective magnetic field  $\tilde{B}$ , we classify the system into three regions. First in the case of  $\tilde{B} < 1$  since the cyclotron diameter is larger than the ribbon width the cyclotron motion of electrons is disturbed, where the Landau levels are not formed. We call this region “weak magnetic field region”. Secondly in the case of  $\tilde{B} > 1$ , since the cyclotron diameter becomes smaller than the ribbon width the cyclotron motion of electrons is not disturbed except in the vicinity of ribbon edges, and the Landau levels appears. We call this region “strong magnetic field region”. Finally in the case of  $\tilde{B} \gg 1$ , where the cyclotron diameter is much smaller than the ribbon width and becomes the order of the lattice constant. In this situation, the topology of the lattice becomes important. We call this region “very strong magnetic field region”.

### 2.1.1 Harper’s equation

Let us adapt the Eq.(2.1) to the graphite lattice and derive the so called Harper equations [73,74]. In order to apply Eq.(2.1) to the graphite lattice and simplify the formulation, we introduce the lattice transformation as shown in Fig. 2.2 (a), which does not change the lattice topology. For convenience we adopt this brick-type lattice structure for labeling purpose.

The Peierls phase for the graphite ribbons is easily calculated from Eq.(2.3). The Peierls phase of graphite ribbons with (b) zigzag and (c) armchair ribbons is shown in Fig. 2.2. For both cases, the Peierls phase is given by  $\phi_{mB,nA} = \frac{1}{2}m\phi\delta_{mn}$  and otherwise zero, where  $\phi$  is the magnetic flux through a plaquette in units of a quantum flux.

Now, let us derive Harper’s equation, which possess the translational symmetry along the zigzag axis. In order to apply Eq.(2.1) to zigzag ribbons, we define a new operator,  $c_\alpha(i)$ , which create an electron on the site  $i$  in the unit cell  $\alpha$ . The momentum representation of this operator in the  $y$ -direction is defined by

$$c_\alpha(i) = \frac{1}{\sqrt{L}} \sum_k e^{ikr_\alpha} \gamma_k(i), \quad (2.9)$$

where  $r_\alpha$  represents the position of the unit cell  $\alpha$ . Here we also define a one-particle state

$$|\Psi(k)\rangle = \sum_m \left[ \Psi_{mA}(k) \gamma_k^\dagger(mA) + \Psi_{mB}(k) \gamma_k^\dagger(mB) \right] |0\rangle. \quad (2.10)$$

Inserting this one-particle state into Schrödinger equation  $H|\Psi\rangle = \epsilon|\Psi\rangle$ , we can easily obtain the following four eigenvalue equations for the sites mB, mA and (m+1)A,

$$\begin{aligned} \epsilon\Psi_{mB} &= \Psi_{(m+1)A} + e^{i2\pi\frac{m}{2}\phi}\Psi_{mA} + e^{-i2\pi\frac{m}{2}\phi}\Psi_{mA}, \\ \epsilon\Psi_{mA} &= \Psi_{(m-1)B} + e^{i2\pi\frac{m}{2}\phi}\Psi_{mB} + e^{-i2\pi\frac{m}{2}\phi}\Psi_{mB}, \\ \epsilon\Psi_{(m+1)A} &= \Psi_{mB} + e^{i2\pi\frac{m}{2}\phi}\Psi_{(m+1)B} + e^{-i2\pi\frac{m}{2}\phi}\Psi_{(m+1)B}. \end{aligned} \quad (2.11)$$

Eliminating the A-sublattice sites, we obtain the difference equation,

$$\lambda\Psi_m(k_y) = a_m\Psi_{m+1}(k_y) + b_m\Psi_m(k_y) + a_{m-1}\Psi_{m-1}(k_y), \quad (2.12)$$

where  $\lambda = \epsilon^2 - 3$ ,  $a_m(k_y) = 2\cos(\frac{k_y}{2} + m\pi\phi)$ ,  $b_m(k_y) = 2\cos(k_y + 2m\pi\phi)$ , and  $\Psi_{mB}$  was replaced by  $\Psi_m$ . Therefore, for a rational flux  $\phi = p/q$  ( $p$  and  $q$  being mutually prime integers), our problem was reduced to a one-dimensional tight binding model with a superlattice potential of period  $2q$ . Note that this equation

does not include any boundary conditions yet. It can be applied to both graphene ribbons and sheets by imposing the appropriate boundary conditions. In the following calculations, the factor  $m\pi\phi$  will be replaced by  $(\frac{N-1}{2} - m + 1)\pi\phi$  to keep the energy band symmetry about  $k = 0$  for arbitrary magnetic flux. This replacement means that the origin of the x-axis is set to the center of the ribbons.

The spectrum is confined to values of  $\lambda$  between  $-6$  and  $+6$ , i.e.  $-3 \leq \epsilon \leq +3$ . A close inspection shows that the following transformations do not change the energy spectrum;  $\epsilon \rightarrow -\epsilon$  and  $\phi \rightarrow \phi + n$ , where  $n$  is an arbitrary integer. For rational flux  $\phi = \frac{p}{q}$ ,  $a_m$  is a function with period  $2q$  and  $b_m$  is a function with period  $q$ . In addition, we must pay attention to the following symmetry of the energy bands in the Brillouin zone,

$$\epsilon\left(k_y + \frac{2\pi}{q}n\right) = \epsilon(k_y). \quad (2.13)$$

Here we should again note that these arguments do not depend on the boundary conditions.

Similarly, we can also derive the Harper equations which includes the translational symmetry along the armchair axis. In the same way as Eq.(2.12) the following equation is obtained,

$$\lambda\Psi_m(k_y) = \Psi_{m+2}(k_y) + a_m\Psi_{m+1}(k_y) + a_m\Psi_{m-1}(k_y) + \Psi_{m-2}(k_y) \quad (2.14)$$

where  $\lambda = \epsilon^2 - 3$ ,  $a_m(k_y) = 2\cos(\frac{k_y}{2} + (m - \frac{1}{2})\pi\phi)e^{-i\frac{\pi}{2}\phi}$ . It is easy to confirm that the same symmetry properties as for Eq.(2.14) apply here too. Similarly, the factor  $a_m$  will be replaced by  $a_m(k_y) = 2\cos(\frac{k_y}{2} + (\frac{N-1}{2} - 2m + 3)\pi\phi)e^{-i\pi\phi}$  in order to obtain the symmetric energy band structure about  $k = 0$  for arbitrary magnetic flux.

### 2.1.2 The $\mathbf{k} \cdot \mathbf{p}$ equation

In the vicinity of the K point of the 1st BZ of graphene sheet, the energy band has a conical structure, i.e.  $\mathbf{k}$ -linear dispersion or massless spectrum. Since a graphene sheet is a half-filled system, the Fermi level is at the center of this spectrum. Thus the massless Dirac equation or so-called  $\mathbf{k} \cdot \mathbf{p}$  equation becomes a powerful tool to describe the low-energy electronic states of a graphite or graphite-related materials. Here we derive the  $\mathbf{k} \cdot \mathbf{p}$  equation [37, 75–80], and use this for the discussions on the behaviors of electronic states of a graphene sheet in weak magnetic fields and the electronic states of graphene ribbons near the Fermi energy.

Let us derive the  $\mathbf{k} \cdot \mathbf{p}$  equation. In the following, we use  $\sqrt{3}a$  as unit of length instead of the lattice constant and the definition of axis is given in Fig.2.3. We introduce a wave vector  $\mathbf{k}$  measured from the K point and consider the set of functions

$$\phi_{i\mathbf{K}}(\mathbf{r}) = \exp(i\mathbf{k} \cdot \mathbf{r})\Psi_{i\mathbf{K}}(\mathbf{r}), \quad (2.15)$$

with  $i = A, B$ .  $\Psi_{A\mathbf{K}}$  ( $\Psi_{B\mathbf{K}}$ ) represents the Bloch function. The wave function near K point can be expanded as

$$\psi(\mathbf{r}) = \sum_{i=A,B} \int \frac{d\mathbf{k}^2}{(2\pi)^2} C^i(\mathbf{k})\phi_{i\mathbf{K}}(\mathbf{r}) = \sum_{i=A,B} F_i^{\mathbf{K}}(\mathbf{r})\Psi_{i\mathbf{K}}(\mathbf{r}), \quad (2.16)$$

where  $F_i^{\mathbf{K}}(\mathbf{r})$  is the envelope function defined by

$$F_{\mathbf{K}}^i(\mathbf{r}) = \int \frac{d\mathbf{k}^2}{(2\pi)^2} \exp(\mathbf{k} \cdot \mathbf{r})C^i(\mathbf{k}). \quad (2.17)$$

Substituting eq.(2.16) into the Schrödinger equation, we obtain the following  $2 \times 2$   $\mathbf{k} \cdot \mathbf{p}$  equation near K point:

$$\begin{pmatrix} 0 & \hat{k}_x - i\hat{k}_y \\ \hat{k}_x + i\hat{k}_y & 0 \end{pmatrix} \begin{pmatrix} F_A^{\mathbf{K}}(\mathbf{r}) \\ F_B^{\mathbf{K}}(\mathbf{r}) \end{pmatrix} = \epsilon \begin{pmatrix} F_A^{\mathbf{K}}(\mathbf{r}) \\ F_B^{\mathbf{K}}(\mathbf{r}) \end{pmatrix}, \quad (2.18)$$

where  $\hat{\mathbf{k}}$  is a wave vector operator defined by

$$\hat{\mathbf{k}} = -i\nabla + \frac{e}{c\hbar}\mathbf{A}. \quad (2.19)$$

Effects of a magnetic field are included by the vector potential  $\mathbf{A}$  appearing in the above operator [76, 81, 82].

Similarly, the  $\mathbf{k} \cdot \mathbf{p}$  Hamiltonian near  $\mathbf{K}'$  point is given by

$$\begin{pmatrix} 0 & \hat{k}_x + i\hat{k}_y \\ \hat{k}_x - i\hat{k}_y & 0 \end{pmatrix} \begin{pmatrix} F_A^{\mathbf{K}'}(\mathbf{r}) \\ F_B^{\mathbf{K}'}(\mathbf{r}) \end{pmatrix} = \epsilon \begin{pmatrix} F_A^{\mathbf{K}'}(\mathbf{r}) \\ F_B^{\mathbf{K}'}(\mathbf{r}) \end{pmatrix}. \quad (2.20)$$

It is noted that eqs. (2.18) and (2.20) are rewritten in terms of Pauli matrix  $\boldsymbol{\sigma} = (\sigma_x, \sigma_y)$  as

$$(\sigma_x \hat{k}_x + \sigma_y \hat{k}_y) \mathbf{F}_{\mathbf{K}}(\mathbf{r}) = \epsilon \mathbf{F}_{\mathbf{K}}(\mathbf{r}) \quad (2.21)$$

$$(\sigma_x \hat{k}_x - \sigma_y \hat{k}_y) \mathbf{F}_{\mathbf{K}'}(\mathbf{r}) = \epsilon \mathbf{F}_{\mathbf{K}'}(\mathbf{r}) \quad (2.22)$$

These equations have the same form as Weyl's equation for neutrinos.

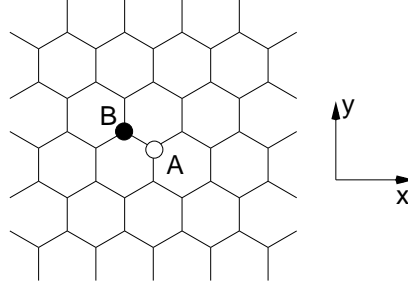
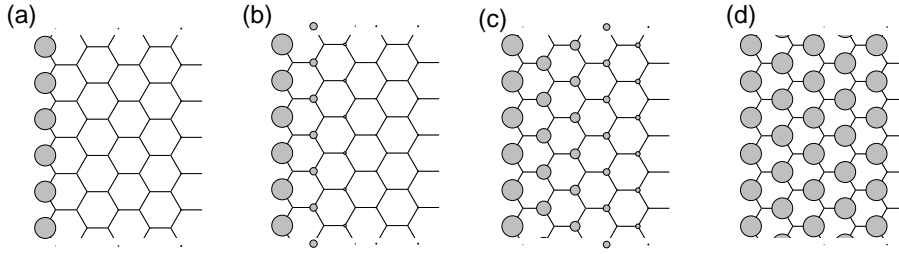


Figure 2.3: A set of notations for the derivation of k-p equation of a graphene sheet

Figure 2.4: The charge density of the edge state at (a)  $k = \pi$ , (b)  $k = \frac{8}{9}\pi$ , (c)  $k = \frac{7}{9}\pi$  and (d)  $k = \frac{2}{3}\pi$ , where the radius of the circle means the magnitude of the charge density.

## 2.2 Edge States

As we have mentioned in the previous chapter, the band structure of zigzag ribbons has partially flat bands at the Fermi energy, corresponding to strongly localized states at the zigzag edges (edge states). Here we show that it is possible to derive the edge state by solving Harper's equation (2.12), which is useful for the extension to cases including magnetic fields.

At the beginning, let us rewrite the Eq.(2.12) to the transfer matrix form,

$$\begin{pmatrix} \Psi_{m+1} \\ \Psi_m \end{pmatrix} = \begin{pmatrix} \frac{1}{a_m} (\lambda - \tilde{b}_m) & \frac{a_{m-1}}{a_m} \\ 1 & 0 \end{pmatrix} \begin{pmatrix} \Psi_m \\ \Psi_{m-1} \end{pmatrix}, \quad (2.23)$$

where  $\tilde{b}_m$  is  $b_m - 1$  for  $m = 1, N$  and  $b_m$  for others. We take open boundary conditions,

$$\begin{pmatrix} \Psi_1 \\ \Psi_0 \end{pmatrix} = \begin{pmatrix} 1 \\ 0 \end{pmatrix} \quad (2.24)$$

and impose the condition  $\varepsilon = 0$ . Then, one obtains,

$$\Psi_n = D_k^{n-1}, \quad (2.25)$$

where  $D_k$  is  $-2 \cos(\frac{k}{2})$ . The convergence condition  $|D_k| \leq 1$  is required, because otherwise the wave function would diverge in the semi-infinite graphite sheet. This convergence condition defines the region  $\frac{2}{3}\pi \leq k \leq \pi$ , where the partly flat bands exist. The charge density is shown in Fig. 2.4 at (a)  $k = \pi$ , (b)  $\pi$ , (c)  $\pi$  and (d)  $\frac{2}{3}\pi$ . At  $k = \pi$ , the charge is perfectly localized at the zigzag edge. When the wave number deviates from  $k = \pi$ , the electron states gradually penetrate towards the inner sites. Finally, the electron states completely extend at  $k = \frac{2}{3}\pi$ .

Next, we discuss the DOS of the edge state in the absence of a magnetic field, which will be used in the calculation of the Pauli susceptibility of zigzag ribbons in the next chapter. As we have seen in this section, the edge state penetrate to inner sites when the wave number changes from  $\pi$  to  $\frac{2}{3}\pi$ . If we consider the graphite ribbons with width  $N$ , two edge states which come from both side of edge will overlap with each other and develop the bonding and anti-bonding configurations. Since the magnitude of the overlap becomes larger when the wave number approaches  $\frac{2}{3}\pi$ , the band gap between the bonding and anti-bonding state formed by the two edge states gets larger toward  $k = \frac{2}{3}\pi$ . Therefore the partly flat bands acquire a slight dispersion which depends on the ribbon width  $N$ . In order to calculate the DOS, we first have to derive the energy dispersion for the

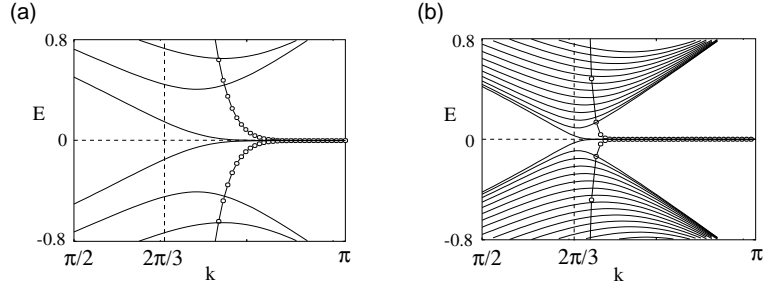


Figure 2.5: The band structure near  $E = 0$  for (a)  $N = 10$ , (b)  $N = 50$ . The solid lines represent the bands calculated in the tight binding model and the solid lines with circles represent the bands are calculated by Eq.(2.30).

edge states. The energy dispersion is calculated by the overlapping of two edge states. From Eq.(2.25), the amplitude of the edge state which penetrates from the first zigzag line is given by

$$\Psi_n = D_k^{n-1} \equiv \Psi_A, \quad (2.26)$$

which is located only on the A-sublattice. On the other hand, the amplitude of the edge state which penetrate from  $N^{th}$  zigzag line, is given by

$$\Psi_{N-n} = D_k^{n-1} \equiv \Psi_B, \quad (2.27)$$

which is located only on the B-sublattice. By using the tight binding Hamiltonian, the overlapping of two edge states is easily calculated,

$$\langle \Psi_A | H | \Psi_B \rangle = N D_k^{N-1} (-2t - t D_k) = T_k, \quad (2.28)$$

where  $D_k = -2 \cos(\frac{k}{2})$ . Therefore, the energy spectrum of the edge states in lowest order perturbation in the overlap is given by the following eigenvalue problem.

$$\begin{pmatrix} 0 & T_k \\ T_k & 0 \end{pmatrix} \begin{pmatrix} C_1 \\ C_2 \end{pmatrix} = \epsilon_k \begin{pmatrix} C_1 \\ C_2 \end{pmatrix} \quad (2.29)$$

By diagonalization of this Hamiltonian matrix, we find the energy spectrum

$$E_k = -2t N D_k^{N-1} \left[ 1 - \cos\left(\frac{k}{2}\right) \right]. \quad (2.30)$$

From this equation, around  $k = \pi$ , the spectrum is given by  $E \sim k^N$ . The energy dispersion of Eq.(2.30) is compared with the band structures calculated in the tight binding model in Fig.2.5. Therefore, the DOS related to the edge states has the form,

$$\rho(\epsilon) = \frac{\partial k}{\partial \epsilon} \sim \frac{1}{N} \epsilon^\alpha, \quad (2.31)$$

where  $\alpha = \frac{1}{N} - 1$ . Note that this DOS has a power-law dependence, which is different from the ordinary van Hove singularity of  $\rho \sim \frac{1}{\sqrt{E}}$  observed in one-dimensional system. It is also found that the renormalized DOS is inversely proportional to the ribbon width, which has been confirmed by numerical calculation. [39]

## 2.3 Energy Gap

In this section, we analytically show that both the direct gap  $\Delta_a$  at  $k = 0$  of sufficiently wide armchair ribbons and the direct gap  $\Delta_z$  at  $k = \frac{2\pi}{3}$  of sufficiently wide zigzag ribbons are inversely proportional to the width of graphite ribbon  $W$ . This result supports that the physical quantities related to the energy gap can be scaled by the ribbon width  $W$ .

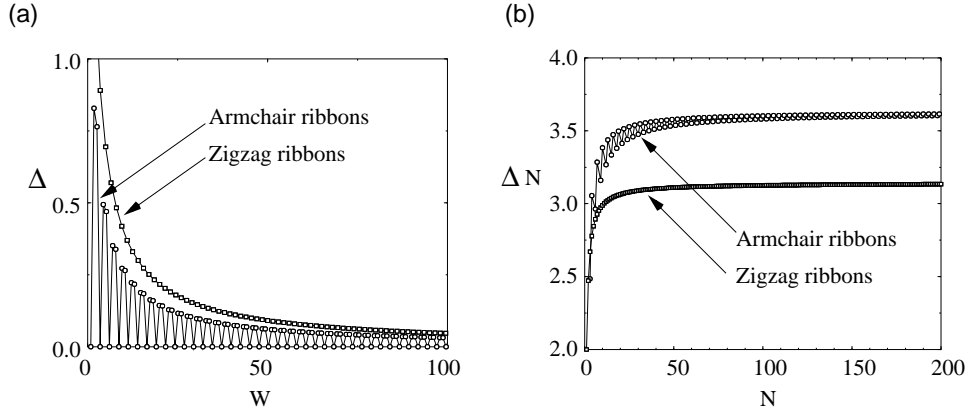


Figure 2.6: (a) The width dependence of the energy gap of armchair ribbons at  $k = 0$  and zigzag ribbons at  $k = \frac{2\pi}{3}$ . (b) The plot of  $\Delta N$  versus  $N$ .

### Energy gap of armchair ribbons at $k = 0$

We examine the energy gap  $\Delta_a$  at  $k = 0$  of armchair ribbons. It is easy to find that at  $k = 0$  the Hamiltonian can be rewritten as

$$H = -t \sum_{j=1}^N \left[ \sum_{\mu=1}^2 (a_{j,\mu}^\dagger a_{j+1,\mu} + h.c.) + a_{j,1}^\dagger a_{j,2} + h.c. \right], \quad (2.32)$$

which is equivalent to the tight binding model for the 2-leg ladder lattice having  $N$  rungs [31,32]. The site indices  $(j,1)$  and  $(j,2)$  correspond to the  $jA(B)$  and  $jB(A)$  sites, respectively, when  $j$  is even(odd). The eigenvalues are evaluated as

$$\epsilon^\pm = -2t \cos\left(\frac{n\pi}{N+1}\right) \pm t \quad (n = 1, 2, \dots, N), \quad (2.33)$$

the corresponding eigenfunctions are

$$\Psi_{j\mu} = (\mp)^{\mu+1} B \sin\left(\frac{nj\pi}{N+1}\right), \quad (2.34)$$

where  $\Psi_{j\mu}$  is the wavefunction at  $(j, \mu)$ -site and  $B$  is the normalization factor. The system is metallic only when  $N = 3m - 1$ , because  $\epsilon^+$  and  $\epsilon^-$  become zero for  $n = m$  and  $2m$ , respectively. Note that every third rung has a zero node in the wavefunction when  $N = 3m - 1$ . Thus,  $\Delta_a$  are given as,

$$\Delta_a = \begin{cases} 0 & N = 3m - 1 \\ 2 \left[ 2t \cos\left(\frac{m}{3m+1}\pi\right) - t \right] & N = 3m \\ 2 \left[ 2t \cos\left(\frac{m+1}{3m+2}\pi\right) - t \right] & N = 3m + 1 \end{cases}. \quad (2.35)$$

After the elimination of  $N$  in terms of  $W = (N-3)\frac{\sqrt{3}}{2} + \sqrt{3}$  and the Taylor expansion under the condition of  $1/W \ll 1$ , we can obtain the following results.

$$\Delta_a \sim \begin{cases} 0 & N = 3M - 1 \\ \frac{\pi}{W + \frac{\sqrt{3}}{2}} & N = 3M \\ \frac{\pi}{W} & N = 3M + 1 \end{cases} \quad (2.36)$$

Thus the  $\Delta_a$  is inversely proportional to the ribbon width.

### Energy gap of zigzag ribbons at $k = \frac{2}{3}\pi$

Since in the zigzag ribbons two states are degenerate at  $k = \pi$ , the gap of the zigzag ribbons is always zero and the system is always metallic. However, as we have seen in the previous section the energy bands have a gap at  $k = \frac{2}{3}\pi$ , because the bonding and anti-bonding configuration between two edge states coming from both edges

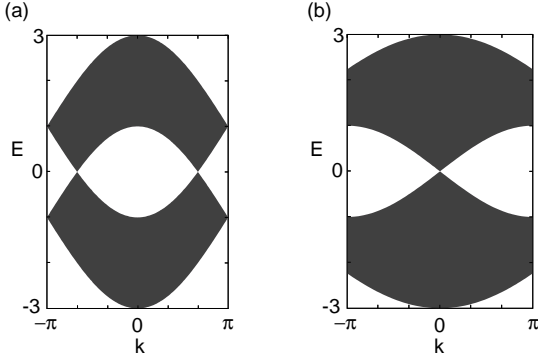


Figure 2.7: The energy band structure of graphite sheet projected to (a) zigzag axis and (b) armchair axis in the absence of magnetic field.

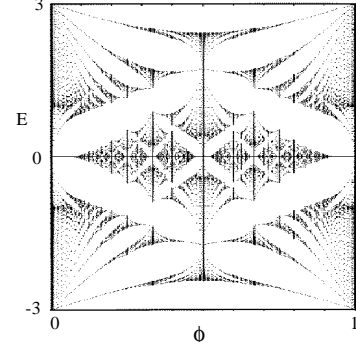


Figure 2.8: The energy spectrum of the graphite sheet in a magnetic field.

is developed toward  $k = \frac{2}{3}\pi$  from  $k = \pi$ . According to the projection of the band structure of a graphene sheet onto the 1st BZ of zigzag ribbons, the degenerate points of valence and conduction band of a graphene sheet ties at  $k = \frac{2}{3}\pi$ . Thus in the limit of infinite ribbon width the energy gap  $\Delta_z$  at  $k = \frac{2}{3}\pi$  has to be zero. The Hamiltonian of zigzag ribbons at  $k = \frac{2}{3}\pi$  is rewritten as

$$H = -t \sum_{i=1}^{2N} (a_i^\dagger a_{i+1} + h.c.), \quad (2.37)$$

which is equivalent to the tight binding model for the one-dimensional lattice having  $2N$  sites. The site index  $i$  corresponds to  $iA$ , if  $i$  is an odd number, and to  $iB$ , if  $i$  is an even number. The eigenvalues are evaluated as  $\epsilon = -2t \cos\left(\frac{n\pi}{2N+1}\right)$  ( $n=1,2,\dots,2N$ ) and the corresponding eigenfunction at the  $j^{\text{th}}$  site,  $\Psi_j$ , is evaluated as  $\Psi_j = B \sin\left(\frac{nj\pi}{2N+1}\right)$ , where  $B$  is the normalization factor. Therefore,  $\Delta_z$  is given as,

$$\Delta_z = 4t \cos\left(\frac{N}{2N+1}\pi\right). \quad (2.38)$$

Taylor expansion under the condition of  $1/N \ll 1$ , we can obtain the following results.

$$\Delta_z \sim \frac{\pi}{N} = \frac{3\pi}{2} \frac{1}{W+1}. \quad (2.39)$$

Thus the  $\Delta_a$  is also inversely proportional to the ribbon width.

In Fig.2.6(a), the width dependence of the energy gap is shown for both armchair and zigzag ribbons. Figure2.6(b) shows the plot of  $N$  times the gap  $\Delta$ ,  $N\Delta$ , versus  $N$ . The  $N\Delta$  becomes constant for values more than about  $N = 30$  ( $N = 60$ ) for zigzag (armchair) ribbons.

## 2.4 Graphene Sheet in a Magnetic Field

In this section, we consider the electronic structures of a graphene sheet in a magnetic field. This will afterwards become the basis to discuss the electronic structures of graphene ribbons.

### 2.4.1 Harper's equation approach

As we have seen in the previous section, the tight binding model of the graphite lattice in a magnetic field could be reduced to a tight binding model with superlattice potential of period  $2q$ . In order to calculate the energy spectrum of the graphene sheet, we must treat the eigenvalue problem of a  $2q \times 2q$  matrix with the periodic boundary condition  $\Psi_{2q+1} = e^{ik_x 2q} \Psi_1$ , when the Brillouin zone is reduced to the magnetic Brillouin zone  $-\frac{\pi}{2q} \leq k_x \leq \frac{\pi}{2q}$  and  $-\pi \leq k_y \leq \pi$ .

At the beginning, we consider the zero-field energy band of the graphite sheet. By setting  $\phi = 0$  in Eqs.(2.12) and (2.14), the zero-field spectrum is easily obtained. From Eq.(2.12), we find for the graphite sheet with translational symmetry along zigzag axis,

$$\epsilon_{\mathbf{k}} = \pm \sqrt{3 + 2 \cos(k_y) + 4 \cos\left(\frac{k_y}{2}\right) \cos(k_x)}. \quad (2.40)$$

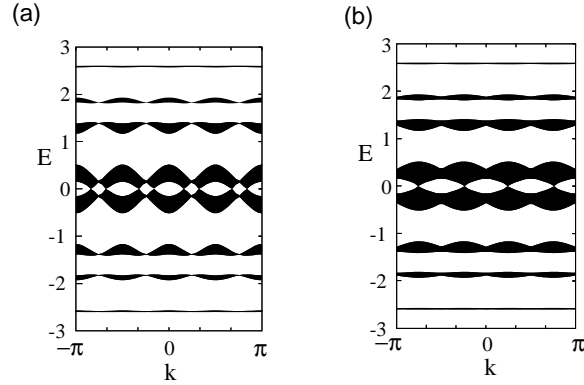


Figure 2.9: The energy band structure of graphite sheet projected to (a) zigzag axis and (b) armchair axis for  $\phi = 1/4$ .

Similarly, from Eq.(2.14), the zero-field spectrum of graphites with translational symmetry along the armchair axis is

$$\epsilon_{\mathbf{k}} = \pm \sqrt{3 + 2 \cos(2k_x) + 4 \cos\left(\frac{k_y}{2}\right) \cos(k_x)}. \quad (2.41)$$

The energy band structures for both Eqs.(2.40) and (2.41) are shown in Fig. 2.7, where  $k_y$  is replaced by  $k$  and we have superposed all  $k_x$ -values in the spectrum. Of course, same as the case of the projection of the energy band, the K-point degeneracy of the band structure of the graphite sheet come to at  $k = \frac{2}{3}\pi$  ( $k = 0$ ) for zigzag (armchair) ribbons.

The spectrum of the graphite sheet in a magnetic field is shown in Fig. 2.8, which was first calculated by Rammal [83]. We can easily find that the spectrum has the same fine recursive structure as the famous Hofstadter butterfly<sup>1</sup> [84]. In the weak-magnetic field limit, we can clearly see the Landau levels. When the magnetic flux is getting larger, these levels form the Landau subbands because of the Harper broadening [74, 91–93]. As we pointed out in the previous section, for the rational flux  $\phi = \frac{p}{q}$ , we can see  $2q$  subbands with a reflection symmetry about  $\epsilon = 0$  and about  $\phi = \frac{1}{2}$ . Interestingly, the degeneracy at  $\epsilon = 0$  exists for arbitrary flux, which confirms that the degeneracy at the K and K' points is not destroyed.

As an example of the energy band structure in a strong magnetic field, we show the case of the graphite sheet projected to the (a) zigzag axis and (b) armchair axis for  $\phi = 1/4$  (Fig. 2.9). In a strong magnetic field, the Landau levels change to  $2 \times 4$  subbands due to Harper broadening and the effect of the lattice structure gets more important, so that each subband has the basic structure of the zero field case. Furthermore we find the symmetry  $\epsilon\left(k_y + \frac{2\pi}{q}n\right) = \epsilon(k_y)$ .

### 2.4.2 $\mathbf{k} \cdot \mathbf{p}$ equation approach

Next let us turn our attention to the electronic states of graphene sheet in a weak magnetic field, following McClure<sup>2</sup> [77, 80]. In the description of the Harper equation, the weak magnetic field corresponds to very large  $q$ , resulting in it becomes hard to treat because the number of sites in the unit cell becomes quite large. In a such situation, the  $\mathbf{k} \cdot \mathbf{p}$  equation is a powerful tool, because we can treat the magnetic field within the continuum approximation.

We start with  $\mathbf{k} \cdot \mathbf{p}$  equation. At the beginning, we introduce the ladder operators

$$\hat{L}_{\pm} = \frac{l}{\sqrt{2}} \left( \hat{k}_x \pm i\hat{k}_y \right) \quad (2.42)$$

where  $l = \sqrt{\frac{c\hbar}{eB}}$  is magnetic length. Then, the  $\mathbf{k} \cdot \mathbf{p}$  Hamiltonian is rewritten as

$$\hat{H}_{\pm} = \begin{pmatrix} 0 & \sqrt{2}t\hat{L}_{\mp}/l \\ \sqrt{2}t\hat{L}_{\mp}/l & 0 \end{pmatrix} \quad (2.43)$$

<sup>1</sup>Although the problem of two-dimensional electrons in a magnetic field is an old one and it shows extremely rich and interesting behaviors. The energy spectrum for various lattice structures are studied by several authours [85–88]. This problem has been also studied in the context of the quantized Hall conductance of the two dimension [89, 90].

<sup>2</sup>For the Landau level structure of three-dimensional graphite based on the SW model [37], see reference [94]

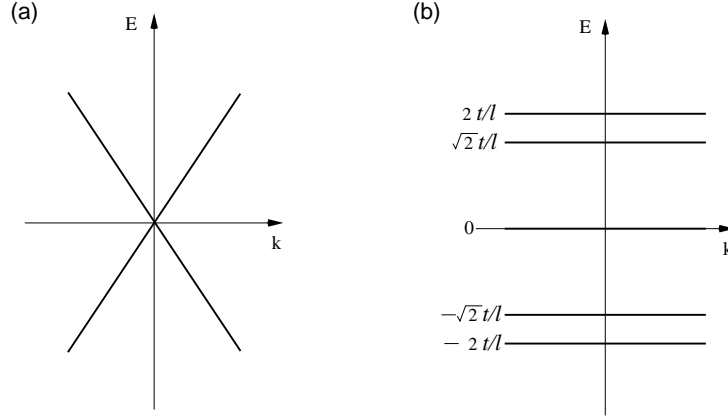


Figure 2.10: The energy bands of a graphene sheet near the K and K' points in the absence (a) and presence (b) of a magnetic field.

where upper and lower signs correspond to K and K' points, respectively. This Hamiltonian leads to the presence of a Landau level with a vanishing energy eigenvalue. For the Landau gauge  $(0, Bx)$ , we have

$$\epsilon_{2D} = 0, \quad \mathbf{F}_{\mathbf{K}} = \frac{1}{\sqrt{L_y}} \exp(ik_y y) \begin{pmatrix} 0 \\ h_0 \end{pmatrix} \quad \text{K - point}, \quad (2.44)$$

$$\epsilon_{2D} = 0, \quad \mathbf{F}_{\mathbf{K}'} = \frac{1}{\sqrt{L_y}} \exp(ik_y y) \begin{pmatrix} h_0 \\ 0 \end{pmatrix} \quad \text{K' - point}, \quad (2.45)$$

with  $L_y$  and  $k_y$  being the system size and the wave vector, respectively, in the  $y$  direction. Other Landau levels are given by

$$\epsilon_{2D} = \pm \sqrt{2}t \frac{\sqrt{n+1}}{l}, \quad \mathbf{F}_{\mathbf{K}} = \frac{1}{\sqrt{2L_y}} \exp(ik_y y) \begin{pmatrix} \pm h_n \\ h_{n+1} \end{pmatrix} \quad n = 0, 1, 2, \dots \quad \text{K - point}, \quad (2.46)$$

$$\epsilon_{2D} = \pm \sqrt{2}t \frac{\sqrt{n+1}}{l}, \quad \mathbf{F}_{\mathbf{K}'} = \frac{1}{\sqrt{L_y}} \exp(ik_y y) \begin{pmatrix} \pm h_{n+1} \\ h_n \end{pmatrix} \quad n = 0, 1, 2, \dots \quad \text{K' - point}, \quad (2.47)$$

where upper and lower signs correspond to conduction and valence bands, respectively, and  $h_n$  is the harmonic oscillator eigenfunctions written as

$$h_n = \frac{i^n}{\sqrt{2^n n! \sqrt{\pi} l}} \exp \left[ -\frac{1}{2} \left( \frac{x + l^2 k_y}{l} \right)^2 \right] H_n \left( \frac{x + l^2 k_y}{l} \right) \quad (2.48)$$

with the Hermite polynomial  $H_n(x)$ . These eigenfunctions have the properties:

$$\hat{L}_+ \hat{L}_- h_n = n h_n, \quad \hat{L}_+ h_n = \sqrt{n+1} h_{n+1}, \quad \hat{L}_- h_n = \sqrt{n} h_{n-1}. \quad (2.49)$$

Figure 2.10 shows the energy levels of a graphene sheet near the K and K' points in the presence and absence of a magnetic field. An important point here is that the 0-th Landau level always remains at  $E = 0$ . This is the origin of the large diamagnetic susceptibility of graphite, which will be discussed in the next chapter.

## 2.5 Graphene Ribbon in Magnetic Field

The energy band structures of graphene ribbons are obtained in terms of the Harper's equation by imposing open boundary conditions. In the case of zigzag ribbons with width  $N$ , the boundary condition is  $\Psi_{N+1} = \Psi_0 = 0$ . However, we need a more careful treatment of Harper's equation at the edge site. In Eqs.(2.12), it was not considered that there would be no 0A(B) and (N+1)A(B) site. Including this fact, for  $m = 1$  and  $N$ , Eq.(2.12) has to be rewritten as

$$\lambda \Psi_m(k_y) = a_m \Psi_{m+1}(k_y) + (b_m - 1) \Psi_m(k_y) + a_{m-1} \Psi_{m-1}(k_y). \quad (2.50)$$

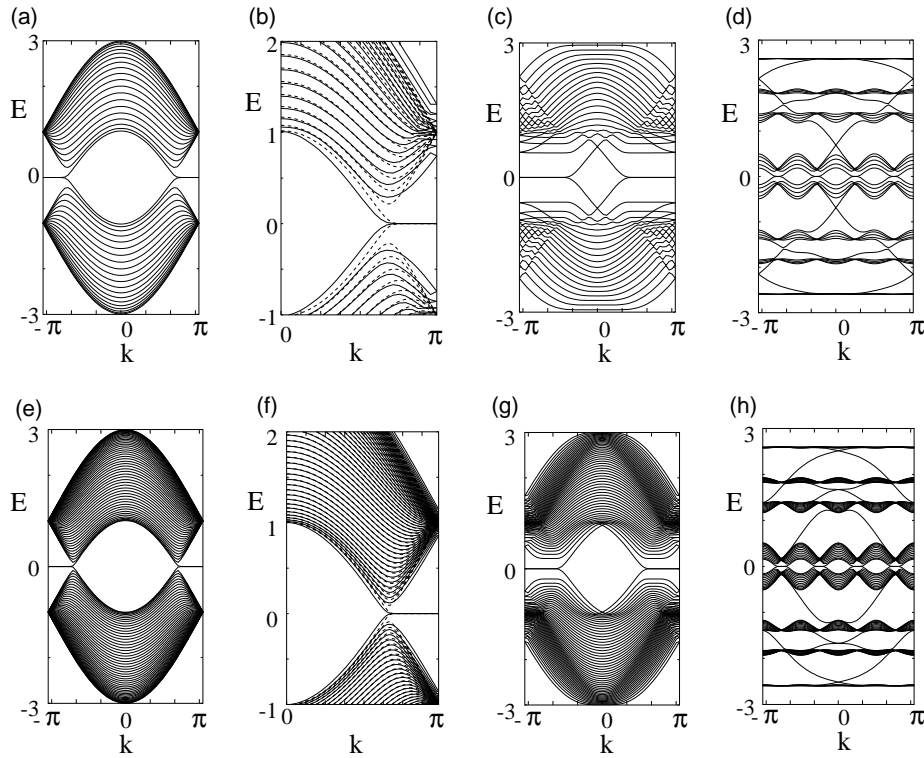


Figure 2.11: The energy band structures of zigzag ribbon for (a)  $\tilde{B} = 0$ , (b)  $\tilde{B} = 4$ , (c)  $\tilde{B} = 16$  and (d)  $\phi = \frac{1}{4}$  for  $N = 10$ . The energy band structures of zigzag ribbon for (e)  $\tilde{B} = 0$ , (f)  $\tilde{B} = 4$ , (g)  $\tilde{B} = 16$  and (h)  $\phi = \frac{1}{4}$  for  $N = 50$ . The dashed lines in (b) and (f) are the energy band structures at  $\tilde{B} = 0$  for comparison.

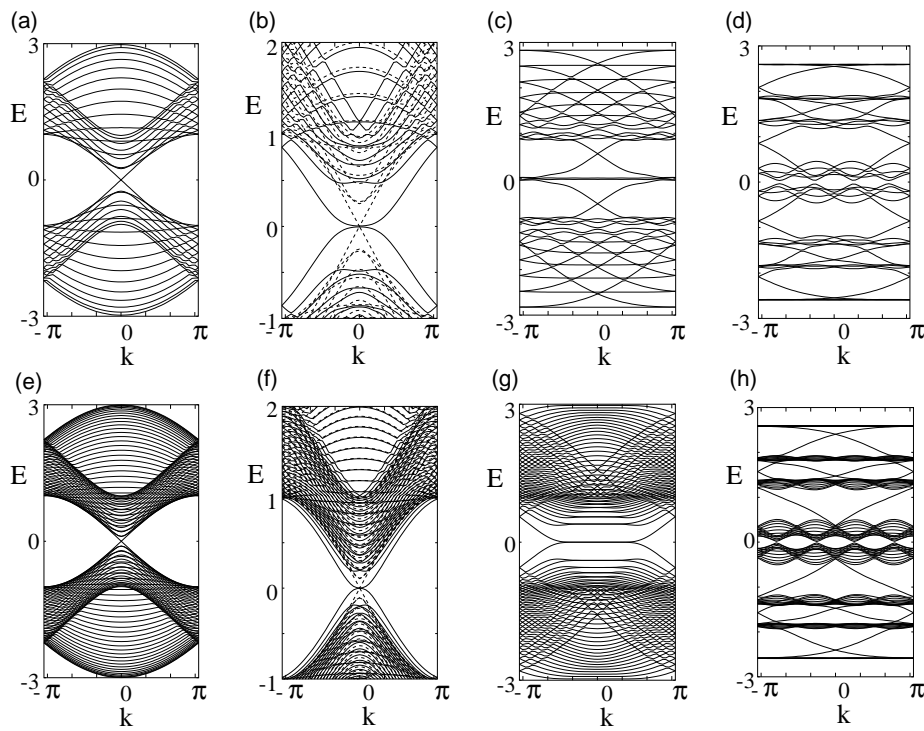


Figure 2.12: The energy band structures of armchair ribbon for (a)  $\tilde{B} = 0$ , (b)  $\tilde{B} = 4$ , (c)  $\tilde{B} = 16$  and (d)  $\phi = \frac{1}{4}$  for  $N = 10$ . The energy band structures of armchair ribbon for (e)  $\tilde{B} = 0$ , (f)  $\tilde{B} = 4$ , (g)  $\tilde{B} = 16$  and (h)  $\phi = \frac{1}{4}$  for  $N = 50$ . The dashed lines in (b) and (f) are the energy band structures at  $\tilde{B} = 0$  for comparison.

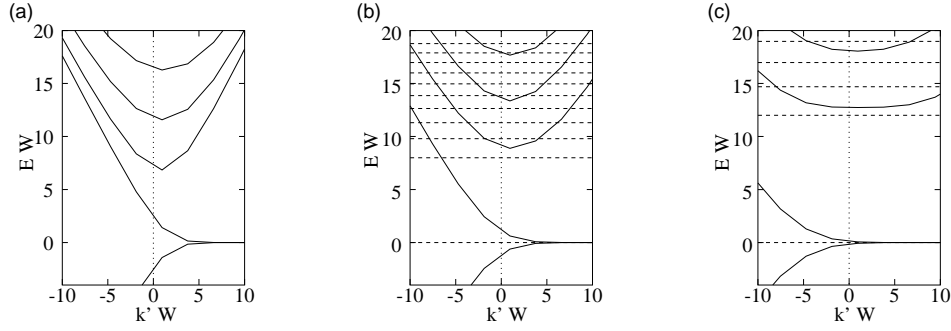


Figure 2.13: The scaled energy band structures of zigzag ribbons near  $k = 2\pi/3$  for (a)  $\tilde{B} = 0$ , (b)  $\tilde{B} = 4$  and (c)  $\tilde{B} = 16$ . Bold lines are dispersions of zigzag ribbons. Here  $k'$  means the wave number measured from  $k = 2\pi/3$ . The dotted lines are the corresponding Landau levels of graphene sheet for comparison.

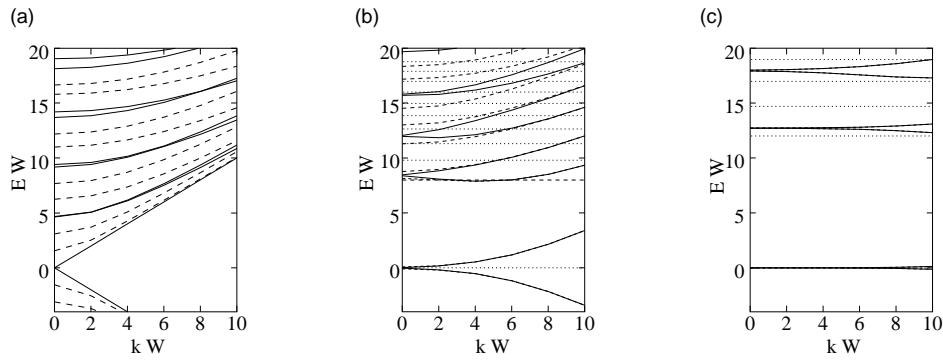


Figure 2.14: The scaled energy band structures of armchair ribbons near  $k = 0$  for (a)  $\tilde{B} = 0$ , (b)  $\tilde{B} = 4$  and (c)  $\tilde{B} = 16$ . Bold lines are metallic armchair ribbons ( $N = 3m - 1$ ) and dashed lines are semiconducting armchair ribbons ( $N \neq 3m - 1$ ). The dotted lines are the corresponding Landau levels of graphene sheet for comparison.

Therefore we must replace  $b_1$  ( $b_N$ ) by  $b_1 - 1$  ( $b_N - 1$ ) in Eq.(2.12) in order to include the condition that the 0A and  $(N+1)A$  sites do not exist. Similarly, for the armchair ribbons, the boundary condition is  $\Psi_{N+1} = \Psi_0 = 0$ , where we must replace  $b_1$  ( $b_N$ ) by  $b_1 - 1$  ( $b_N - 1$ ) in order to include the condition that the 0A and  $(N+1)A$  sites do not exist.

In Fig.2.11, it is shown that the energy band structures of zigzag ribbon of  $N = 10$  for (a)  $\tilde{B} = 0$ , (b)  $\tilde{B} = 4$ , (c)  $\tilde{B} = 16$  and (d)  $\phi = \frac{1}{4}$ , and the energy band structures of zigzag ribbon  $N = 50$  for (e)  $\tilde{B} = 0$ , (f)  $\tilde{B} = 4$ , (g)  $\tilde{B} = 16$  and (h)  $\phi = \frac{1}{4}$ . In Fig.2.11 (b) and (f), the dashed lines are the energy band structures at  $\tilde{B} = 0$  for comparison. For  $\phi = 0$ , the profile of band structure has almost the same structure as in the case of the graphene sheet as shown in Fig. 2.7(a). As we have discussed in the previous section, the partly flat bands at  $E = 0$  originate from the edge states.

In the weak magnetic field region of  $\tilde{B} = 4$ , the Landau levels are not perfectly formed and the band structure at  $\phi = 0$  is almost unchanged, because the edges interrupt the cyclotron motion of the electron (Fig. 2.11 (b),(f)). For the strong magnetic field region of  $\tilde{B} = 16$ , where the ribbon width is sufficiently wide compared with the cyclotron radius, the Landau levels are nearly developed (Fig. 2.11 (c),(g)).

As an example for  $q \ll N$  and high commensurates, we show the energy band structure of  $\phi = \frac{1}{4}$  in Fig. 2.11 (d),(h). The  $2 \times 4$ -Landau subbands are formed. Between the Landau subbands, we can see the additional dispersion. The states of these dispersions are also localized at the edge [95–97], which originate from the cyclotron motion of electrons. It should be noted that the partly flat bands are formed at  $E = 0$  again.

Figure 2.12 shows the energy band structures of the armchair ribbon of  $N = 10$  for (a)  $\tilde{B} = 0$ , (b)  $\tilde{B} = 4$ , (c)  $\tilde{B} = 16$  and (d)  $\phi = \frac{1}{4}$ , and the energy band structures of the armchair ribbon with  $N = 50$  for (e)  $\tilde{B} = 0$ , (f)  $\tilde{B} = 4$ , (g)  $\tilde{B} = 16$  and (h)  $\phi = \frac{1}{4}$ . Similarly, in the weak magnetic field region of  $\tilde{B} = 2$ , Landau levels are not perfectly formed and the band structure at  $\phi = 0$  does not change. For  $\tilde{B} = 16$ , where the ribbon width is sufficiently wide compared with the cyclotron radius, the Landau levels are again almost formed as shown in Fig. 2.12. For the case of  $q \ll N$  and high-commensurate fluxes, we show the energy band structure of  $\phi = \frac{1}{4}$  in Fig. 2.12 (d). We also find that despite the additional dispersion between Landau subbands, no partly flat

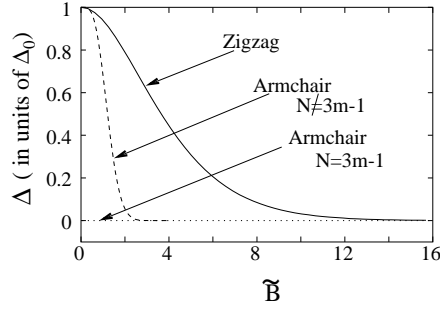


Figure 2.15: Magnetic field dependence of the energy gap of armchair (zigzag) ribbons at  $k = 0$  ( $k = 2\pi/3$ ). The energy gaps are normalized by the energy gap,  $\Delta_0$ , of  $\tilde{B} = 0$ .

bands, as may occur in zigzag ribbons, are present at  $E = 0$  even in a magnetic field.

Next we show that the band dispersions near  $E = 0$  can be scaled by the ribbon width  $W$  for sufficiently wide ribbons. In Fig.2.13, the scaled band structures are shown, when (a)  $\tilde{B} = 0$ , (b)  $\tilde{B} = 4$  and (c)  $\tilde{B} = 16$ . Here the energy and the wave number  $k'$  is scaled by  $W$ , and  $k'$  means the wave number measured from  $k = 2\pi/3$ . In the figures, the bold lines are dispersions of zigzag ribbons, and the dotted lines are the corresponding Landau levels of graphene sheet for comparison. Similarly, the band dispersions of the armchair ribbons can be scaled. In Fig.2.14, the scaled band structures are shown, when (a)  $\tilde{B} = 0$ , (b)  $\tilde{B} = 4$  and (c)  $\tilde{B} = 16$ . Bold lines are metallic armchair ribbons ( $N = 3m - 1$ ) and dashed lines are semiconducting armchair ribbons ( $N \neq 3m - 1$ ). The dotted lines are the corresponding Landau levels of graphene sheet for comparison.

In Fig.2.15(a), it is shown the magnetic field dependence of the energy gap for armchair and zigzag ribbons. The energy gap of semiconducting armchair ribbons becomes negligible when the effective magnetic field  $\tilde{B}$  is much larger than 2. This condition is same as the case of usual quantum wire. However, we need more strong magnetic field to collapse the energy gap (at  $k = 2\pi/3$ ) of zigzag ribbons. This is due to the bonding and anti-bonding configuration of two edge states. In the zero-field limit,  $(1 - \Delta/\Delta_0)$  depends on  $\tilde{B}^4$  for armchair ribbons, and  $\tilde{B}^2$  for zigzag ribbons.

### 2.5.1 Edge states in a magnetic field

In the case of finite magnetic field, using Eqs.(2.23) and (2.24) under the condition of  $\epsilon = 0$ , we can derive the wave function on the  $n^{\text{th}}$  zigzag line as

$$\Psi_n = \prod_{i=1}^n D_k(i), \quad (2.51)$$

where

$$D_k(i) = \begin{cases} -2 \cos\left(\frac{k}{2} - \frac{N-2i+1}{2}\pi\phi\right) & (i \geq 2) \\ 1 & (i = 1) \end{cases} \quad (2.52)$$

For the rational flux  $\phi = \frac{p}{q}$ , there is a relation of  $D_k(i+q) = D_k(i)$ , so that in the case of semi-infinite graphite Eq.(2.51) might be rewritten as

$$\Psi_{nq} = (\Delta_k)^{n-1}, \quad (2.53)$$

where

$$\Delta_k = \prod_{i=1}^q D_k(i) \quad (2.54)$$

Thus, the edge states are modified in the presence of a magnetic field. The condition of the convergence of wave function becomes  $\Delta_k \leq 1$ , which then defines the region of the flat band. Note that  $\Delta_k$  has  $q$  internal degrees of freedom. In other words, there are  $q$  solutions which give the same value of  $\Delta_k$ . For example, in the case of  $\phi = \frac{1}{4}$ , there are 4 wave numbers which give  $\Delta_k = 0$ , i.e,  $k = \pm\frac{3}{4}\pi, \pm\frac{1}{4}\pi$ , the charge density corresponding to each wave number is depicted in Fig. 2.16. The charge density does not penetrate to the inner sites farther than up to the  $(4+1)$ -th zigzag chain, and there are 4 kinds of localized modes corresponding to the 4 internal degrees of freedom of  $\Delta_k$ . Thus, the edge states in a magnetic field behave as the zero-field edge states with  $q$  internal degrees of freedom.

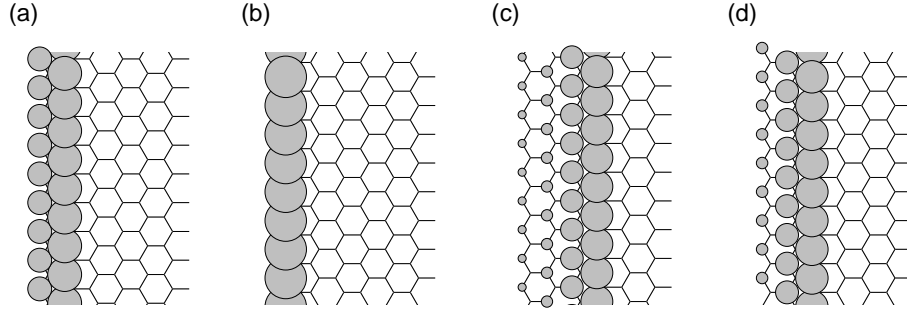


Figure 2.16: The charge density of the edge state at (a)  $k = -\frac{3}{4}\pi$ , (b)  $k = -\frac{1}{4}\pi$ , (c)  $k = \frac{1}{4}\pi$  and (d)  $k = \frac{3}{4}\pi$ , where the radius of the circle denotes the magnitude of the charge density.

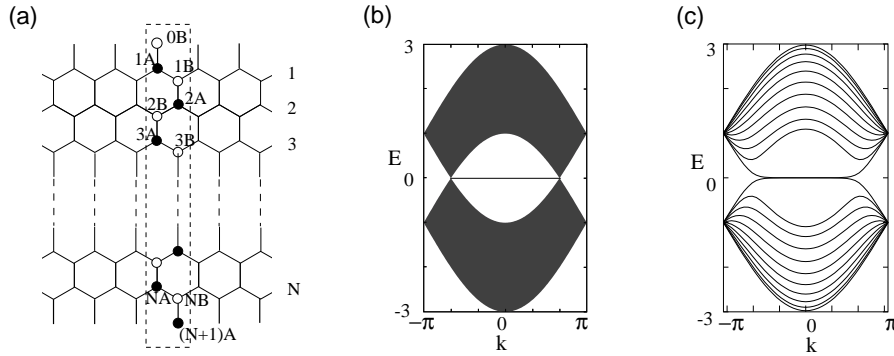


Figure 2.17: (a) The structure of bearded ribbon II. (b) The band structure of a semi-infinite graphene sheet with a bearded edge. (c) The band structure of bearded ribbon for  $N = 10$ .

## 2.6 Bearded Edge and Cove Edge

In this section, we discuss two other important edge shapes having translational symmetry of zigzag axis, called *bearded* and *cove*. Although these two edges look more artificial than the zigzag edge, they are interesting because they also show the non-bonding edge localized. The analytic representation and their band structures are briefly presented here.

### Bearded edge

A Bearded edge is a zigzag edge attached additional  $\sigma$ -bonds. We assume that these  $\sigma$ -bonds are terminated by hydrogen atoms and the onsite energy of these sites is set at zero. The graphene ribbons with two bearded edges as shown in Fig.2.17(a) was firstly studied by Klein, and he also presented an analytic form of the edge states. In Fig.2.17(b), the band structure of a semi-infinite graphene sheet with a bearded edge is shown. Interestingly, a partly flat band appears in the region of  $|k| \leq \frac{2\pi}{3}$ , which is the opposite condition in the semi-infinite graphene sheet with a zigzag edge. The analytic form of this edge state can be derived in the similar ways described in the Chapters 1 and 2 for the derivation of the edge state of zigzag edges. If we consider the case of  $N$  is infinite in the Fig.2.17(a), the analytic solution can be written as,

$$\Psi_{nB} = (1/D_k)^n \quad \text{and} \quad \Psi_{nA} = 0, \quad (2.55)$$

where  $D_k = -2 \cos(k/2)$ . The convergence condition of the wave function,  $1/D_k \leq 1$ , gives the region of the edge state as  $|k| \leq \frac{2\pi}{3}$ . Since the penetration depth of the edge states get longer toward  $k = \pm \frac{2}{3}\pi$ , the small energy gaps appear near  $k = \pm \frac{2}{3}\pi$  in the case of finite width ribbons due to the development of the bonding and anti-bonding configuration between two edge states.

Next we show the ribbons having zigzag and bearded edge as shown in Fig.2.18(a). Since in this ribbon  $|N_A - N_B| = 1$ , where  $N_A$  ( $N_B$ ) means the number of sites belonging to the A(B)-sublattice, there is a flat band at  $E = 0$  all over the 1st BZ, as shown in Fig.2.18(b). The analytic solution of this flat band can be easily understood by the combination of two edge states for zigzag and bearded edges. In the region of  $|k| < \frac{2}{3}\pi$ , the

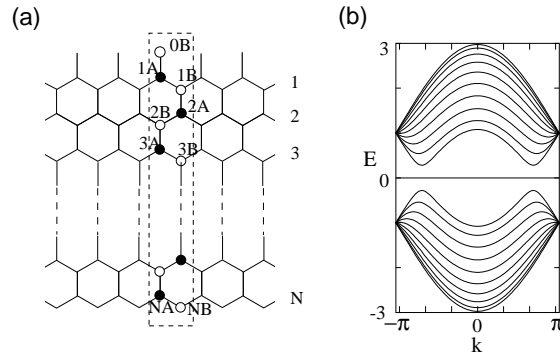


Figure 2.18: (a) The structure of bearded ribbon I. (b) The band structure of a semi-infinite graphene sheet with a bearded edge. (c) The band structure of bearded ribbon for  $N = 10$ .

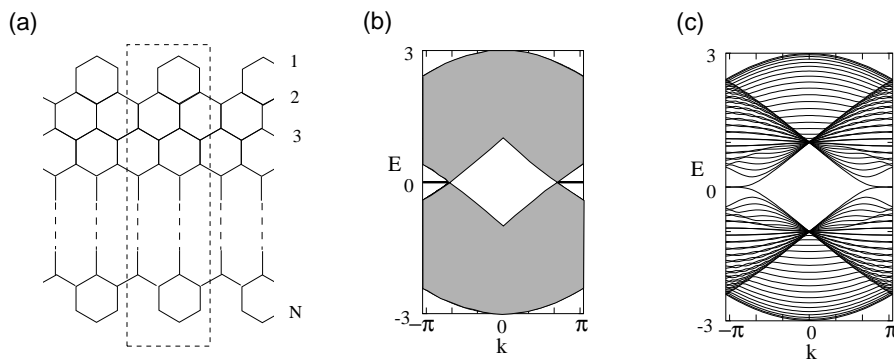


Figure 2.19: (a) The structure of cove ribbon. (b) The band structure of a semi-infinite graphene sheet with a cove edge. (c) The band structure of bearded ribbon for  $N = 10$ .

electrons localized at the bearded edge, and in the region of  $|k| > \frac{2}{3}\pi$ , the electrons localized at the zigzag edge. At  $k = \pm \frac{2}{3}\pi$ , the electrons are delocalized. It should be noted that this ribbon is insulating because the flat band does not carry currents and there are energy gaps between the flat band and next subbands. We will use this ribbon in the Chapter 4 for the study on the electronic transport properties.

### Cove edge

Cove edge is a zigzag edge attached additional hexagon rings. The graphene ribbons with two cove edges as shown in Fig.2.19(a). In Fig.2.19(b), the band structure of a semi-infinite graphene sheet with a cove edge is shown. This case also provides a partly flat band in the region of  $|k| \leq \frac{2}{3}\pi$ . The analytic solution is not simple such as the cases of zigzag and bearded edges, because the unit cell is the double size of other two ribbons.

The important conclusion in this section is that an edge which are not parallel to an armchair axis provides edge states. Actually, graphene ribbons with mixed armchair edges and zigzag edges also show the localized states [39]. Thus it is considered that the edges whose cutting direction not parallel to the armchair axis show edge localized states. Here we do not consider the effect of odd-membered rings such as pentagon and heptagon, because they will make the problems more complicated. The reason why an armchair edge does not provide an edge state will be clarified in the connection with a surface bound state of anisotropic superconductivity in the last section of this chapter.

## 2.7 $\mathbf{k} \cdot \mathbf{p}$ Theory

In this section, we consider how an edge state can be described in the framework of the continuum model such as  $\mathbf{k} \cdot \mathbf{p}$  approximation. We will find that the appearance of the zero-energy state can be easily confirmed. However the conditions for the special shapes of edges are not subtle.

### 2.7.1 Solutions with the translational symmetry of zigzag axis

Let us consider the generic solutions having the translational invariance to x-axis (zigzag axis, see Fig.2.3), starting from the  $\mathbf{k} \cdot \mathbf{p}$  equation near the K-point. We take the plane wave form to x-axis written as

$$F_i^{\mathbf{K}}(\mathbf{r}) \propto e^{ik \cdot x} F_i^{\mathbf{K}}(y), \quad (i = A, B) \quad (2.56)$$

then the  $\mathbf{k} \cdot \mathbf{p}$  equation is rewritten as

$$\begin{pmatrix} -\epsilon & k - \partial_y \\ k + \partial_y & -\epsilon \end{pmatrix} \begin{pmatrix} F_A^{\mathbf{K}}(y) \\ F_B^{\mathbf{K}}(y) \end{pmatrix} = 0. \quad (2.57)$$

This simultaneous differential equation has two pairs of solutions.

**Solution 1**

$$-\epsilon F_A^{\mathbf{K}}(y) + (k - \partial_y) F_B^{\mathbf{K}}(y) = 0 \quad (2.58)$$

$$(k + \partial_y) F_A^{\mathbf{K}}(y) - \epsilon F_B^{\mathbf{K}}(y) = 0 \quad (2.59)$$

Eliminating  $F_A^{\mathbf{K}}(y)$  by substituting the first equation to the second equation, we can obtain the following differential equation,

$$\partial_y^2 F_B^{\mathbf{K}}(y) + (\epsilon^2 - k^2) F_B^{\mathbf{K}}(y) = 0. \quad (2.60)$$

Since this equation has two independent solutions,

$$e^{\sqrt{\epsilon^2 - k^2}y} \quad \text{and} \quad e^{-\sqrt{\epsilon^2 - k^2}y}, \quad (2.61)$$

$F_B^{\mathbf{K}}(y)$  is written as

$$F_B^{\mathbf{K}}(y) = C_1 e^{\sqrt{\epsilon^2 - k^2}y} + C_2 e^{-\sqrt{\epsilon^2 - k^2}y}. \quad (2.62)$$

From the Eq.(2.58),  $F_A^{\mathbf{K}}(y)$  is written as

$$\epsilon F_A^{\mathbf{K}}(y) = C_1 (k - \sqrt{k^2 - \epsilon^2}) e^{\sqrt{\epsilon^2 - k^2}y} + C_2 (k + \sqrt{k^2 - \epsilon^2}) e^{-\sqrt{\epsilon^2 - k^2}y}. \quad (2.63)$$

As a result, we obtain the following pair of solutions,

$$\begin{pmatrix} F_A^{\mathbf{K}}(y) \\ F_B^{\mathbf{K}}(y) \end{pmatrix} = \begin{pmatrix} C_1 (k - \sqrt{k^2 - \epsilon^2}) e^{\sqrt{\epsilon^2 - k^2}y} + C_2 (k + \sqrt{k^2 - \epsilon^2}) e^{-\sqrt{\epsilon^2 - k^2}y} \\ C_1 \epsilon e^{\sqrt{\epsilon^2 - k^2}y} + C_2 \epsilon e^{-\sqrt{\epsilon^2 - k^2}y} \end{pmatrix}. \quad (2.64)$$

Now let us inspect this solution in the case of  $\epsilon = 0$ . For  $k > 0$ , the solution can be written as

$$\begin{pmatrix} F_A^{\mathbf{K}}(y) \\ F_B^{\mathbf{K}}(y) \end{pmatrix} = \begin{pmatrix} C_2 2k e^{-ky} \\ 0 \end{pmatrix}, \quad (2.65)$$

This envelope functions show that the wavefunction is zero on the B-sites and the amplitude on A-sites monotonically decreases, with increasing  $y$ . Therefore, this solution represents the wave function of (i) zigzag edge for  $y > 0$  and (ii) bearded edge for  $y < 0$ . Next, For  $k < 0$

$$\begin{pmatrix} F_A^{\mathbf{K}}(y) \\ F_B^{\mathbf{K}}(y) \end{pmatrix} = \begin{pmatrix} -C_1 2|k| e^{|k|y} \\ 0 \end{pmatrix} \quad (2.66)$$

This couple of envelope function indicates that B-sites are nodes the amplitude on A-sites monotonically increase, decreasing  $y$ . Therefore, this solution becomes the wave function of (i) bearded edge where  $y > 0$  and (ii) zigzag edge  $y < 0$ .

**Solution 2**

The second pair of solutions can be derived by the following differential equation obtained by eliminating  $F_B^{\mathbf{K}}(y)$ ,

$$\partial_y^2 F_A^{\mathbf{K}}(y) + (\epsilon^2 - k^2) F_A^{\mathbf{K}}(y) = 0. \quad (2.67)$$

After the similar manipulation, the envelope functions are written as

$$\begin{pmatrix} F_A^{\mathbf{K}}(y) \\ F_B^{\mathbf{K}}(y) \end{pmatrix} \propto \begin{pmatrix} C_1 \epsilon e^{\sqrt{\epsilon^2 - k^2}y} + C_2 \epsilon e^{-\sqrt{\epsilon^2 - k^2}y} \\ C_1 (k - \sqrt{k^2 - \epsilon^2}) e^{\sqrt{\epsilon^2 - k^2}y} + C_2 (k + \sqrt{k^2 - \epsilon^2}) e^{-\sqrt{\epsilon^2 - k^2}y} \end{pmatrix}. \quad (2.68)$$

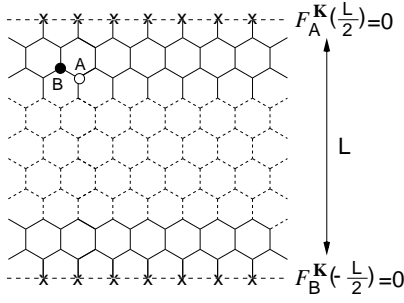


Figure 2.20: The structure of the zigzag ribbon. The boundary conditions for the envelope functions are  $F_A^K(\frac{L}{2}) = 0$  and  $F_B^K(-\frac{L}{2}) = 0$ .

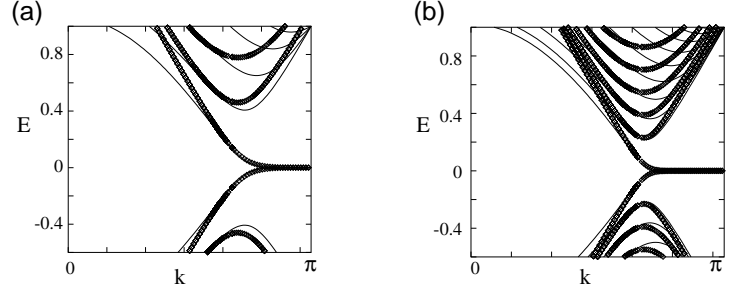


Figure 2.21: The comparison of the energy band structures. The bold (diamond) lines represent the band structures based on the tight binding model (k-p model) for the zigzag ribbon of (a)  $N = 10$  and (b)  $N = 20$ .

When  $\epsilon = 0$  and  $k > 0$ ,

$$\begin{pmatrix} F_A^K(y) \\ F_B^K(y) \end{pmatrix} = \begin{pmatrix} 0 \\ C_2 2k e^{ky} \end{pmatrix}, \quad (2.69)$$

This indicates that A-sites are nodes and the amplitude on B-sites monotonically increase, decreasing  $y$ . Therefore, this solution becomes the wave function of (i) bearded edge for  $y > 0$  and (ii) zigzag edge for  $y < 0$ . For  $\epsilon = 0$  and  $k < 0$ ,

$$\begin{pmatrix} F_A^K(y) \\ F_B^K(y) \end{pmatrix} = \begin{pmatrix} 0 \\ -C_1 2|k| e^{-|k|y} \end{pmatrix} \quad (2.70)$$

This pair of envelope functions indicates that A-sites are nodes the amplitude on B-sites monotonically decrease, increasing  $y$ . Therefore, this solution becomes the wave function of (i) zigzag edge for  $y > 0$  and (ii) bearded edge for  $y < 0$ .

## 2.7.2 Envelope functions on graphite ribbons

### Zigzag ribbons

Let us construct the envelop functions on zigzag ribbons with arbitrary width  $L$ . The origin of y-axis is taken at the center of zigzag ribbons, so that the region of zigzag ribbons is  $-\frac{L}{2} \leq y \leq \frac{L}{2}$ . The two-coordinated sites at  $y = \frac{L}{2}(-\frac{L}{2})$  are B(A)-sublattice. When  $k > 0$ , we have already seen that zigzag boundary provides an edge state in the gap region of  $|\epsilon| < |k|$ .  $F_B^K$  ( $F_A^K$ ) has a maximum value at  $y = \frac{L}{2}(-\frac{L}{2})$  and decreases toward inner sites when the wave number  $k$  is positive. Therefore, the candidate of a pair of the envelop functions ( $k > 0$ ) which satisfy above conditions is

$$\begin{pmatrix} F_A^{K,>}(y) \\ F_B^{K,>}(y) \end{pmatrix} = C_1 \begin{pmatrix} \epsilon \\ k + \sqrt{k^2 - \epsilon^2} \end{pmatrix} e^{\sqrt{\epsilon^2 - k^2}(y - \frac{L}{2})} + C_2 \begin{pmatrix} k + \sqrt{k^2 - \epsilon^2} \\ \epsilon \end{pmatrix} e^{-\sqrt{\epsilon^2 - k^2}(y + \frac{L}{2})}. \quad (2.71)$$

Actually, when  $|\epsilon| < |k|$ , the 1st term decays from  $y = \frac{L}{2}$  toward inner sites and the 2nd term decays from  $y = -\frac{L}{2}$  toward inner sites. When  $|\epsilon| > |k|$ , these two terms form standing waves. We should take  $C_1 = C_2$  for negative energy (bonding states) and  $C_1 = -C_2$  for positive energy (anti-bonding states).

When  $k$  is negative, the conditions on envelope functions will be changed. In  $k < 0$  region, zigzag ribbons can not have the edge localized states. When  $|\epsilon| < |k|$ ,  $F_B^K$  ( $F_A^K$ ) has minimum value at  $y = \frac{L}{2}(-\frac{L}{2})$  and increases toward inner sites when the wave number  $k$  is negative. Thus, we can construct the envelope function as follows,

$$\begin{pmatrix} F_A^{K,<}(y) \\ F_B^{K,<}(y) \end{pmatrix} = C_1 \begin{pmatrix} \epsilon \\ k - \sqrt{k^2 - \epsilon^2} \end{pmatrix} e^{-\sqrt{\epsilon^2 - k^2}(y - \frac{L}{2})} + C_2 \begin{pmatrix} k - \sqrt{k^2 - \epsilon^2} \\ \epsilon \end{pmatrix} e^{\sqrt{\epsilon^2 - k^2}(y + \frac{L}{2})}. \quad (2.72)$$

Afterwards, we have to impose the following boundary conditions on the above envelope functions in order to derive the relation between energy and wave number,

$$F_A^K \left( y = \frac{L}{2} \right) = F_B^K \left( y = -\frac{L}{2} \right) = 0. \quad (2.73)$$

Localized states ( $|\epsilon| < |k|$ )

When we impose  $C_1 \neq 0$  and  $C_2 \neq 0$ , for  $k > 0$ , the boundary condition provide the following determinant,

$$\det \begin{pmatrix} \epsilon & (k + \eta)e^{-\eta L} \\ (k + \eta)e^{-\eta L} & \epsilon \end{pmatrix} = 0, \quad (2.74)$$

where  $\eta = \sqrt{k^2 - \epsilon^2}$ . Therefore,

$$\epsilon = \pm(k + \eta)e^{-\eta L} \quad (2.75)$$

This equation has solution as  $\epsilon = k$ , however, in this case the original differential equation has double solutions. We exclude this solution here. Otherwise, we should note that this equation has one solution in the gap, i.e.,  $|\epsilon| < |k|$ . This solution is a localized state.

For negative  $k$ , the relation between  $k$  and  $\epsilon$  becomes

$$\epsilon = \pm(k - \eta)e^{\eta L}. \quad (2.76)$$

It is clear that the solution of this equation is only  $\epsilon = k$ . Therefore there is no edge state when  $k < 0$ .

Extended states ( $|\epsilon| > |k|$ )

Now we consider the solutions of the extended states, i.e.  $|\epsilon| > |k|$ . Similarly, the relation between  $\epsilon$  and  $k$  is

$$\epsilon = \pm(k + i\tilde{k})e^{-i\tilde{k}L} = |\epsilon|e^{i\theta} \quad (2.77)$$

$$= k \cos(\tilde{k}L) + \tilde{k} \sin(\tilde{k}L) + i \left\{ \tilde{k} \cos(\tilde{k}L) - k \sin(\tilde{k}L) \right\} = \xi + i\nu \quad (2.78)$$

where  $\tilde{k} = \sqrt{\epsilon^2 - k^2}$ . Therefore, we obtain two equations

$$\xi - \epsilon = 0 \quad \text{and} \quad \nu = 0. \quad (2.79)$$

From  $\nu = 0$ , the condition of the extended states is given by

$$\tan(\tilde{k}L) = \frac{\tilde{k}}{k} = \frac{\tilde{k}L}{kL}. \quad (2.80)$$

This equation can be solved graphically or numerically.

For negative  $k$ , the relation between  $k$  and  $\epsilon$  becomes

$$\epsilon = \pm(k - i\tilde{k})e^{i\tilde{k}L} = |\epsilon|e^{i\theta} \quad (2.81)$$

$$= k \cos(\tilde{k}L) + \tilde{k} \sin(\tilde{k}L) + i \left\{ -\tilde{k} \cos(\tilde{k}L) + k \sin(\tilde{k}L) \right\} = \xi + i\nu \quad (2.82)$$

From  $\nu = 0$ , the condition of the extended states is given by

$$\tan(\tilde{k}L) = \frac{\tilde{k}}{k} = -\frac{\tilde{k}L}{|k|L}. \quad (2.83)$$

In Fig.2.21, we show the energy band structure obtained from  $\mathbf{k} \cdot \mathbf{p}$  approximation (diamond), together with the energy bands from the tight binding model(bold line). The  $\mathbf{k} \cdot \mathbf{p}$  approximation excellently reproduce the low-energy feature of the energy dispersion.

**Envelope functions on bearded ribbons II**

Let us consider the envelope functions on bearded ribbons II with arbitrary width  $L$  (graphene ribbon whose both edges are bearded edge, see Fig2.17(a)).

For positive  $k$  with  $\epsilon \leq k$ , the bearded boundary ( $y = \pm \frac{L}{2}$ ) provides diverging solutions toward inner sites. Therefore, the pair of the envelop functions ( $k > 0$ ) which satisfy above boundary condition is

$$\begin{pmatrix} F_{\mathbf{A}}^{\mathbf{K},>}(y) \\ F_{\mathbf{B}}^{\mathbf{K},>}(y) \end{pmatrix} = C_1 \begin{pmatrix} \epsilon \\ k + \sqrt{k^2 - \epsilon^2} \end{pmatrix} e^{\sqrt{\epsilon^2 - k^2}(y + \frac{L}{2})} + C_2 \begin{pmatrix} k + \sqrt{k^2 - \epsilon^2} \\ \epsilon \end{pmatrix} e^{-\sqrt{\epsilon^2 - k^2}(y - \frac{L}{2})}. \quad (2.84)$$

On the other hand, for negative  $k$  with  $\epsilon \leq k$ , the bearded boundary ( $y = \pm \frac{L}{2}$ ) provides edge localized solutions damping toward inner sites, where the sites on B-sublattice are node. The pair of the envelop functions ( $k < 0$ ) which satisfy above boundary condition is

$$\begin{pmatrix} F_{\mathbf{A}}^{\mathbf{K},<}(y) \\ F_{\mathbf{B}}^{\mathbf{K},<}(y) \end{pmatrix} = C_1 \begin{pmatrix} k - \sqrt{k^2 - \epsilon^2} \\ \epsilon \end{pmatrix} e^{\sqrt{\epsilon^2 - k^2}(y + \frac{L}{2})} + C_2 \begin{pmatrix} \epsilon \\ k - \sqrt{k^2 - \epsilon^2} \end{pmatrix} e^{\sqrt{\epsilon^2 - k^2}(y - \frac{L}{2})}. \quad (2.85)$$

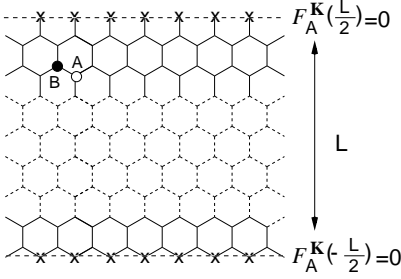


Figure 2.22: The structure of the bearded ribbon (Type I). The boundary conditions for the envelope functions are  $F_A^K(\frac{L}{2}) = 0$  and  $F_A^K(-\frac{L}{2}) = 0$ .

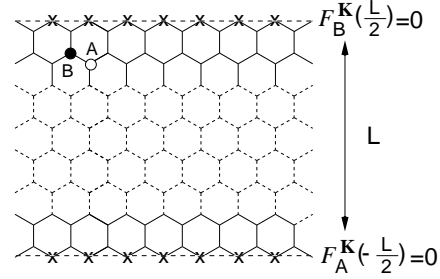


Figure 2.23: The structure of the bearded ribbon (Type II). The boundary conditions for the envelope functions are  $F_B^K(\frac{L}{2}) = 0$  and  $F_A^K(-\frac{L}{2}) = 0$ .

These pairs of envelope functions must satisfy the following boundary conditions:

$$F_B^K\left(y = \frac{L}{2}\right) = F_A^K\left(y = -\frac{L}{2}\right) = 0. \quad (2.86)$$

Localized states ( $|\epsilon| < |k|$ )

When  $C_1 \neq 0$  and  $C_2 \neq 0$  for  $k < 0$ , the above boundary conditions provide the following determinant,

$$\det \begin{pmatrix} k - \eta & \epsilon e^{\eta L} \\ \epsilon e^{\eta L} & k - \eta \end{pmatrix} = 0, \quad (2.87)$$

where  $\eta = \sqrt{k^2 - \epsilon^2}$ . Therefore,

$$\epsilon = \pm(k - \eta)e^{-\eta L} \quad (2.88)$$

This equation has solution when  $\epsilon = k$ , however, in this case the original differential equation has double solutions. We exclude this solution here. Otherwise, we should note that this equation has one solution when  $0 < \epsilon < -|k|$  and  $|k| < \epsilon < 0$ . This latter solution is the localized states at the bearded boundary.

For positive  $k$ , the relation between  $k$  and  $\epsilon$  is

$$\epsilon = \pm(k + \eta)e^{\eta L}. \quad (2.89)$$

It is clear that the solution of this equation is only  $\epsilon = k$ . Therefore there is no localized states when  $k > 0$ .

Extended states ( $|\epsilon| > |k|$ )

For negative  $k$  of  $|\epsilon| > |k|$ , the relation between  $\epsilon$  and  $k$  is

$$\epsilon = \pm(-|k| - i\tilde{k})e^{-i\tilde{k}L}, \quad (2.90)$$

where  $\tilde{k} = \sqrt{\epsilon^2 - k^2}$ . For positive  $k$ , the relation between  $\epsilon$  and  $k$  is

$$\epsilon = \pm(k - i\tilde{k})e^{i\tilde{k}L}, \quad (2.91)$$

where  $\tilde{k} = \sqrt{\epsilon^2 - k^2}$ . These two equations give the energy dispersion of extended states.

### Envelope functions on bearded ribbons I

Now we consider the envelop functions of bearded ribbons of type I with arbitrary width  $L$  (see Fig.2.18(a)). The origin of  $y$ -axis is taken at the center of ribbons, so that the region of ribbons is  $-\frac{L}{2} \leq y \leq \frac{L}{2}$ .

For positive  $k$ , the zigzag boundary ( $y = \frac{L}{2}$ ) provides the localized states damping toward inner sites, and the sites on A-sublattice are nodal site. However, the bearded boundary ( $y = -\frac{L}{2}$ ) provides the wave function diverging toward inner sites. Therefore, the ansatz for the pair of the envelop functions ( $k > 0$ ) which satisfy above boundary condition is

$$\begin{pmatrix} F_A^{K,>}(y) \\ F_B^{K,>}(y) \end{pmatrix} = C_1 \begin{pmatrix} \epsilon \\ k + \sqrt{k^2 - \epsilon^2} \end{pmatrix} e^{\sqrt{\epsilon^2 - k^2}(y - \frac{L}{2})} + C_2 \begin{pmatrix} \epsilon \\ k + \sqrt{k^2 - \epsilon^2} \end{pmatrix} e^{\sqrt{\epsilon^2 - k^2}(y + \frac{L}{2})}. \quad (2.92)$$

In the condition of  $|\epsilon| < |k|$ , the 1st term represents the damping wave from  $y = \frac{L}{2}$  toward inner sites, the 2nd term represents the diverging wave from  $y = -\frac{L}{2}$  toward inner sites. The boundary conditions for the bearded ribbon-I are

$$F_A^K \left( y = \frac{L}{2} \right) = F_A^K \left( y = -\frac{L}{2} \right) = 0, \quad (2.93)$$

so that we find

$$\epsilon (1 \pm e^{\eta L}) = 0. \quad (2.94)$$

The solution of this equation is  $\epsilon = k$  or  $\epsilon = 0$ . The former solution is ignored. The latter one means the existence of a flat band.

For the negative  $k$ , the bearded boundary ( $y = -\frac{L}{2}$ ) provides the localized states damping toward inner sites localized at B sublattice when  $k$  is negative. However, the zigzag boundary ( $y = \frac{L}{2}$ ) provides the wave function diverging toward inner sites. The pair of a couple of the envelop functions ( $k < 0$ ) which satisfy above boundary condition is

$$\begin{pmatrix} F_A^{K,<}(y) \\ F_B^{K,<}(y) \end{pmatrix} = C_1 \begin{pmatrix} \epsilon \\ k + \sqrt{k^2 - \epsilon^2} \end{pmatrix} e^{\sqrt{\epsilon^2 - k^2}(y - \frac{L}{2})} + C_2 \begin{pmatrix} \epsilon \\ k + \sqrt{k^2 - \epsilon^2} \end{pmatrix} e^{\sqrt{\epsilon^2 - k^2}(y + \frac{L}{2})}. \quad (2.95)$$

By imposing the boundary conditions, we again obtain same equation,

$$\epsilon (1 \pm e^{\eta L}) = 0. \quad (2.96)$$

## 2.8 Connection with Anisotropic Superconductivity

After the discovery of the high temperature superconductor (HTSC), considerable effort of the studies on the mechanism causing superconductivity has been devoted. Today, a great deal of experimental data gives the convincing evidence that the pair wavefunction has  $d_{x^2-y^2}$ -wave symmetry rather than  $s$ -wave symmetry. This unconventional pairing symmetry induces much interest physical properties, one of them is the Andreev bound states at [110]-surface of  $d_{x^2-y^2}$ -wave superconductor, which is observed as a zero-bias conductance peak in the current-voltage characteristics [98–100]. In this section, we show that the mechanism of the surface bound states at [110]-surface of  $d_{x^2-y^2}$ -wave superconductor is closely related to the edge states of graphite edges. The reason why the armchair edge does not have the edge states is clarified.

### 2.8.1 Bound states at [110]-surface of $d_{x^2-y^2}$ -wave superconductor

Before we show the mechanism of the surface bound states of [110]-surface of  $d_{x^2-y^2}$ -wave SC, we shall briefly study some characteristics of  $d_{x^2-y^2}$ -wave pairing symmetry. Let us consider how the electron (or hole) behaves at the surface of  $d_{x^2-y^2}$ -wave SC. In Fig.2.24(a), the classical trajectories of electrons and holes in the region of the [100]-surface are shown. The change of the momentum of these trajectories by the reflection at the surface always connect same signs of the pairing potential. However, at the [110]-surface, as shown in Fig.2.24(b), the change of the momentum of these trajectories by the reflection at the surface always connect different signs of the pairing potential, and lead to a phase shift  $\pi$ . This  $\pi$ -phase shift is the origin of the Andreev bound states at [110]-surface of  $d_{x^2-y^2}$ -wave SC as we will see in the following.

Following Hu [98], we shall study the origin of the Andreev bound states at [110]-surface of  $d$ -wave superconductor, and we will see how the  $\pi$ -phase shift yields the zero-energy bound states. The elementary excitation of an inhomogeneous superconductor obey the Bogoliubov-de Gennes (BdG) equations [101]:

$$\epsilon_n u_n(\mathbf{x}_1) = \hat{h}_0 u_n(\mathbf{x}_1) + \int \Delta(\mathbf{s}, \mathbf{r}) v_n(\mathbf{x}_2) d\mathbf{x}_2, \quad (2.97)$$

$$\epsilon_n v_n(\mathbf{x}_1) = -\hat{h}_0 v_n(\mathbf{x}_1) + \int \Delta(\mathbf{s}, \mathbf{r}) u_n(\mathbf{x}_2) d\mathbf{x}_2, \quad (2.98)$$

where  $\mathbf{s} = (\mathbf{x}_1 - \mathbf{x}_2)/2$ ,  $\mathbf{r} = (\mathbf{x}_1 + \mathbf{x}_2)/2$ , and  $\hat{h}_0 = -\hbar^2 \nabla_{\mathbf{x}_1}^2 / 2m - \mu$ . Here  $\mu$  is the chemical potential. These equations can be simplified for momenta close to the Fermi wavevector  $\mathbf{k}_F$ ,

$$\begin{pmatrix} u_n(\mathbf{r}) \\ v_n(\mathbf{r}) \end{pmatrix} = e^{i\mathbf{k}_F \cdot \mathbf{r}} \begin{pmatrix} \tilde{u}_n(\mathbf{r}) \\ \tilde{v}_n(\mathbf{r}) \end{pmatrix}, \quad (2.99)$$

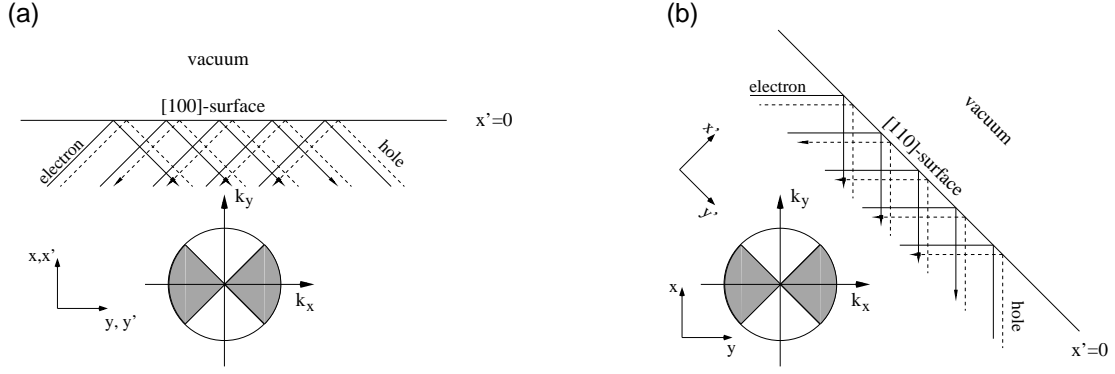


Figure 2.24: Schematic view of Andreev reflection in the surface region of  $d_{x^2-y^2}$ -wave superconductor. The trajectories at the [100]-surface (a) does not connect gap regions of opposite sign, however at the [110]-surface (b) the trajectories connect gap regions of opposite sign which lead to a phase shift  $\pi$  and zero-energy bound states. Shading means the sign of the pair potential.

defining envelope functions  $(\tilde{u}_n(\mathbf{r}), \tilde{v}_n(\mathbf{r}))$ , which obey the following equations, called Andreev equations [102],

$$\epsilon_n u_n(\mathbf{x}_1) = -i \frac{\hbar \mathbf{k}_F}{m} \cdot \nabla \tilde{u}_n(\mathbf{r}) + \Delta(\hat{\mathbf{k}}_F, \mathbf{r}) v_n(\mathbf{r}), \quad (2.100)$$

$$\epsilon_n v_n(\mathbf{x}_1) = i \frac{\hbar \mathbf{k}_F}{m} \cdot \nabla \tilde{v}_n(\mathbf{r}) + \Delta(\hat{\mathbf{k}}_F, \mathbf{r}) u_n(\mathbf{r}). \quad (2.101)$$

This approximation is called ‘‘Andreev approximation’’.

Now let us consider the condition for the Andreev bound states. For simplicity, we take the direction which is perpendicular (parallel) to the surface as  $x'$ -axis ( $y'$ -axis). We consider that the surface has a normal metal overlayer of thickness  $d$ . For  $\Delta(\hat{\mathbf{k}}, \mathbf{r}) = \Delta_0(\hat{\mathbf{k}})\Theta(-x')$ , we can solve these equations similar as in the  $\mathbf{k} \cdot \mathbf{p}$  approximation.

$$(\tilde{u}_n^<, \tilde{v}_n^<) = e^{\gamma x'} (\tilde{u}_n, \tilde{v}_n) \quad \text{for } x' < 0 \quad (2.102)$$

$$(\tilde{u}_n^>, \tilde{v}_n^>) = (e^{-ik_1 x'} \tilde{u}_n, e^{ik_1 x'} \tilde{v}_n) \quad \text{for } x' > 0 \quad (2.103)$$

where

$$\hat{u} = \Delta_0/D, \quad \hat{v} = [-i \cdot \text{sgn}(k_{x0}) \sqrt{\Delta_0^2 - \epsilon_n^2} + \epsilon_n] / D \quad (2.104)$$

with

$$D = \left[ |i \cdot \text{sgn}(k_{x0}) \sqrt{\Delta_0^2 - \epsilon_n^2} - \epsilon_n^2|^2 + \Delta_0^2 \right]^{1/2} \quad (2.105)$$

and

$$\epsilon_n = \sqrt{-(k_{x0} \gamma / m)^2 + \Delta_0^2} = k_{x0} k_1 / m \quad (2.106)$$

Since  $\hat{u}$  and  $\hat{v}$  depend on the sign of  $k_{x0}$  directly as well as indirectly via  $\Delta_0$ , we label them with another subscript + or -. Let us take the superposition of these solutions as follows,

$$\begin{pmatrix} u_n^< \\ v_n^< \end{pmatrix} = e^{\mathbf{k}_\perp \cdot \mathbf{r}_\perp} e^{\gamma x'} \left[ A e^{-ik_{x0} x'} \begin{pmatrix} \hat{u}_{n+} \\ \hat{v}_{n+} \end{pmatrix} + B e^{ik_{x0} x'} \begin{pmatrix} \hat{u}_{n-} \\ \hat{v}_{n-} \end{pmatrix} \right] \quad \text{for } x' < 0, \quad (2.107)$$

$$\begin{pmatrix} u_n^> \\ v_n^> \end{pmatrix} = e^{i\mathbf{k}_\perp \cdot \mathbf{r}_\perp} \left[ A e^{-ik_{x0} x'} \begin{pmatrix} e^{-ik_1 x'} \hat{u}_{n+} \\ e^{ik_1 x'} \hat{v}_{n+} \end{pmatrix} + B e^{ik_{x0} x'} \begin{pmatrix} e^{ik_1 x'} \hat{u}_{n-} \\ e^{-ik_1 x'} \hat{v}_{n-} \end{pmatrix} \right] \quad \text{for } x' > 0, \quad (2.108)$$

where  $\mathbf{k}_\perp = (0, k_y, k_z)$ . The solution must vanish at  $x' = d$ , resulting in we obtain the following condition:

$$e^{4ik_1 d} = \begin{pmatrix} \hat{v}_{n+} \\ \hat{u}_{n+} \end{pmatrix} \begin{pmatrix} \hat{u}_{n-} \\ \hat{v}_{n-} \end{pmatrix} \quad (2.109)$$

For an s-wave superconductor,  $\Delta(-k_{x0}, k_y, k_z) = \Delta(k_{x0}, k_y, k_z)$ , the above equation can be reduced to

$$e^{4ik_1 d} = \frac{\epsilon_n - i \sqrt{\Delta_0^2 - \epsilon_n^2}}{\epsilon_n + i \sqrt{\Delta_0^2 - \epsilon_n^2}}, \quad (2.110)$$

and for  $d_{x^2-y^2}$ -wave superconductor,  $\Delta(-k_x, k_y, k_z) = -\Delta(k_x, k_y, k_z)$ , the above equation can be reduced to

$$e^{4ik_1 d} = -\frac{\epsilon_n - i\sqrt{\Delta_0^2 - \epsilon_n^2}}{\epsilon_n + i\sqrt{\Delta_0^2 - \epsilon_n^2}}. \quad (2.111)$$

We can find that s-wave case have no zero energy solutions, however d-wave case have zero energy solutions. Thus the sign-change of the order-parameter gives zero-energy bound states at the surface.

## 2.8.2 Graphite as an odd-parity superconductor

We start with the tight binding Hamiltonian of a graphene sheet given in the Chapter 1, and derive the BdG-type equation. The tight binding equation of the graphene sheet in the  $\mathbf{k}$ -space is written as

$$\begin{pmatrix} 0 & \epsilon_{\mathbf{k}} \\ \epsilon_{\mathbf{k}} & 0 \end{pmatrix} \begin{pmatrix} \Psi_{A\mathbf{k}} \\ \Psi_{B\mathbf{k}} \end{pmatrix} = \epsilon \begin{pmatrix} \Psi_{A\mathbf{k}} \\ \Psi_{B\mathbf{k}} \end{pmatrix}, \quad (2.112)$$

where

$$\epsilon_{\mathbf{k}} = -t \left[ e^{ik_x a} + e^{-i\left(\frac{k_x a}{2} + \frac{k_y \sqrt{3}a}{2}\right)} + e^{-i\left(\frac{k_x a}{2} - \frac{k_y \sqrt{3}a}{2}\right)} \right]. \quad (2.113)$$

We apply the following transformation to the above Hamiltonian

$$\begin{pmatrix} \Psi_p \\ \Psi_h \end{pmatrix} = \frac{1}{\sqrt{2}} \begin{pmatrix} 1 & 1 \\ -i & i \end{pmatrix} \begin{pmatrix} \Psi_A \\ \Psi_B \end{pmatrix}, \quad (2.114)$$

leading to

$$\begin{pmatrix} \frac{1}{2}(\epsilon_{\mathbf{k}} + \epsilon_{\mathbf{k}}^*) & -\frac{i}{2}(\epsilon_{\mathbf{k}} - \epsilon_{\mathbf{k}}^*) \\ -\frac{i}{2}(\epsilon_{\mathbf{k}} - \epsilon_{\mathbf{k}}^*) & -\frac{1}{2}(\epsilon_{\mathbf{k}} + \epsilon_{\mathbf{k}}^*) \end{pmatrix} \begin{pmatrix} \Psi_{p\mathbf{k}} \\ \Psi_{h\mathbf{k}} \end{pmatrix} = \epsilon \begin{pmatrix} \Psi_{p\mathbf{k}} \\ \Psi_{h\mathbf{k}} \end{pmatrix}. \quad (2.115)$$

In this equation, the diagonal terms formally correspond to the kinetic terms of particle and holes in BdG equation, and the off-diagonal terms can be considered as the pair-potential of the superconductor. In the

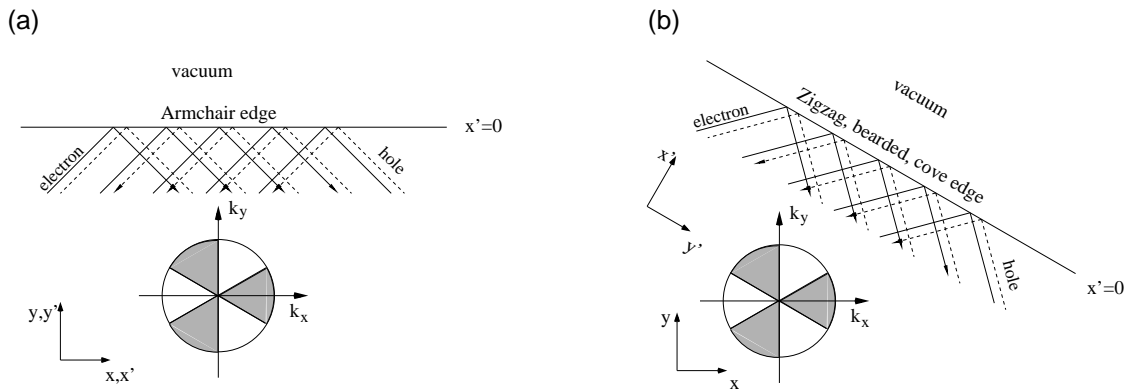


Figure 2.25: Schematic view of Andreev reflection in the surface region of graphite ( $f$ -wave superconductor) surface. The trajectories at the armchair edge (a) does not connect gap regions of opposite sign, however at the zigzag, bearded and cove edge (b) the trajectories connect gap regions of opposite sign which lead to a phase shift  $\pi$  and zero-energy bound states.

continuum limit, we can rewrite the above equation as follows,

$$\begin{pmatrix} -\frac{\hbar^2}{2m}\nabla^2 - \mu & \Delta_{\mathbf{k}} \\ \Delta_{\mathbf{k}} & +\frac{\hbar^2}{2m}\nabla^2 - \mu \end{pmatrix} \begin{pmatrix} \Psi_{p\mathbf{k}} \\ \Psi_{h\mathbf{k}} \end{pmatrix} = \epsilon \begin{pmatrix} \Psi_{p\mathbf{k}} \\ \Psi_{h\mathbf{k}} \end{pmatrix}. \quad (2.116)$$

Here  $\mu$  is the chemical potential and  $\Delta_{\mathbf{k}}$  represents the pair-potential of the superconductor,

$$\Delta_{\mathbf{k}} = -\frac{i}{2}(\epsilon_{\mathbf{k}} - \epsilon_{\mathbf{k}}^*) = \sin(k_x a) + \sin\left[\left(\frac{k_x a}{2} + \frac{k_y \sqrt{3}a}{2}\right)\right] + \sin\left[\left(\frac{k_x a}{2} - \frac{k_y \sqrt{3}a}{2}\right)\right]. \quad (2.117)$$

More simply, this pair potential can be rewritten as

$$\Delta = |\Delta| \cos(3\theta), \quad (2.118)$$

close to the Fermi level, where  $\theta$  is the angle of the Fermi vector measured from  $k_x$ -axis. Interestingly, this pair potential means an odd-parity superconductivity, precisely f-wave superconductivity and deduce the following results: since the armchair (zigzag) axis corresponds to  $k_x$  ( $k_y$ ), the trajectories at the armchair edge does not connect gap regions of opposite sign, however at the zigzag, beaded and cove edge the trajectories connect gap regions of opposite sign which lead to a phase shift  $\pi$  and zero-energy bound states. Thus, the armchair edge does not show the edge localized states.

## 2.9 Summary

In this chapter, we widely discussed the electronic states of nano-graphene ribbons based on the tight binding model and the continuum models in the absence and presence of external magnetic field. The discussion of this chapter, which will be the basis of the chapters 3 and 4, is summarized here.

Edge localized states near zigzag edges are analyzed in terms of the Harper's equation. The approximate form of energy dispersion of the partly flat bands originating from the edge states is obtained:  $E_k = -2tND_k^{N-1} [1 - \cos(\frac{k}{2})]$  for  $\epsilon \ll t\pi/N$ . The corresponding density of states is  $\rho(\epsilon) = \frac{1}{N}\epsilon^\alpha$ , where  $\alpha = 1/N - 1$ .

The energy gap of armchair (zigzag) ribbons at  $k = 0$  ( $k = \frac{2}{3}\pi$ ) is analytically derived. The magnitude of the energy gap is inversely proportional to the ribbon width. In the weak magnetic field region of  $\tilde{B} < 1$ , the energy gap depends on  $B^4$  ( $B^2$ ) for armchair (zigzag) ribbons. The energy gap becomes zero about  $\tilde{B} = 1$  ( $\tilde{B} = 12$ ) for semiconducting armchair (zigzag) ribbons.

Energy band structures of graphene ribbons are numerically analyzed. In magnetic field region of  $\tilde{B} < 4$  ( $\tilde{B} < 16$ ) for armchair (zigzag) ribbons, the energy band dispersion can be scaled by the ribbon width in the low-energy region. It is also confirmed that the partly flat bands originating from the edge states are not be destroyed by the magnetic field. In the presence of magnetic field, generating a rational fraction of the magnetic flux ( $\phi = p/q$ ) in each hexagonal plaquette of the graphite plane, the edge state behaves like a zero-field edge state with  $q$  internal degrees of freedom.

We have adapted the  $\mathbf{k} \cdot \mathbf{p}$  theory to graphene ribbons. The energy dispersion calculated from the tight-binding model is well reproduced by the  $\mathbf{k} \cdot \mathbf{p}$  theory. However, we have to subtly take account of the edge boundary conditions for the  $\mathbf{k} \cdot \mathbf{p}$  Hamiltonian.

We have also discussed the formal analogy between anisotropic superconductor and graphite. In terms of proper unitary transformation, the tight-binding Hamiltonian of a graphene sheet can be mapped to the Bogoliubov-de Gennes equation of an odd-parity (precisely f-wave) superconductor. This pairing potential changes the sign for the zigzag (or bearded, cove) edges, however not for armchair. Therefore, in general, edge states appear at the edges which are not parallel to the armchair edge.



---

# Chapter 3

## Magnetic Properties

---

In this chapter, the magnetic properties of nanographites are discussed in the absence and presence of the electron-electron interactions. It is well known that bulk graphite shows a large anisotropic diamagnetic susceptibility, while aromatic molecules have only weak diamagnetism. This fact tells us that the orbital diamagnetic susceptibility is sensitive to the size of graphite fragments. On the other hand, the sharp peak in the density of states due to the edge states gives rather strong Pauli paramagnetic response, so that the competition between these two components occurs in nanographite systems. Since the edge states also give the possibility of spin polarization at low-temperature due to the electron-electron interaction, we discuss the possibility of the appearance of localized spins at the edges. The results presented are published in Ref. [103].

### 3.1 Orbital Diamagnetism and Pauli Paramagnetism

The observed magnetic susceptibility  $\chi$  is the sum of four components: (1) localized spin susceptibility  $\chi_{spin}$ , (2) diamagnetic susceptibility due to the core electrons  $\chi_{core}$ , (3) Pauli paramagnetic susceptibility  $\chi_P$  and (4) orbital diamagnetic susceptibility  $\chi_{orb}$ , due to the cyclotron motion of the itinerant electrons. Since we neglect electron-electron interaction for the moment,  $\chi_{spin}$  can be neglected. Furthermore,  $\chi_{core}$  is unimportant for us, because it is small and basically temperature independent. On the other hand, the Pauli paramagnetic susceptibility is related to the DOS at the Fermi level, which represents an important component in zigzag nanographite ribbons where an enhanced density of states appears at the Fermi level. Note that  $\chi_P$  is negligible in armchair ribbons, aromatic molecules and graphite sheets, because their DOS is suppressed at the Fermi level. We will see below that since the DOS introduced by the edge states is sharply peaked at the Fermi energy,  $\chi_P$  introduces a very pronounced temperature dependence which is nearly Curie-like. The diamagnetic contribution to the susceptibility is very familiar from the magnetic properties of graphite sheets. It is due to the orbital cyclotron motion of the electrons in a field with a finite component perpendicular to the plane. Naturally, this diamagnetic response is very anisotropic and only weakly temperature dependent. From this we can conclude that in nanographite ribbons with zigzag edges the susceptibility should consist mainly of these two competing contributions,  $\chi_P$  and  $\chi_{orb}$ . Hence, a crossover occurs from a high-temperature diamagnetic to a low-temperature paramagnetic regime, where the characteristic temperature depends on the width of the ribbon and of the orientation of the external field. It is worth noting that the field direction is an important tool to distinguish the magnitude of the two components.

### 3.2 Orbital Magnetization and Susceptibility

In this section, I briefly summarize the calculation method of the orbital diamagnetic susceptibility  $\chi_{orb}$  of graphene ribbons. We use the tight binding model presented in the previous chapter for the calculation of the orbital diamagnetic susceptibility  $\chi_{orb}$ . The free energy  $F(H, T)$  including the magnetic field is given by,

$$F(H, T) = \mu N - \frac{1}{\beta\pi} \int_{BZ} dk \sum_n \ln \left( 1 + e^{-\beta(\epsilon_{k,n}(H) - \mu)} \right) \quad (3.1)$$

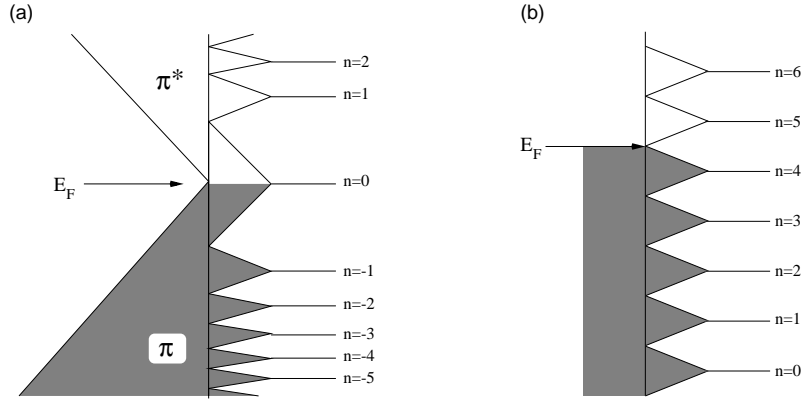


Figure 3.1: (a) Landau levels of graphene sheet near K point (b) Landau levels of 3D metal.

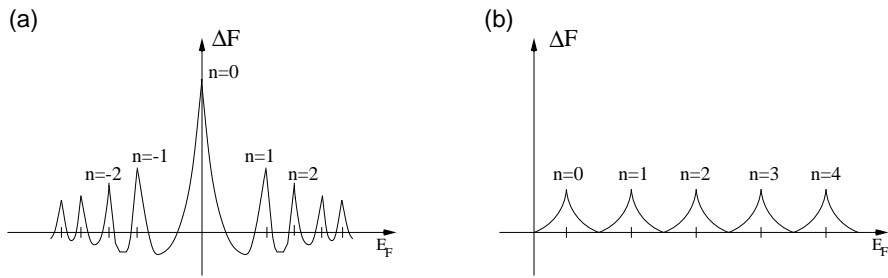


Figure 3.2: (a) Oscillation of free energy of graphene sheet as a function of  $E_F$ . When the Fermi energy is located at zero, this oscillation has the sharp peak, however (b) the simple 3D metal does not show such sharp peaks. The existence of this peak is the origin of large diamagnetism in graphites.

where  $\beta = \frac{1}{k_B T}$  and  $\mu$  is the chemical potential and  $\epsilon_{k,n}(H)$  ( $n$  is the band index) is the energy spectrum of the graphite ribbons in the magnetic field calculated based on the tight binding model. Then the magnetic moment  $M(H)$  and the magnetic susceptibility  $\chi(H)$  per site for finite temperature and arbitrary magnetic field  $H$  become

$$M(H) = -\frac{1}{N_e} \frac{\partial F}{\partial H} = -\frac{1}{N_e \pi} \int dk \sum_n \frac{1}{e^{\beta(\epsilon_{k,n} - \mu)} + 1} \frac{\partial \epsilon_{k,n}}{\partial H}, \quad (3.2)$$

and

$$\chi(H) = \frac{1}{N_e} \frac{\partial M}{\partial H} = -\frac{1}{N_e \pi} \int dk \sum_n \left\{ -\frac{\beta}{4 \cosh^2 \frac{\beta x}{2}} \left( \frac{\partial \epsilon_{k,n}}{\partial H} \right)^2 + \frac{1}{e^{\beta(\epsilon_{k,n} - \mu)} + 1} \frac{\partial^2 \epsilon_{k,n}}{\partial H^2} \right\} \quad (3.3)$$

The zero-field magnetic susceptibility  $\chi_0(T)$  for finite temperature is given by

$$\chi(T) = -\frac{1}{N_e \pi} \left( \frac{S_{\text{hex}}}{\phi_0} \right)^2 \int dk \sum_n^{\text{occ.}} \frac{1}{e^{\beta(\epsilon_{k,n} - \mu)} + 1} \left( \frac{\partial^2 \epsilon_{k,n}}{\partial H^2} \right), \quad (3.4)$$

where  $S_{\text{hex}}$  is the area of a hexagonal ring.  $N_e$  is the electron number in the system.

### 3.2.1 Large orbital diamagnetism of graphene sheet

Before we show the results on the graphene ribbons, let us briefly review the large orbital diamagnetism in graphite. The origin of the large diamagnetism in graphites is due to the appearance of the Landau level at  $E = 0$ . This was first shown by McClure [77]. When the energy dispersion is linear to  $k$  near the K or K' points, the Landau levels  $E_n$  in the 1st BZ of the graphene sheet is expressed as,

$$E_n = \pm \frac{\sqrt{3}}{2} t a \sqrt{2nS} \quad (n = 0, 1, 2, \dots), \quad (3.5)$$

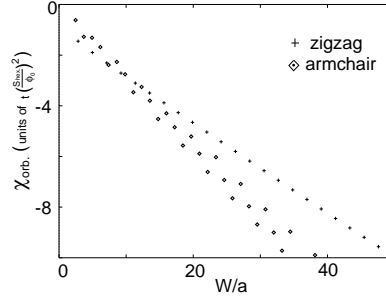


Figure 3.3: The ribbon width dependence of the orbital diamagnetic susceptibility  $\chi_{orb}$  of graphite ribbons at  $T=0$ .

where  $n$  is an index of the Landau levels and  $S$  is given by

$$S = eH/\hbar c. \quad (3.6)$$

Each Landau level has a characteristic feature and is very different from the Landau levels of ordinary 3D free electron gas, as seen in Fig.3.1. It is noted that the zero-th Landau level is always located in the zero gap at the  $\mathbf{K}$  point. The zero-th Landau level does not shift by a magnetic field. We can easily show that all the Landau levels with zero and negative Landau indices which are occupied by the valence electron act to increase the free energy in a magnetic field and thus the orbital diamagnetism appears. When the Fermi energy is located in zero energy gap, the oscillation of the free energy, which is known to cause de Haas-van Alphen effect at low temperatures, has a cusp at  $E_F = 0$  and yields large orbital diamagnetism as shown in Fig.3.2(a). In Fig.3.2(b), we also show the free energy as a function of  $E_F$  in the case of 3D electron gas. As seen in this figure, there are no sharp peaks in the oscillation in contrast to the results in Fig.3.2 (a) for graphene. The expression of orbital susceptibility of graphene sheet at finite temperatures has been derived by McClure [77] based on the  $\mathbf{k} \cdot \mathbf{p}$  approximation is

$$\chi_{MC} = -0.044 \left( \frac{4}{\pi C_L} \right)^{3/2} (ta)^2 \left( \frac{e}{\hbar c} \right)^2 \text{sech}^2 \left( \frac{\mu}{2k_B T} \right) \times (k_B T \rho) \quad [\text{emu/g}], \quad (3.7)$$

where  $\mu$  is the Fermi energy and  $\rho$  is the density of carbon atoms in the unit volume of graphite. The typical value of  $\chi_{MC}$  for the graphite at room temperature is  $21.0 \times 10^{-6}$  emu/g.

### 3.2.2 Orbital diamagnetism of graphene ribbons

The orbital magnetism is influenced by the system geometry and size. The width dependence of the orbital susceptibility  $\chi_{orb}$  at  $T = 0$  is shown in Fig. 3.3. Analogous to the graphene sheets, the aromatic molecules or the carbon nanotubes, the graphite ribbons exhibit diamagnetism. The magnitude of  $\chi_{orb}(T \approx 0)$  grows linearly with increasing  $W$  in accordance with the fact that  $\chi_{orb}$  of the graphene sheet diverges in the zero-temperature limit. A remarkable point is the different slope in the  $W$ -dependence of  $\chi_{orb}$  for armchair and zigzag ribbons. Actually the difference between the susceptibilities of the two types of ribbons increases for larger  $W$ . At a first glance, this result may seem unphysical, because one might attribute the difference to an edge effect which should diminish for wider ribbons. The origin of this discrepancy, however, is based on topological properties as we will show shortly. We would like also to mention the aspect that  $\chi_{orb}$  for the armchair ribbons shows some oscillations as a function of  $W$ . This is due to the fact that armchair ribbons are metallic or insulating depending on  $W$ . On the other hand, no oscillations occur for zigzag ribbons, as they are metallic for all  $W$ .

#### Ring currents behavior driven by a magnetic field

The difference of the slope in  $\chi_{orb}$  and  $M_{orb}$  is related to the more microscopic and configurational aspect of the ribbons. An important point to take into account is the ring current susceptibility in the equilibrium state, because the magnetic moments and ring currents are related in the following way [104]

$$M_z = \frac{1}{c} \int dS (\mathbf{r} \times \mathbf{j})_z, \quad (3.8)$$

where  $\mathbf{r}$  is the position and  $\mathbf{j}$  is the current operator, and the integral  $\int dS$  runs over the plane. The current  $\mathbf{j}$  is described on each bond  $(i, j)$  by

$$J_{ij} = i \frac{et}{\hbar} \left( e^{i2\pi\phi_{ij}} c_i^\dagger c_j - \text{h.c.} \right) \quad (3.9)$$

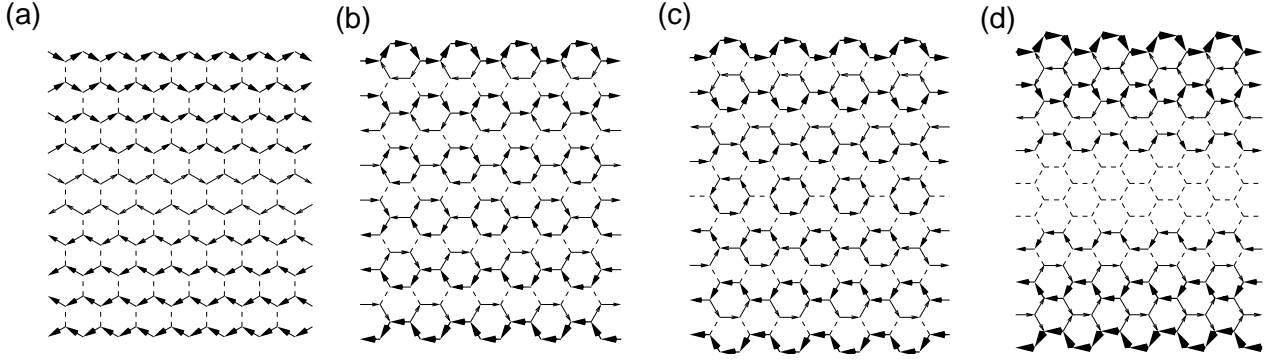


Figure 3.4: The texture of the ring currents for (a) zigzag ribbon ( $N=10$ ) and armchair ribbons of (b)  $N=18$ , (c)  $N=19$  and (d)  $N=20$ . In zigzag ribbon, because of the symmetry of the lattice, the ring currents along the vertical bonds are zero. In armchair ribbons of  $N=18$  and  $19$ , the Kekulé pattern is clear.

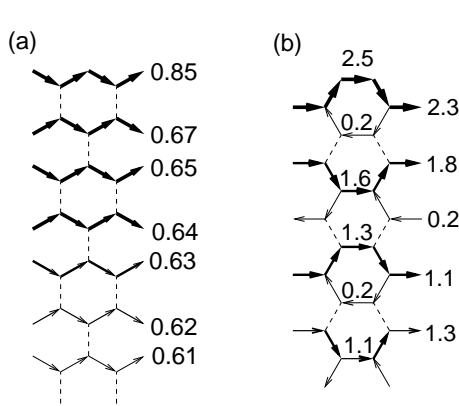


Figure 3.5: Current flow and magnitude near the edge for (a) zigzag ribbon ( $N=50$ ) and armchair ribbon ( $N=50$ ).

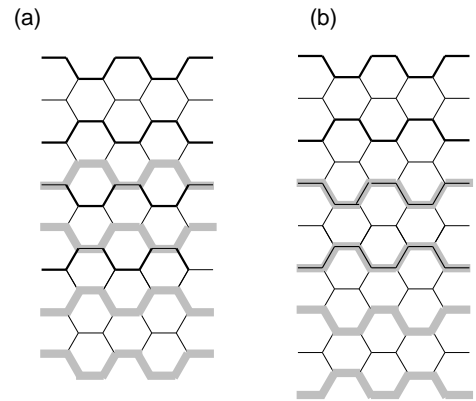


Figure 3.6: Schematic picture of ring current flow generated by the interference. Thick bold lines denote the right-going currents and thick shaded lines denote the left-going currents.

The ring currents also contribute to the linear response for weak magnetic fields. It is straightforward to calculate them and the corresponding susceptibility. The pattern of the ring currents for (a) a zigzag ribbon of  $N=10$ , and armchair ribbons of (b)  $N=18$ , (c)  $N=19$  and (d)  $N=20$  are shown in Fig. 3.4(a)-(d), respectively. The magnitude (in the units of  $J_0(= \frac{e\hbar}{h})$ ) and directions of the ring current near the graphite edge are given in detail in Fig 3.5. We can easily find that the current flow is symmetric with respect to  $x = 0$  and the total current in  $y$ -direction vanishes, because we consider an equilibrium state. The pattern of the current flow is strikingly different for the zigzag and the armchair ribbons. In zigzag ribbons, due to the lattice symmetry, the currents along the vertical bonds are exactly zero. The currents flow only along the horizontal bonds, whose directions are antisymmetric with respect to  $x = 0$ . For armchair ribbons, the current distribution is quite different, because currents flow also on vertically oriented bonds, and exhibits a clear Kekulé pattern. Note that the Kekulé pattern is more pronounced when  $N \neq 3M - 1$  ( $M=1,2,3, \dots$ ), which corresponds to the semiconducting armchair ribbon, whereas it is less distinct for the metallic case,  $N = 3M - 1$  ( $M=1,2,3, \dots$ ), where almost no currents are found close to the ribbon center. The reason can be attributed to the interference effect between the current flows associated with the two edges. As shown in Fig. 3.5(b), the currents are stronger along the cis-polyacetylene which is separated by one dimer line. For  $N \neq 3M - 1$  and  $N = 3M - 1$ , the ring current patterns are depicted schematically in Fig. 3.6 (a) and (b), where thick bold lines denote dominant right-going currents while thick shaded lines are for the left-going currents. It is easy to find that for  $N \neq 3M - 1$  both types of lines tend to avoid each other and form a Kekulé pattern around the center of the ribbons. However, when  $N = 3M - 1$ , the lines lie perfectly on top of each other so that the left- and right-going currents cancel each other around the center of ribbon. Thus the effect of the lattice topology near the graphite edge drastically changes the ring current flow in the whole sample.

In Fig.3.7, the magnitude of the ring current susceptibility  $J$  is plotted as a function of  $x/W$  with a fixed position  $y$  for (a) zigzag ribbons, (b) armchair ribbons with ( $N \neq 3M - 1$ ) and (c) armchair ribbons with

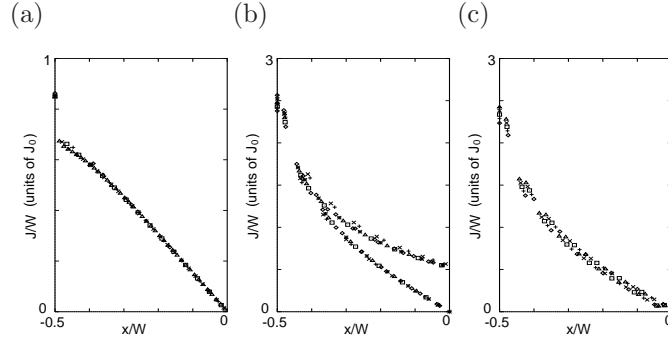


Figure 3.7: The position dependence of magnitude of the ring currents for (a) zigzag ribbons, (b) armchair ribbons ( $N \neq 3M - 1$ ) and (c) armchair ribbons ( $N = 3M - 1$ ).

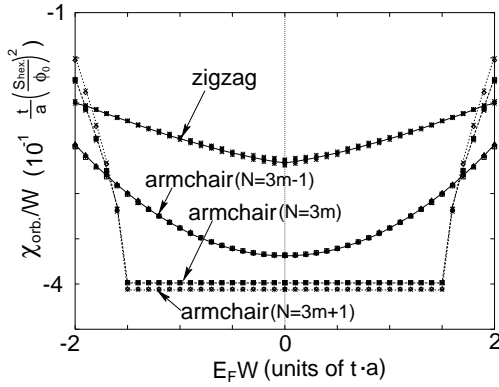


Figure 3.8: The Fermi energy dependence of the orbital magnetic moments  $\chi_{orb}$  of graphite ribbons at  $T=0$ .

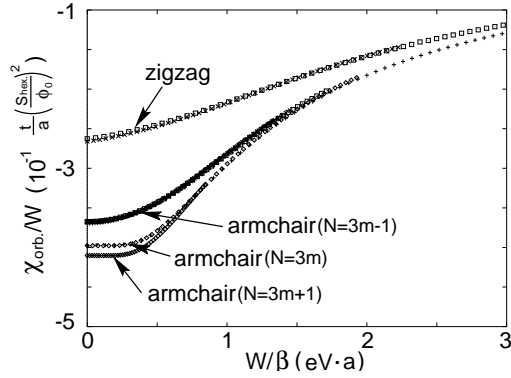


Figure 3.9: The temperature dependence of  $\chi_{orb}$ , where  $\chi_{orb}$  is scaled by  $1/W$  and  $\beta$  is scaled by  $W$ .

( $N = 3M - 1$ ). Interestingly, each graphite ribbon has a scaling behavior as a function of  $x/W$  and the magnitude of the ring currents has a power-law decay. These facts further emphasize that the edge shape effect is significant in nanographites.

### Scaling properties of the orbital magnetic susceptibility

Next we show the Fermi energy dependence of  $\chi_{orb}$ . Actually in real graphite materials, a small change in the carrier density from the half-filling is possible and can even be controlled by substrate properties. The calculated Fermi energy dependence is shown in Fig. 3.8, where it is found that  $\chi_{orb}/W$  is a universal function of  $\mu W$ . We normalize  $\chi_{orb}$  by dividing it by  $W$ , since it is proportional to  $W$  ( Fig. 3.3). Furthermore we multiply  $E_F$  by  $W$ , because the direct gap at  $k = 0$  is proportional to the  $1/W$  at  $k = 0$  for armchair ribbons and at  $k = 2\pi/3$  for zigzag ribbons for large  $W$ .

In Fig. 3.9, it is shown the temperature dependence of  $\chi_{orb}$ , which is important from the viewpoint of experiments on nanographites. In all cases the magnitude of  $\chi_{orb}$  decreases with increasing temperature. It is also found that the temperature dependence of  $\chi_{orb}/W$  scales as a function of  $\beta W$ , because the energy gap is proportional to the  $1/W$ . Our calculation also demonstrates that the edge effect becomes more significant with lower temperature. Similiar scaling properties can also be found in carbon nanotubes [105, 106].

## 3.3 Pauli Paramagnetism

In the previous section, we have seen that the orbital diamagnetic susceptibility depends on the edge shape in nanographite ribbons, especially, the topology of the lattice strongly affects the flow of diamagnetic ring currents. Here we discuss another important component of the magnetic susceptibility, Pauli paramagnetic susceptibility  $\chi_P$ , because zigzag ribbons have a sharp peak of DOS at the Fermi level. The width of this peak has the order of meV, which is comparable to the temperature scale of room temperature. Therefore, we expect that the Pauli susceptibility of zigzag ribbons might be sensitive to temperature, although the Pauli susceptibility of

usual metals is temperature independent. On the other hand, since the DOS of armchair ribbons at  $\epsilon = 0$  is zero or very tiny, we can neglect the effect of the Pauli paramagnetism in armchair ribbons.

The magnetic moment due to the Zeeman effect is

$$M = \mu_B (n_\uparrow - n_\downarrow), \quad (3.10)$$

where  $\mu_B$  is the Bohr magneton and  $n_\uparrow$  ( $n_\downarrow$ ) denotes the electron density with up-spin (down-spin). The electron density at arbitrary temperature for each spin is given by

$$n_\sigma = \frac{1}{\pi} \int_{1st\mathbf{BZ}} dk \sum_n \frac{1}{1 + e^{\beta(\epsilon_{n,k} - \sigma\mu_B H)}}, \quad (3.11)$$

where  $\sigma(=\uparrow, \downarrow)$  means spin index. Therefore, the Pauli susceptibility  $\chi_P$  per site is given by

$$\chi_P = \lim_{T \rightarrow 0} \frac{\partial M}{\partial H} = \frac{\beta\mu_B^2}{\pi N_e} \sum_n \int dk \frac{1}{\cosh(\beta\epsilon_{n,k})}, \quad (3.12)$$

where  $\beta = \frac{1}{k_B T}$ . Room temperature ( $T \sim 300\text{K}$ ) corresponds to  $\beta \sim 0.25$ . We numerically calculated the finite temperature Pauli susceptibility of graphite ribbons using this equation up to room temperature.

It is possible to separate the contribution of the edge states to  $\chi_P$ . As we have seen in Sec.2.2, the DOS due to the edge states is given by Eq.(2.31). After the substitution of Eq.(2.31) into Eq.(3.12), we replace the  $k$ -integration by the energy integration. Then we can obtain the  $\chi_P$  contribution due to the edge states as,

$$\chi_P = \frac{1}{N_e N \beta^\alpha} \int dx \frac{x^\alpha}{\cosh x + 1} \sim \frac{1}{N} T^\alpha, \quad (3.13)$$

where  $x$  is  $\beta\epsilon_k$  and  $\alpha$  is  $\frac{1}{N} - 1$ . Interestingly,  $\chi_P$  has the Curie-like temperature dependence. The exponent of  $\chi_P$  depends on the ribbon width through  $\alpha$ . When  $N$  becomes infinite, the exponent  $\alpha$  approaches  $-1$  and  $\chi_P$  show the Curie-law. However, in this limit, the contribution of  $\chi_P$  is diminished by a factor  $1/N$  in Eq.(3.13).

Numerical results of the Pauli susceptibility  $\chi_P$  of zigzag ribbons up to room temperature are shown in Fig. 3.10 for various values of  $N$ . As expected, because of the edge states,  $\chi_P$  shows Curie-like temperature dependence. In the inset of Fig.3.10, we plotted the  $N$  dependence of  $\alpha$ , which was calculated by the least square method and has a good agreement with the line of  $\frac{1}{N} - 1$ .

The observed susceptibility  $\chi$  is essentially the sum of the orbital  $\chi_{orb}$  and the Pauli susceptibility  $\chi_P$ . The temperature dependence of the total susceptibility  $\chi$  is shown in Fig.3.11. The total susceptibility  $\chi$  shows the diamagnetic behavior in the high temperature regime and paramagnetic behavior in the low temperature. In the inset, the width dependence of the crossing temperature, i.e.  $\chi = 0$ , is plotted, which is well fitted by  $\frac{1}{\beta} = 10^{0.1526} \times x^{-1.846}$ .

Here we should remind that both aromatic molecules and bulk graphite show diamagnetic behavior, however, nanographite with zigzag edges have a remarkable paramagnetic behavior because of the edge state. If this paramagnetic behavior is experimentally detected, it will be an indirect evidence of the existence of the edge state.

## 3.4 Magnetic Instability

The presence of the sharp peak in the density of states should induce the lattice distortion by the electron-phonon interaction and/or the magnetic polarization by the electron-electron interaction. Because of the non-bonding character of the edge states, the lattice distortion in the vicinity of the zigzag edges is unlikely with the realistic strength of the electron-phonon coupling [107]. The absence of the lattice distortion is also confirmed in terms of the density functional approach [108]. Thus we examine the effect of the electron-electron interaction by using the Hubbard model with unrestricted Hartree-Fock approximation, and successively random phase approximation. We have found a possibility of spontaneous magnetic ordering near the edge, peculiar to the nanometer scale fragments of graphite.

### 3.4.1 Mean field treatment in graphite ribbons

In order to study the magnetic instability in nano-graphene ribbons, we use the Hubbard model. The Hamiltonian is written as

$$H = -t \sum_{\langle \alpha, \alpha' \rangle} \sum_{\langle i, j \rangle, s} c_{\alpha, s}^\dagger(i) c_{\alpha', s}(j) + U \sum_\alpha \sum_i n_{\alpha, \uparrow}(i) n_{\alpha, \downarrow}(i), \quad (3.14)$$

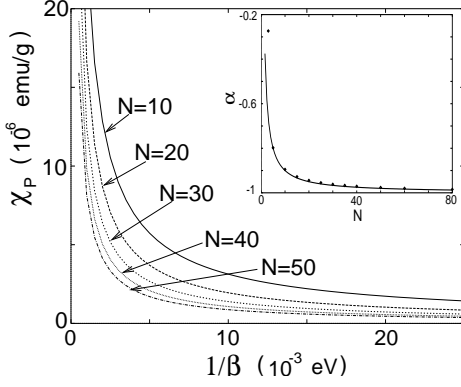


Figure 3.10: The temperature dependence of  $\chi_P$  for  $N=10, 20, \dots, 50$  up to room temperature. In the inset, the exponent is plotted on the width  $N$  and show a good agreement with the line of  $\frac{1}{N} - 1$ .

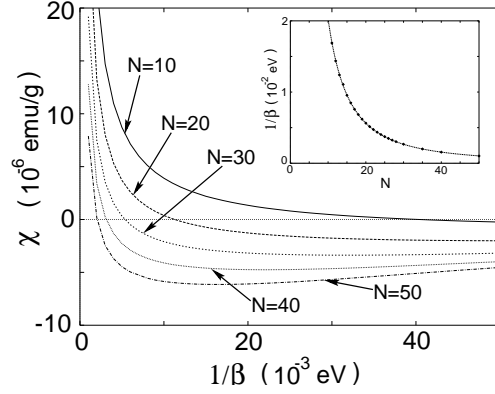


Figure 3.11: The temperature dependence of total susceptibility  $\chi$ , which is  $\chi_{orb.} + \chi_P$  is shown for  $N=10, 20, \dots, 50$ . In the inset, the width dependence of crossing temperature, where  $\chi = 0$ .

where the operator  $c_{\alpha,s}^\dagger(i)$  creates an electron with spin  $s$  on the site  $i$  of the unit cell  $\alpha$  and  $n_{\alpha,s}(i) = c_{\alpha,s}^\dagger(i)c_{\alpha,s}(i)$ . The indices of the sites in graphene ribbons are given shown in Fig.2.1 of the Chapter 2, and  $t$  and  $U$  are the nearest-neighbor transfer integral and on-site Coulomb repulsion, respectively. Here we solve the unrestricted Hartree-Fock (HF) Hamiltonian,

$$H = -t \sum_{\langle \alpha, \alpha' \rangle} \sum_{\langle i, j \rangle, s} c_{\alpha,s}^\dagger(i) c_{\alpha',s}(j) + U \sum_{\alpha} \sum_i (\langle n_{\alpha,\downarrow}(i) \rangle n_{\alpha,\uparrow}(i) + \langle n_{\alpha,\uparrow}(i) \rangle n_{\alpha,\downarrow}(i)) - U \sum_{\alpha} \sum_i \langle n_{\alpha,\uparrow}(i) \rangle \langle n_{\alpha,\downarrow}(i) \rangle \quad (3.15)$$

with the self-consistence conditions

$$m(i) = \frac{1}{L} \sum_k \langle a_{k\uparrow}^\dagger(i) a_{k\uparrow}(i) - a_{k\downarrow}^\dagger(i) a_{k\downarrow}(i) \rangle \quad (3.16)$$

$$= \frac{1}{L} \sum_k \sum_l^{occ.} \{ u_{k\uparrow}^*(i;l) u_{k\uparrow}(i;l) - u_{k\downarrow}^*(i;l) u_{k\downarrow}(i;l) \}, \quad (3.17)$$

where  $a_{k,s}^\dagger(i)$  is the Fourier transformed operator of  $c_{\alpha,s}^\dagger(i)$ ,

$$c_{\alpha,s}^\dagger(i) = \frac{1}{\sqrt{L}} \sum_k e^{ikr_\alpha} a_{k,s}^\dagger(i), \quad (3.18)$$

and  $\langle \dots \rangle$  denotes the expectation value in the HF state. The symbol  $u_{k,s}(i;l)$  denotes the matrix element of the following canonical transformation

$$a_{k,s}^\dagger(i) = \sum_l u_{k,s}^*(i;l) \gamma_{k,s}^\dagger(l) \quad (3.19)$$

in order to diagonalize the HF Hamiltonian with  $\gamma_{k,s}^\dagger(i)$  as the new quasi-particle operators. Since the zigzag ribbons have a bipartite-lattice structure, we solve the self-consistent equations assuming that the basic correlation is antiferromagnetic (AF).

In Fig.3.12, the  $U$  dependence of magnetization  $m$  for the zigzag ribbon of (a)  $N=2$ , (b)  $N=3$  and (c)  $N=10$  is shown. The dashed lines are HF solutions for a 2D graphite sheet. Similarly, we show the cases for armchair ribbons of (a)  $N=3$ , (b)  $N=4$  and (c)  $N=5$  in Fig.3.13. First, we can clearly see a peculiar feature for the zigzag ribbons, *i.e.*, large magnetic moments emerge on the edge carbons even for the weak  $U$ , which is explained as follows. Since the 2D graphite is a zero-gap semiconductor whose density of states (DOS) is zero at the Fermi level, the broken line stands up at a finite value  $U(=U_C)$ . This is consistent with the fact that graphite is non-magnetic, where  $U$  is expected to be much smaller than  $t$ . On the other hand, the zigzag ribbon has a large density of states at the Fermi level originating from the edge states. Thus, non-zero magnetic solutions can emerge for infinitesimally small  $U$  region as indicated in the present mean field result. However,

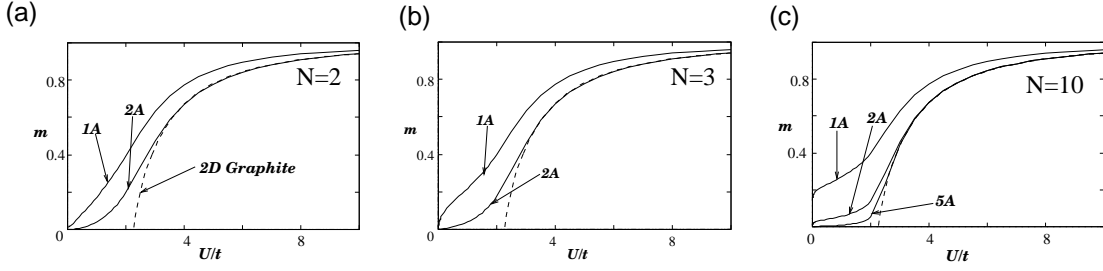


Figure 3.12: The  $U$  dependence of the magnetization  $m$  for the zigzag ribbons of  $N=(a)2$ , (b)3 and (c)10. The dashed lines mean the mean field solutions for the graphene sheet.

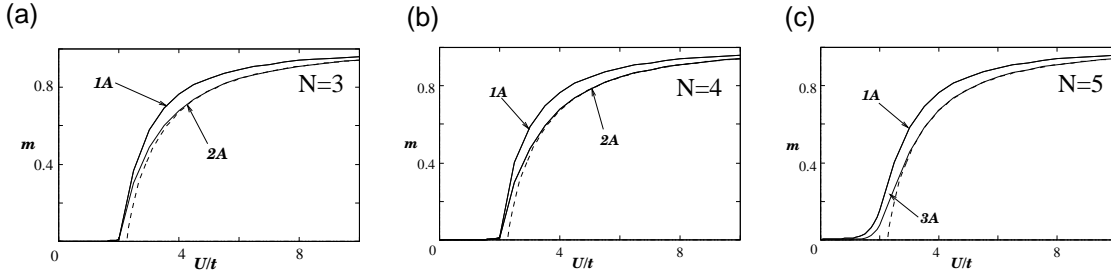


Figure 3.13: The  $U$  dependence of the magnetization  $m$  for the armchair ribbons of  $N=(a)3$ , (b)4 and (c)5. The dashed lines mean the mean field solutions for the graphene sheet.

special emphasis should be put on the behavior of the magnetization at the edge site 1A. As shown in Fig.3.12, the magnetization at the site 1A rapidly rises up and reaches about 0.2 even at small  $U$  ( $\approx 0.1$ ), when the width of ribbon is increased. We note that the armchair ribbon does not show such singular magnetic behavior as shown in Fig.3.13(a)-(c).

Next, we should also stress the local ferrimagnetic structure for the zigzag ribbons. We exhibit the magnetic structure of the ribbon with  $N = 10$  at  $U/t = 0.1$  in Fig.3.14, where spin alignment is visible at both edge sites. The origin of this structure is also explained from the nature of the edge states, which are responsible to the magnetization. Since the amplitude of the edge state is non-zero only on one of the two sublattices at an edge and damps inwards, the magnetic moment selectively grows on this sublattice forming local ferrimagnetic spin configuration, which is getting smaller and promptly on inner sites. The opposite edge sites, however, belong to the different sublattices, the total magnetization of the zigzag graphite ribbon is zero, although this vanishing total spin for the ground state is consistent with the exact statement of the half-filled Hubbard model [109].

In the Fig.3.15, the ribbon width,  $N$ , dependence of the magnetization at the most outer site (1A or NB). The magnitude of the magnetization rapidly increases with ribbons getting wider and then saturates around  $N = 10$ . This saturation value of the magnetization can be easily evaluated by the analytic solution of the edge states. From the analytic solution, the charge density on  $m$ -th zigzag chain is  $\left(4 \cos \frac{k}{2}\right)^{m-1}$ . Since the

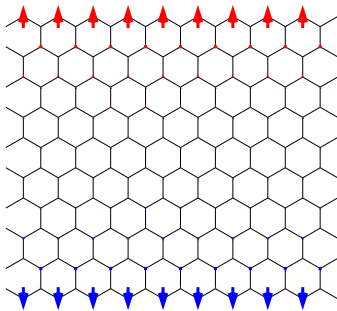


Figure 3.14: The schematic magnetic structure for the zigzag ribbon of  $N = 10$  at  $U/t = 0.1$ .

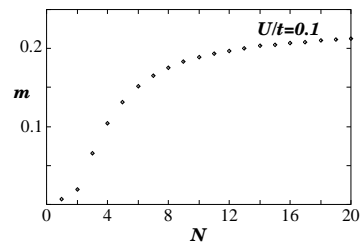


Figure 3.15: The ribbon width,  $N$ , dependence of the magnetization at the most outer site (1A or NB).

charge density from 1st zigzag chain is  $\frac{1}{1 - 4 \cos^2 \frac{k}{2}}$ , and the total charge density from 2nd zigzag chain except 1st zigzag chain is  $\frac{4 \cos^2 \frac{k}{2}}{1 - 4 \cos^2 \frac{k}{2}}$ , the charge density at 1A site is given as  $1 - 4 \cos^2 \frac{k}{2}$ . Thus in the region of  $0 \leq k \leq \frac{2\pi}{3}$ , the charge density at the 1A site is given as

$$\int_{\frac{2\pi}{3}}^{\pi} dk \left( 1 - 4 \cos^2 \frac{k}{2} \right) = \sqrt{3} - \frac{\pi}{3}. \quad (3.20)$$

At  $U/t = 0$  two partly flat bands are degenerate, the electron-electron interaction lifts this degeneracy and gives the magnetization of  $\frac{1}{3} m u_B$ . When we multiply  $\frac{1}{3}$  to Eq.(3.20), we obtain the saturation value of the magnetization at the 1A site as follows,  $\left( \sqrt{3} - \frac{\pi}{3} \right) \frac{1}{3} \sim 0.228$ .

### 3.4.2 Spin wave mode in graphite ribbons

The ferrimagnetic spin polarizations along the zigzag edges are interesting in view of the magnetic properties of nanographites. Nevertheless, the long-range order derived from the mean-field calculation is spurious, because no finite-momentum long-range spin order is expected in an one-dimensional system with full spin-rotation symmetry [110]. Even we may argue that quasi-long-range order, similar to the spin-1/2 Heisenberg chain, is not realized in zigzag ribbons of any finite width for the following reason. The unit cell of the ribbons contains an even number of sites such that Haldane's conjecture applies, i.e. the system should exhibit a spin gap [111]. This is very analogous to the case of the ladder systems with an even number of legs, which display a resonating valence bond (RVB) ground state, i.e., a short range correlated spin liquid state. With increasing of the ribbon width, however, the spin gap  $\Delta_s$  decreases exponentially due to the diminished overlap between two edges. In the limiting case of a semi-infinite graphite sheet, the state should, therefore, possess a gapless spin spectrum with quasi long range order. From this point of view, it is reasonable to study the low-lying spin excitations based on the HF result using the random phase approximation (RPA), which will give us in any cases gapless spin wave modes. These modes lie below the charge gap induced by the electron-electron interaction for any width of the ribbon so that they should remain always well-defined. We will use the RPA result to derive an effective Heisenberg spin model for the moments which emerge at the edges due to the electron-electron interaction.

Let us now turn to the collective mode associated with this peculiar magnetic structure of zigzag ribbons. We start with the following transverse dynamical susceptibility,

$$\chi_{i,j}^{+-}(q, \omega) = i \int dt e^{i\omega t} \langle [S_q^+(i; t), S_{-q}^-(j; 0)] \rangle, \quad (3.21)$$

where  $S_q^+(i; t)$  is the Heisenberg representation of  $S_q^+(i) = \sum_k a_{k+q\uparrow}^\dagger(i) a_{k\downarrow}(i)$ . Using the canonical transformation eq.(3.19), the dynamical susceptibility  $\chi_{ij}^{0+-}(q, \omega)$  for the mean field solution can be expressed in the Lehmann representation,

$$\chi_{ij}^{0+-}(q, \omega) = \sum_k \sum_l \sum_m^{\text{occ. unocc.}} \left\{ - \frac{u_{k+q\uparrow}^*(i; l) u_{k\downarrow}(i; m) u_{k\downarrow}^*(j; m) u_{k\uparrow}(j; l)}{\omega - \epsilon_k(m) - \epsilon_k(l)} + \frac{u_{k+q\downarrow}^*(i; l) u_{k\uparrow}(i; m) u_{k\uparrow}^*(j; m) u_{k\downarrow}(j; l)}{\omega + \epsilon_k(m) - \epsilon_k(l)} \right\}. \quad (3.22)$$

In order to take the bipartite structure of the AF correlation into account, it is convenient to distinguish between "uniform" and "staggered" spins,

$$\begin{aligned} \mathbf{S}_{iu; q} &= \sum_{\alpha} \mathbf{S}_{\alpha}(i) e^{iqr_{\alpha}}, \\ \mathbf{S}_{is; q} &= s(i) \sum_{\alpha} \mathbf{S}_{\alpha}(i) e^{iqr_{\alpha}}, \end{aligned}$$

where  $s(i)$  is +1 (-1) if the site  $i$  belongs to the A (B)-sublattice. The spin operators are given by

$$\mathbf{S}_{\alpha}(i) = \sum_{ss'} c_{\alpha, s}^\dagger(i) \boldsymbol{\sigma}_{ss'} c_{\alpha, s'}(i).$$

It is natural to introduce the following transformation for the dynamical susceptibility,

$$\begin{aligned} \chi_{ij}^{0+-uu} &= \chi_{ij}^{0+-}, & \chi_{ij}^{0+-us} &= s(j) \chi_{ij}^{0+-}, \\ \chi_{ij}^{0+-su} &= s(i) \chi_{ij}^{0+-}, & \chi_{ij}^{0+-ss} &= s(i) s(j) \chi_{ij}^{0+-} \end{aligned}$$

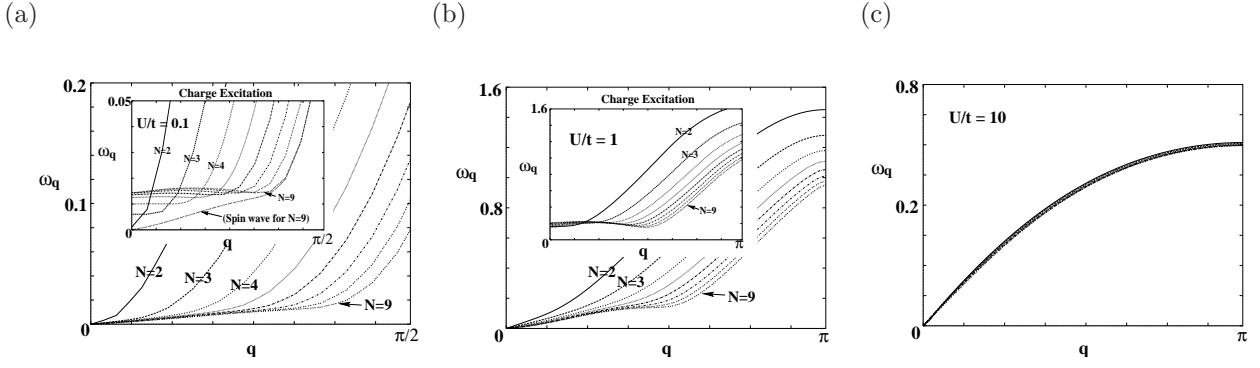


Figure 3.16: Spin wave modes for various ribbon widths of  $N = 2, 3, \dots, 9$  when  $U/t = 0.1$  (a),  $1.0$  (b) and  $10.0$  (c). The insets in (a) and (b) show the corresponding charge excitations.

From this, we obtain the equations for the response to the oscillating fields,  $h_{ju}^+(q, \omega)$  (uniform) and  $h_{js}^+(q, \omega)$  (staggered), and the corresponding mean fields [112],

$$\begin{aligned} \langle S_{iu;q}^+ \rangle &= \sum_j \chi_{ij}^{0uu}(q, \omega) (h_{ju}^+(q, \omega) + I \langle S_{ju;q}^+ \rangle) + \sum_j \chi_{ij}^{0us}(q, \omega) (h_{js}^+(q, \omega) + I \langle S_{js;q}^+ \rangle), \\ \langle S_{is;q}^+ \rangle &= \sum_j \chi_{ij}^{0su}(q, \omega) (h_{ju}^+(q, \omega) + I \langle S_{ju;q}^+ \rangle) + \sum_j \chi_{ij}^{0ss}(q, \omega) (h_{js}^+(q, \omega) + I \langle S_{js;q}^+ \rangle). \end{aligned}$$

The spectrum of the spin wave modes is indicated by the poles of the susceptibilities obtained from these equations.

The spin wave spectra are shown in Fig.3.16 for  $U/t = 0.1, 1.0$  and  $10$ , and various ribbon widths. Obviously, the spin wave spectrum is sensitive to both the interaction  $U$  and width  $N$ . For all widths and all finite  $U$  the spin wave spectrum has a basic linear dispersion around  $q = 0$  (and  $2\pi$ ) resulting in the aspect that the correlation is essentially antiferromagnetic. However, a strong quadratic dispersion are superposed due to the ferromagnetic character of the large moments appearing at each edge, as we can see clearly in Fig.3.16(a) ( $U = 0.1t$ ). This superposition completely disappear for  $U = 10t (> U_c)$  in Fig.3.16(c), where all sites generate a magnetic moment with well-developed Néel structure. In this case the dispersion very weakly depends on the width  $N$  and becomes entirely that of an AF system. The case of  $U = t$  can be considered as intermediate, because for small  $N$  it is more similar to the small- $U$  situation while for large  $N$  the low-energy spectrum resembles that of  $U = 10t$ . It is important to notice that the low-energy spectrum for all  $U > 0$  lies below the continuum of the quasiparticle excitations described by the mean field calculation (see insets in Fig.3.16(a),(b)). Therefore these spin waves represent well-defined undamped modes.

Now let us turn to the case of  $U = 0.1t$  where only the outermost moments at the edges are well-developed and can be considered as spin degrees of freedom on a lattice with two leg ladder structure. We can derive the effective Heisenberg model for these spins by analyzing the RPA spin wave spectrum,

$$H = \sum_{\langle i,j \rangle} J_{ij} \mathbf{S}_i \mathbf{S}_j, \quad (3.23)$$

where  $J_{i,j}$  is the effective spin-spin interaction not restricted to nearest neighbors as shown in Fig.3.17. By means of Holstein-Primakoff transformation, the spin wave spectrum deriving from the ordered state with parallel alignments of the spin along the edges and antiparallel between the edges.

$$\omega_q = \sqrt{\left( -4 \sum_{\mu} J_{\mu} \sin^2 \mu q + 2 \sum_{\mu} J'_{\mu} - J'_0 \right)^2 - \left( 2 \sum_{\mu} J'_{\mu} \cos 2\mu q - J'_0 \right)^2} \quad (3.24)$$

where  $J_{\mu}$  and  $J'_{\mu}$  denote intra- and inter-edge interactions, respectively. We use the least square fit method in order to determine  $J_{\mu}$  and  $J'_0$  from the RPA spectra ( $\mu = 1, \dots, 10$ ). Figure 3.18(a) and (b) show that  $J_{\mu}$  decreases fast with distance ( $|J_{\mu}| \propto \mu^{-\alpha}$ ,  $\alpha_{N=3} = 3.2$ ,  $\alpha_{N=9} = 2.2$ ), but weakly with  $N$ . On the other hand,  $J'_0$  and  $J'_1$  drop sharply with increasing  $N$ , where the results for  $N > 5$  are limited by the numerical accuracy. One important result in this context is the fact that the inter-edge interaction is almost two orders of magnitude smaller even in the case of  $N = 3$ . This suggests that the states of both edges contribute almost independently

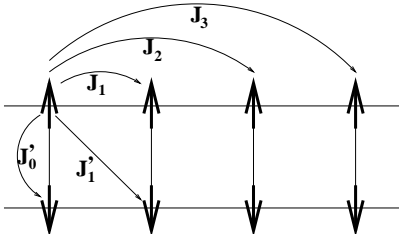


Figure 3.17: The definition of effective Heisenberg interactions of the ladder model fitted for the spin modes of zigzag ribbons

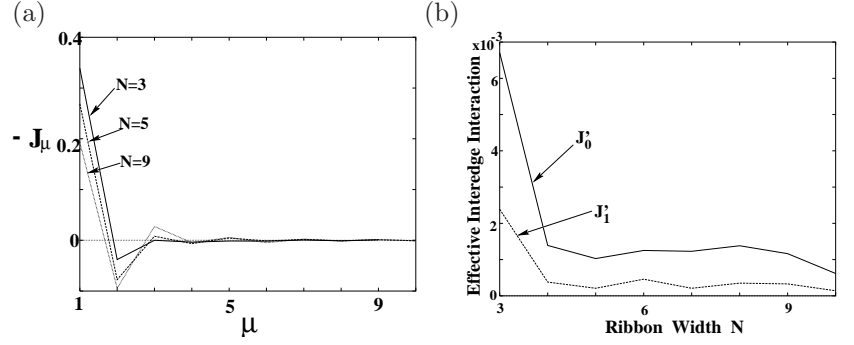


Figure 3.18: (a) Site dependence of effective Heisenberg interactions  $-J_\mu$  when  $N = 3, 5$ . (b) Ribbon width dependence of effective Heisenberg interactions  $J_0'$  and  $J_1'$  for interedge.

to the uniform susceptibility. The ferromagnetic correlation of the large moments leads to an enhancement of the paramagnetic signal in nanographite.

The spin system is Eq.(3.24) has a spin gap for finite  $J_0'$  and  $J_1'$ . The small value of  $J_0'$  suggests a small value of the spin gap,  $\Delta_s \sim J_0'$ . The accurate values are difficult to estimate even with exact diagonalization due to severe finite size effects for weakly coupled spin chains.

### 3.5 Summary and Discussion

In this chapter, we investigated the magnetic properties of nanographite systems. The characteristic features which we found in this chapter are listed below.

- **Orbital diamagnetism**

The orbital magnetic susceptibility  $\chi_{\text{orb}}$  of nanographites has the intermediate values between those of aromatic molecules and bulk graphites. The armchair ribbons show larger diamagnetic response than zigzag ribbons. The magnitude of  $\chi_{\text{orb}}$  linearly depends on the ribbon width. The  $\chi_{\text{orb}}$  can be scaled as the function of the Fermi energy, temperature and ribbon width. The difference of the  $\chi_{\text{orb}}$  between armchair and zigzag is attributed to the behavior of ring currents driven by magnetic fields.

- **Pauli diamagnetism**

Zigzag ribbons shows the large Pauli paramagnetic response at low-temperature due to the existence of the sharp peak in the density of states at the Fermi energy, while in armchair ribbons the Pauli paramagnetic susceptibility,  $\chi_{\text{Pauli}}$ , is negligible. Since the width of the peak is the order of meV, the  $\chi_{\text{Pauli}}$  is sensitive to the temperature, resulting in the Curie-like behavior. The temperature dependence of the  $\chi_{\text{Pauli}}$  is  $\frac{1}{N} \frac{1}{T^{1-1/N}}$  at low temperature, which originates from the form of the density of states of edge states. In nanographite systems, this paramagnetic response competes with the diamagnetic responses, resulting in the crossover from high-temperature diamagnetic response to low-temperature paramagnetic response.

- **Spin polarization**

The edge states are not stable even for small onsite Coulomb interaction, which yields localized spins of about  $0.2\mu_B$  at the edge sites. In zigzag ribbons, the spins ferrimagnetically align due to the nature of non-bonding edge states. The two magnetic states which polarized at the zigzag edge couple antiferromagnetically, resulting in the total magnetization being zero which is consistent with the Lieb's argument. Since the zigzag ribbons have even sites in the unit cell, the ground state of the system is considered as a resonating valence bond state, which induce a gap for the spin excitation. However, since the coupling between two edges rapidly decreases with increasing the width, the spin gap is negligible small when the ribbon width has a nanometer-scale.

The argument we discussed here is applicable to the other edge shapes having the non-bonding edge states, i.e. bearded and cove edges. Based on the discussion of the previous chapter, the non-bonding edge states are expected at the edges which are not parallel to the armchair edge. Thus, there is a class of nanographites which show the crossover from the paramagnetic response at low temperature and the diamagnetic response at high temperature can be assigned as the characteristic feature of the nanographite systems.

In the ACF-samples and graphitized nanodiamonds (see Chapter 1), the dangling bonds are terminated by the other elements. Nevertheless, their magnetic susceptibility shows Curie-Weiss behavior originating from localized spins. Since in the ACF and graphitized nanodiamond systems, the dangling bonds are terminated, the presence of dangling bond spins can be ruled out. Our results show that the non-bonding edge states give strong Pauli paramagnetic response even in the absence of electron-electron interactions. Thus, we conclude that the localized spin originating from the non-bonding edge states is one of the strong candidates to explain the behavior of magnetic response in nanographite systems.

Up to now, it has been considered that the graphite-related materials are quite silent for the magnetic response. However, our results suggest that in nanographite systems the paramagnetic response due to the non-bonding edge states are crucial, resulting in that the nanographites is assigned as a completely different systems from bulk graphites and aromatic molecules in the viewpoint of the magnetic properties.

---

# Chapter 4

## Transport Properties

---

In this chapter, we study the electronic transport properties of nanographite systems. The topology of  $sp^2$  carbon networks plays an important role not only for magnetic properties, but also for transport phenomena. Because of the non-bonding character of edge states, a single edge state cannot contribute to the electron transport. However, in zigzag ribbons, the edge states can provide a single channel for electron transport in the low-energy region, due to the bonding and anti-bonding configuration of two edge states which overlap from both edges. Here we analyze the conductance through the nanographene ribbon junctions and nanographene ribbon with non-magnetic impurities, based on the Landauer approach. The junctions analyzed here are systems which connect two zigzag ribbons with the same or different width. The conductance as a function of the Fermi energy shows rich structure in the single-channel energy region, in contrast to the case of related carbon nanotube systems. The remarkable feature in the behavior of the conductance is the appearance of sharp zero-conductance dip structures. Each zero-conductance dip is associated with a resonant state which can be interpreted as the superposition of two degenerate flux states with circulating current patterns. We also show that these conductance zeros are connected with pronounced negative magneto-resistance.

The organization of this chapter is as follows. First, we briefly introduce the multi-channel Landauer formula and the recursive Green's function method. Next we analyze the problem of single-barrier nanographene ribbon junctions and their zero-conductance resonances. Finally, we discuss the problems of non-magnetic impurities in zigzag ribbons. The results presented are partially published in Ref. [113].

### 4.1 Multi-Channel Landauer Formula

We use the multi-channel Landauer formula (MCLF) [114–116] in order to evaluate the conductance of nanographite junctions. This formula was originally developed for Anderson localization problems. Nowadays it is widely used in the mesoscopic and nanoscopic systems.<sup>1</sup> The MCLF derives the conductance from the scattering matrix. Through the scattering matrix,  $\mathbf{S}$ , the amplitudes of the scattering waves  $\mathbf{b}$  are related to the incident wave amplitudes  $\mathbf{a}$ :

$$\begin{bmatrix} \mathbf{b}_L \\ \mathbf{b}_R \end{bmatrix} = \mathbf{S} \begin{bmatrix} \mathbf{a}_L \\ \mathbf{a}_R \end{bmatrix} = \begin{bmatrix} \mathbf{r} & \mathbf{t}' \\ \mathbf{t} & \mathbf{r}' \end{bmatrix} \begin{bmatrix} \mathbf{a}_L \\ \mathbf{a}_R \end{bmatrix}, \quad (4.1)$$

where  $\mathbf{t}$ ,  $\mathbf{t}'$  are the transmission matrices,  $\mathbf{r}$ ,  $\mathbf{r}'$  are the reflection matrices and subscripts  $L$  and  $R$  denote the left and right lead lines. Conductance is defined in units of  $\frac{e^2}{\pi h}$  per spin by

$$g(E) = tr(\mathbf{t}^\dagger \mathbf{t}) = \sum_{\mu, \nu} |t_{\mu\nu}(E)|^2, \quad (4.2)$$

where  $t_{\mu\nu}(E)$  is a transmission coefficient from  $\nu^{\text{th}}$  to  $\mu^{\text{th}}$  channel at energy  $E$ . The scattering matrix can be written in terms of the site Green function. Through the site Green functions, the transmission coefficients can be connected to the tight binding model. In order to calculate the site Green functions efficiently, we adopt the recursive Green function technique [125–127].

<sup>1</sup>For reviews of mesoscopic systems, see references [117–123].

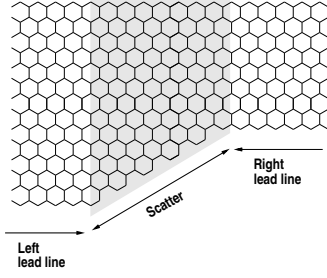


Figure 4.1: An example configuration of nanographite ribbon junctions. The shaded central region is the scatter. Lead lines (zigzag ribbons) are attached on the both of the scatter.

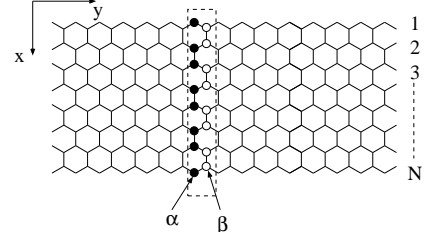


Figure 4.2: The structure of zigzag ribbon. We classify into 2 columns called  $\alpha$  and  $\beta$  in the unit cell. The rectangle with dashed lines is the unit cell.

An example of the nanographite ribbon junctions is depicted in Fig.4.1. The shaded central region corresponds to the scattering region, and the zigzag ribbons of the left and right parts correspond to lead lines. We need to know the Green function of zigzag ribbons in order to apply the recursive GF method, in the subsection 4.1.1.

#### 4.1.1 Zigzag ribbon as a lead line

Let us consider a zigzag ribbon of width  $N$ . We define the translational invariant direction as the  $y$ -axis and, the  $x$ -axis lies perpendicular to  $y$ -axis as shown in Fig.4.2. In zigzag ribbons, there are two kinds of columns in a unit cell, which we call  $\alpha$ - and  $\beta$ -column, respectively. The equations of motion on the zigzag ribbon in the  $j$ -th cell are given by

$$\begin{cases} (EI - \mathbf{H}_0^\alpha) \mathbf{C}_j^\alpha - \mathbf{V}^\dagger \mathbf{C}_j^\beta - \mathbf{V} \mathbf{C}_{j-1}^\beta = \mathbf{0} \\ (EI - \mathbf{H}_0^\beta) \mathbf{C}_j^\beta - \mathbf{V}^\dagger \mathbf{C}_{j+1}^\alpha - \mathbf{V} \mathbf{C}_j^\alpha = \mathbf{0} \end{cases}, \quad (4.3)$$

where  $\mathbf{C}_j^\alpha$  ( $\mathbf{C}_j^\beta$ ) is a vector ( $N \times 1$  matrix) describing the amplitudes of the  $\alpha$  ( $\beta$ )-column of  $j$ -th layer and  $\mathbf{H}_0^\alpha$  ( $\mathbf{H}_0^\beta$ ) denotes the column Hamiltonian of  $\alpha$  ( $\beta$ )-column. The  $\mathbf{V}$  ( $\mathbf{V}^\dagger$ ) represents the inter-column Hamiltonian describing hopping. From these two equations, we can obtain the following equation system,

$$\begin{bmatrix} EI - \mathbf{H}_0^\beta & 0 & -\mathbf{V}^\dagger & 0 & -\mathbf{V} \\ 0 & EI - \mathbf{H}_0^\beta & 0 & -\mathbf{V} & -\mathbf{V}^\dagger \\ -\mathbf{V} & -\mathbf{V}^\dagger & 0 & 0 & EI - \mathbf{H}_0^\alpha \end{bmatrix} \begin{bmatrix} \mathbf{C}_j^\beta \\ \mathbf{C}_{j-1}^\beta \\ \mathbf{C}_{j+1}^\alpha \\ \mathbf{C}_{j-1}^\alpha \\ \mathbf{C}_j^\alpha \end{bmatrix} = \mathbf{0}. \quad (4.4)$$

Using numerical or analytical methods, we eliminate the two variables of the  $\beta$ -column,  $\mathbf{C}_j^\beta$  and  $\mathbf{C}_{j-1}^\beta$ , to obtain the following Harper's equation,

$$\mathbf{C}_{j+1}^\alpha + \mathbf{u} \mathbf{C}_{j-1}^\alpha + \mathbf{v} \mathbf{C}_j^\alpha = 0, \quad (4.5)$$

and assume the Bloch form, i.e.,

$$\mathbf{C}_{j+1}^\alpha = \lambda \mathbf{C}_j^\alpha. \quad (4.6)$$

Therefore, the following eigenvalue problem is derived,

$$\lambda \begin{pmatrix} \mathbf{C}_j^\alpha \\ \mathbf{C}_{j-1}^\alpha \end{pmatrix} = \begin{pmatrix} -\mathbf{v} & -\mathbf{u} \\ 1 & 0 \end{pmatrix} \begin{pmatrix} \mathbf{C}_j^\alpha \\ \mathbf{C}_{j-1}^\alpha \end{pmatrix}. \quad (4.7)$$

This equation has  $2N$  eigenvalues and  $2N$  eigenvectors, which are classified into  $N$  right- and left-going waves. The  $N$  right-going solutions consist of traveling waves having the positive velocity in  $y$  direction and evanescent waves decaying exponentially in the positive  $y$  direction. Similarly, the  $N$  left-going solutions consist of traveling waves having the negative velocity in  $y$  direction and evanescent waves decaying exponentially in the negative  $y$  direction.

Let  $\mathbf{u}_1(-), \dots, \mathbf{u}_N(-)$  be the left-going solutions of  $\mathbf{C}_0^\alpha$  corresponding to  $\lambda_1(-), \dots, \lambda_N(-)$  and  $\mathbf{u}_1(+), \dots, \mathbf{u}_N(+)$  be the right-going solutions of  $\mathbf{C}_0^\alpha$  corresponding to  $\lambda_1(+), \dots, \lambda_N(+)$ . We then define two kinds of matrices,

$$\mathbf{U}(\pm) = (\mathbf{u}_1(\pm), \dots, \mathbf{u}_M(\pm)) \quad (4.8)$$

and

$$\Lambda(\pm) = \begin{bmatrix} \lambda_1(\pm) & & \\ & \ddots & \\ & & \lambda_M(\pm) \end{bmatrix}. \quad (4.9)$$

Any left- and right-going wave can be written, for example at  $j=0$ , as

$$\mathbf{C}_0^\alpha(\pm) = \mathbf{U}(\pm)\mathbf{C}^\alpha(\pm), \quad (4.10)$$

where  $\mathbf{C}(\pm)$  is an appropriate vector consisting of expansion coefficients. For general  $j$ , we have

$$\mathbf{C}_j^\alpha(\pm) = \mathbf{U}(\pm)\Lambda(\pm)^j\mathbf{C}^\alpha(\pm), \quad (4.11)$$

which leads to the relation

$$\mathbf{C}_j^\alpha(\pm) = \mathbf{F}(\pm)^{j-j'}\mathbf{C}_{j'}^\alpha(\pm), \quad (4.12)$$

with

$$\mathbf{F}(\pm) = \mathbf{U}(\pm)\Lambda(\pm)\mathbf{U}^{-1}(\pm). \quad (4.13)$$

We should note that  $\mathbf{U}(\pm)$  is not a unitary matrix in general.

### 4.1.2 The scattering problem

Now let us consider the scattering problem. We assume that the scattering object has  $N_s$  columns as shown in Fig.4.3, denoted from column 1 to column  $N_s$ . The 0-th column corresponds to the end of the left lead line, and the  $N_s+1$  column corresponds to the beginning of the right lead line. An infinite zigzag ribbon is attached to both sides of this scattering object as a lead. First, we separate the amplitude  $\mathbf{C}_0^\alpha$  at cell 0 into the right-going (incident) and left-going (reflected) solutions:

$$\mathbf{C}_0^\alpha = \mathbf{C}_0^\alpha(+)+\mathbf{C}_0^\alpha(-). \quad (4.14)$$

By using Eq.(4.12), the  $\mathbf{C}_{-1}^\alpha$  can be rewritten as follows,

$$\begin{aligned} \mathbf{C}_{-1}^\alpha &= \mathbf{C}_{-1}^\alpha(+)+\mathbf{C}_{-1}^\alpha(-) \\ &= \mathbf{F}^{-1}(+)\mathbf{C}_0^\alpha(+)+\mathbf{F}^{-1}(-)\mathbf{C}_0^\alpha(-) \\ &= \mathbf{F}^{-1}(-)\mathbf{C}_0^\alpha+\{\mathbf{F}^{-1}(+)-\mathbf{F}^{-1}(-)\}\mathbf{C}_0^\alpha(+). \end{aligned} \quad (4.15)$$

Let us consider the case where a zigzag ribbon is attached to the scattering object at 0-th column. In order to do this, we have to derive an equation which relates  $\mathbf{C}_0^\alpha$  to  $\mathbf{C}_0^\beta$  and  $\mathbf{C}_{-1}^\alpha$  in terms of the following equation,

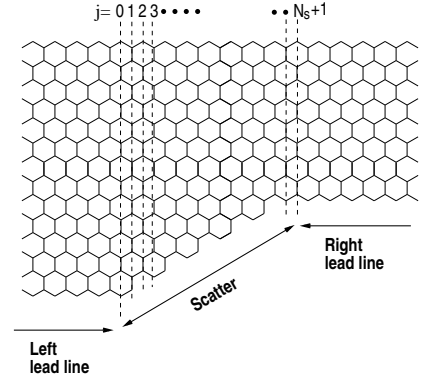


Figure 4.3: The columns in the scattering region are denoted by  $j=0,1,2,\dots,N_s,N_s+1$ .

$$\begin{bmatrix} EI - \mathbf{H}_0^\beta & -\mathbf{V} & 0 & -\mathbf{V}^\dagger \\ -\mathbf{V}^\dagger & EI - \mathbf{H}_0^\alpha & -\mathbf{V} & 0 \end{bmatrix} \begin{bmatrix} \mathbf{C}_{-1}^\beta \\ \mathbf{C}_0^\alpha \\ \mathbf{C}_0^\beta \\ \mathbf{C}_{-1}^\alpha \end{bmatrix} = 0. \quad (4.16)$$

The elimination of  $\mathbf{C}_{-1}^\beta$  gives

$$(\mathbf{EI} - \mathbf{H}_L)\mathbf{C}_0^\alpha - \mathbf{V}_L\mathbf{C}_0^\beta - \mathbf{V}_L^\dagger\mathbf{C}_{-1}^\alpha = 0. \quad (4.17)$$

Here we substitute Eq.(4.15) into the above equation in order to eliminate  $\mathbf{C}_{-1}^\alpha$ , then we obtain

$$(\mathbf{EI} - \mathbf{H}_L - \mathbf{V}_L^\dagger\mathbf{F}^{-1}(-))\mathbf{C}_0^\alpha - \mathbf{V}_L\mathbf{C}_0^\beta = \mathbf{V}_L^\dagger(\mathbf{F}(+)^{-1} - \mathbf{F}(-)^{-1})\mathbf{C}_0^\alpha(+), \quad (4.18)$$

and we introduce the new notation  $\tilde{\mathbf{H}}_L$ ,

$$\tilde{\mathbf{H}}_L = \mathbf{H}_L + \mathbf{V}_L^\dagger\mathbf{F}(-)^{-1}. \quad (4.19)$$

Then we obtain

$$(\mathbf{H} - \tilde{\mathbf{H}}_L)\mathbf{C}_0^\alpha - \mathbf{V}_L\mathbf{C}_0^\beta = \mathbf{V}_L^\dagger(\mathbf{F}(+)^{-1} - \mathbf{F}(-)^{-1})\mathbf{C}_0^\alpha(+). \quad (4.20)$$



From these equations, we can obtain the transmission coefficient  $t_{\mu\nu}$  for the incident channel  $\nu$  with velocity  $v_\nu$  and out-going channel  $\mu$  with velocity  $v_\mu$  as

$$t_{\mu\nu} = \left[ \frac{v_\mu}{v_\nu} \right]^{1/2} \left\{ \mathbf{U}(+)^{-1} (N_s + 1 | \mathbf{G} | 0) \mathbf{V}_L^\dagger (\mathbf{F}(+)^{-1} - \mathbf{F}(-)^{-1}) \mathbf{U}(+) \right\}_{\mu\nu} \quad (4.32)$$

and the reflection coefficient  $r_{\mu\nu}$  for incident channel  $\nu$  and out-going channel  $\mu$  as

$$r_{\mu\nu} = \left[ \frac{v_\mu}{v_\nu} \right]^{1/2} \left\{ \mathbf{U}(-)^{-1} \left\{ (0 | \mathbf{G} | 0) \mathbf{V}_L^\dagger (\mathbf{F}(+)^{-1} - \mathbf{F}(-)^{-1}) - 1 \right\} \mathbf{U}(+) \right\}_{\mu\nu}. \quad (4.33)$$

Immediately after we obtained the transmission coefficient  $t_{\mu\nu}$ , we can evaluate the conductance by the Landauer formula,

$$G(E) = \frac{e^2}{\pi\hbar} \sum_{\mu,\nu} |t_{\mu\nu}(E)|^2. \quad (4.34)$$

Thus, the conductance is calculated through the site GF.

### 4.1.3 Recursive relation of the Green function

In order to evaluate the transmission and reflection coefficients, we have to calculate the Green functions. Most powerful strategy is the recursive Green function method. Let us define the following four Green functions by,

$$(j | \mathbf{G} | j) = [j | (\mathbf{E}\mathbf{I} - \mathbf{H}^{(j)})^{-1} | j] \quad (4.35)$$

$$(j | \mathbf{G} | 0) = [j | (\mathbf{E}\mathbf{I} - \mathbf{H}^{(j)})^{-1} | 0] \quad (4.36)$$

$$(0 | \mathbf{G} | j) = [0 | (\mathbf{E}\mathbf{I} - \mathbf{H}^{(j)})^{-1} | j] \quad (4.37)$$

$$(0 | \mathbf{G} | 0) = [0 | (\mathbf{E}\mathbf{I} - \mathbf{H}^{(j)})^{-1} | 0] \quad (4.38)$$

where  $\mathbf{H}^{(j)}$  is the total Hamiltonian for the strip comprising the 0 to  $j$  cells excluding the intercell Hamiltonian  $\tilde{\mathbf{H}}_{j,j+1}$  and  $\tilde{\mathbf{H}}_{j+1,j}$ . Then the Green function for strips with any length can be obtained by a set of recursive formulas,

$$(j+1 | \mathbf{G}^{(j+1)} | j+1)^{-1} = \mathbf{E}\mathbf{I} - \tilde{\mathbf{H}}_{j+1} - \tilde{\mathbf{H}}_{j+1,j} (j | \mathbf{G}^{(j)} | j) \tilde{\mathbf{H}}_{j,j+1}$$

$$(j+1 | \mathbf{G}^{(j+1)} | l) = (j+1 | \mathbf{G}^{(j+1)} | j+1) \tilde{\mathbf{H}}_{j+1,j} (j | \mathbf{G}^{(j)} | l)$$

$$(l | \mathbf{G}^{(j+1)} | j+1) = (l | \mathbf{G}^{(j)} | j) \tilde{\mathbf{H}}_{j,j+1} (j+1 | \mathbf{G}^{(j+1)} | j+1)$$

$$(l | \mathbf{G}^{(j+1)} | l) = (l | \mathbf{G}^{(j)} | l) + (l | \mathbf{G}^{(j)} | j) \tilde{\mathbf{H}}_{j,j+1} (j+1 | \mathbf{G}^{(j+1)} | l),$$

where the suffix  $l$  must be less than  $j+1$ . In actual numerical calculations, we use the following Green function as a starting point for our recursive calculations.

$$(0 | \mathbf{G}^{(0)} | 0) = \left( \mathbf{E}\mathbf{I} - \tilde{\mathbf{H}}_L \right)^{-1}. \quad (4.39)$$

In terms of the above set of recursive relations, we can also calculate the Green function at arbitrary positions. By the analytic continuation, we can obtain the (local or total) density of states in the scattering region in terms of the following relation,

$$\rho(E) = -\frac{1}{\pi} \text{Im} \mathbf{G}(E + i\eta). \quad (4.40)$$

In addition, we can also obtain the behavior of the incident wave and current flow in the scattering region by this method.

## 4.2 Single-Barrier Nanographite Ribbon Junctions

### 4.2.1 Design of single-barrier nanographite ribbon junctions

Before we discuss the design of the junctions and their conductance properties, let us summarize a few important facts concerning the low-energy states for zigzag and bearded ribbons.

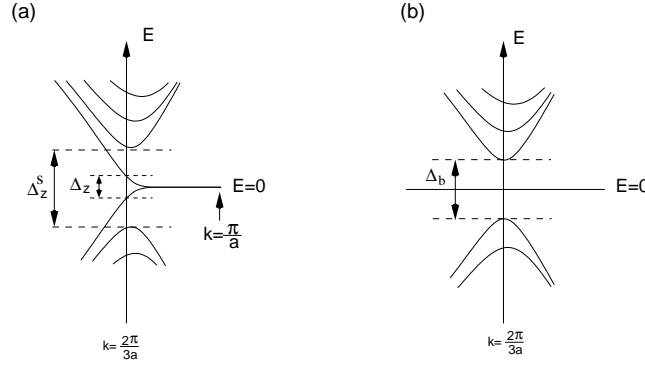


Figure 4.4: The band structure near  $E = 0$  of (a) zigzag ribbons and (b) bearded ribbons.

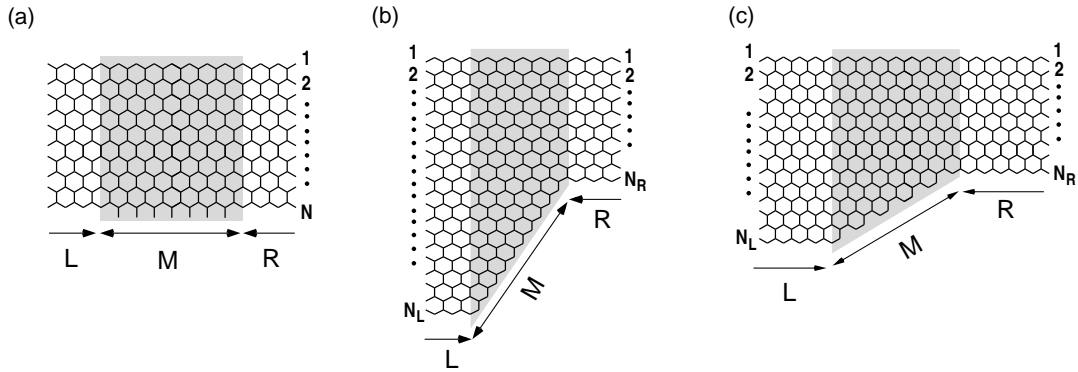


Figure 4.5: The structure of junction (a) I, (b) II and (c) III.

**Zigzag ribbon:** The zigzag ribbons are metallic for arbitrary ribbon width with an energy dispersion near  $E = 0$  as shown in Fig.4.4(a). The partly flat band appears at  $E = 0$  due to the edge states. Each edge state has a non-vanishing amplitude only on one of the two sublattices, i.e. non-bonding character. However, in a zigzag ribbon of finite width, two edge states coming from both sides, have a finite overlap. Because they are located on different sublattices, they mix into a bonding and anti-bonding configuration. In this way the partly flat bands acquire a dispersion. Note that the overlap is increasing as  $k$  deviates from  $\pi/a$ , because the penetration depth of the edge states increases and diverges at  $k = 2\pi/3a$ . The dispersion depends on the ribbon width  $N$  (number of zigzag lines from one side to the other), and has the approximate form

$$E_k = \pm 2tND_k^{N-1} \left[ 1 - \cos\left(\frac{ka}{2}\right) \right], \quad (4.41)$$

where  $D_k = 2 \cos\left(\frac{ka}{2}\right)$ . Thus, although the edge states on each side separately have non-bonding character, together through their overlap they provide one conducting channel except at exactly  $E = 0$ . The energy region of single-channel transport is restricted by the energy gap  $\Delta_z^s$  in Fig.4.4(a)

$$\Delta_z^s = 4t \cos\left[\frac{N-1}{2N+1}\pi\right]. \quad (4.42)$$

Note that  $\Delta_z^s$  is different from  $\Delta_z$  (Fig.4.4(a)), defined in the chapter 2, which is the direct gap of zigzag ribbons at  $k = \frac{2}{3}\pi$ .

**Bearded ribbon:** The bearded ribbon has one zigzag edge and one edge which has additional bonds (beard) to the zigzag edge. Here the edge states of both edges exist on the same sublattice. Consequently, there is no mixing between these edge states that would remove the non-bonding character, and we obtain a completely flat band at  $E = 0$  for any width  $N$ . The absence of dispersion leads to the insulating behavior for the edge state channel. The gap to the first conducting channel depends on  $N$  and is given by

$$\Delta_b = 4t \cos\left[\frac{N}{2N+2}\pi\right]. \quad (4.43)$$

Now let us turn to the design of junctions. In this section we study three types of junctions sandwiched by two zigzag ribbons denoted by L and R. The middle region shall be denoted by M. The junction I is depicted in Fig.4.5(a). The M-region between the two zigzag ribbons of width  $N$  is a bearded ribbon which has  $l$  attached bonds. This is an example to illustrate the peculiar features of transport properties in zigzag ribbon junctions, regardless of the question as to whether bearded ribbons could be realized in nature. It should be noted that this model represents a metal-insulator-metal junction. In Fig.4.5(b) and (c), the junction II and III are depicted. These junctions connect zigzag ribbon leads of different width. The M-region contains a tilted zigzag edge for junction II and an armchair edge for junction III. These junctions are more realistic than the junction I. In the junction II and III, the length of the M-region is proportional to  $N_L - N_R$ .

### 4.2.2 Fermi energy dependence of conductance

In Fig.4.6 (a), the Fermi energy dependence of the ballistic conductance for the junction I with  $N = 20$  for the whole energy region, where the number of attached bonds is 0, 1 and 3. Since the system of  $l = 0$  is a perfect conductor, the ballistic conductance is proportional to the number of conducting channels at the Fermi energy, i.e. the number of subbands at the Fermi energy. The conductance has a clear step feature as a function of the Fermi energy. With increasing number of attached bonds, the conductance decreases due to the lattice imperfection. In the multi-channel energy region the structure of the function  $G(E)$  is rather smooth, however in the single-channel region near  $E = 0$  the conductance has strong features. The Fermi energy of undoped systems is at  $E = 0$ . Since in realistic systems the low-energy region near the Fermi energy is more important, we shall investigate the behavior of the conductance in the low-energy region carefully. We show the Fermi energy dependence of the conductance of junction-I within the single-channel region,  $|E| < \Delta_b/2$ , in the Fig.4.6(b), and (c) with log-scale for the Fermi energy. We can find that the conductance has zero-conductance dips. The number of dips increases with increasing the number of the attached bonds, and simultaneously the maximum height of the conductance decreases. Interestingly, even one-attached bond makes a zero-conductance dip. We should note that near the bottom of the valence bands ( the top of the conduction bands ) which is also a single-channel region the dip structures of zero-conductance does not appear. Since the bottom of the valence bands ( the top of the conduction bands ) has the character of free electron, the appearance of the zero-conductance near  $E = 0$  dips is related to the topology of the lattice and the electron spectrum around  $E = 0$ . We should remark that the conductance of junctions connecting two nanotubes with different circumference does not show this type of dip structures [128].

Next we show the behavior of conductance for junction-II and junction-III in Fig.4.7 and Fig.4.8, respectively. In the Fig.4.7, the Fermi energy dependence of the conductance in junction II for (a) the whole energy region, (b) single conducting channel region and (c) single conducting channel region with log-scale are displayed. Here the single-channel region is given by  $|E| < \Delta_b(N_L)/2$ , where both leads have a single conducting channel, because the case of  $N_L > N_R$  give  $\Delta_b(N_L) < \Delta_b(N_R)$ . Similarly, in the Fig.4.8, we show the Fermi energy dependence of the conductance in junction-III for (a) the whole energy region and (b) single conducting channel region. In both types of junctions, we set the width of the left zigzag ribbon at  $N_L = 20$ , the width of the right zigzag ribbon is changed as  $N_R = 16, 14, 10$ . When  $N_L$  is equal to  $N_R$ , the system is a perfect conductor, so that the conductance is a step function of the Fermi energy. Since the maximum number of conducting channels is equal to the width of the lead lines, the maximum value of the conductance is equal to the width of the right zigzag ribbon, so that the conductance decreases with decreasing the width of right zigzag ribbon in the multi-channel region. Interestingly, although we can find sharp dips in the multi-channel region of  $|E| > 1$  for the junction-I, we cannot find such structures for the junction II and III. Now we shall see the low-energy transport properties. The behavior of the conductance of the junction II and III is qualitatively same in the multi-channel region. However, in the single-channel region near  $E = 0$ , the behavior of the conductance of the junction II and III is quite different. The conductance of the junction III is smooth even in the single-channel region, but the conductance of the junction II has dip structures analogous to the junction I. It should be noted again that in the single-channel region near the bottom of the valence band ( the top of the conduction band ), where the electrons have the nature of free electrons, there are no such dip structures. Increasing the length of the M-region, the conductance is lowered because of the enhanced reflection of the electron wave.

In the junction II, with increasing the length of the M-region, the number of the zero-conductance dips increases and the height of the conductance decreases. In the junction III, however, the dip structures of zero-conductance do not appear, and the conductance is a smooth function of the energy. The height of the conductance decreases with increasing the M-region. The tilted edge in II supports an edge state which, similar to the bearded ribbon, lies on the same sublattice as the edge state on the other side of the ribbon.

Thus, these results say that the edge structures play an important role in low-energy electronic transport properties. In next subsection, we shall see the behavior of the incident waves in the M-region in order to understand these zero-conductance states.

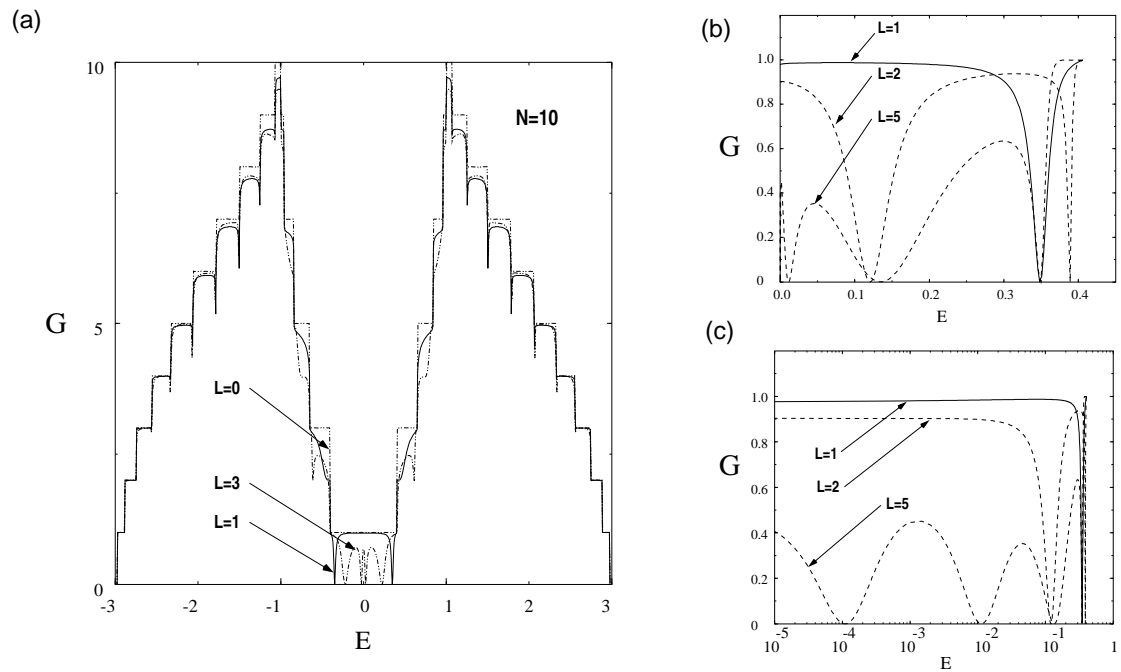


Figure 4.6: The Fermi energy dependence of the conductance of the junction I for (a) the whole energy region and (b) the energy region of single conducting channel.

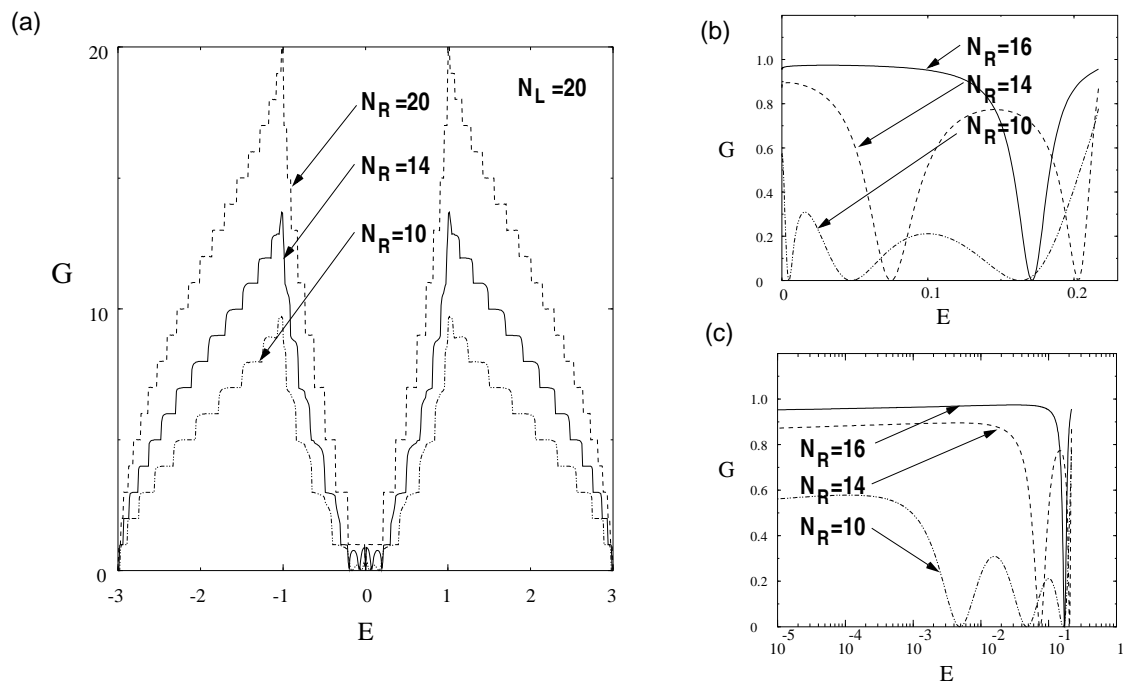


Figure 4.7: The Fermi energy dependence of the conductance of the junction II for (a) the whole energy region and (b) the energy region of single conducting channel.

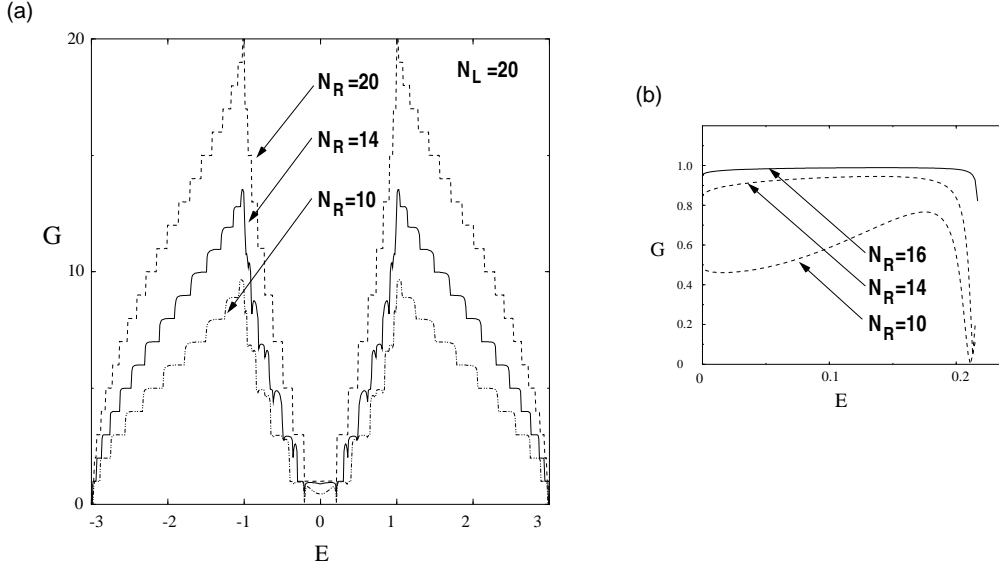


Figure 4.8: The Fermi energy dependence of the conductance of the junction III for (a) the whole energy region and (b) the energy region of single conducting channel.

### 4.2.3 Behavior of electron waves

The appearance of the zero-transmission dips in the junction I and II is connected with the formation of the resonant quasi-bound states in the M-region. According to quantum mechanics, the quasi-bound states are formed by the interference of the incident waves and reflected waves, resulting in the formation of standing waves in the M-region. Thus, we shall study the behavior of electron waves in the M-region.

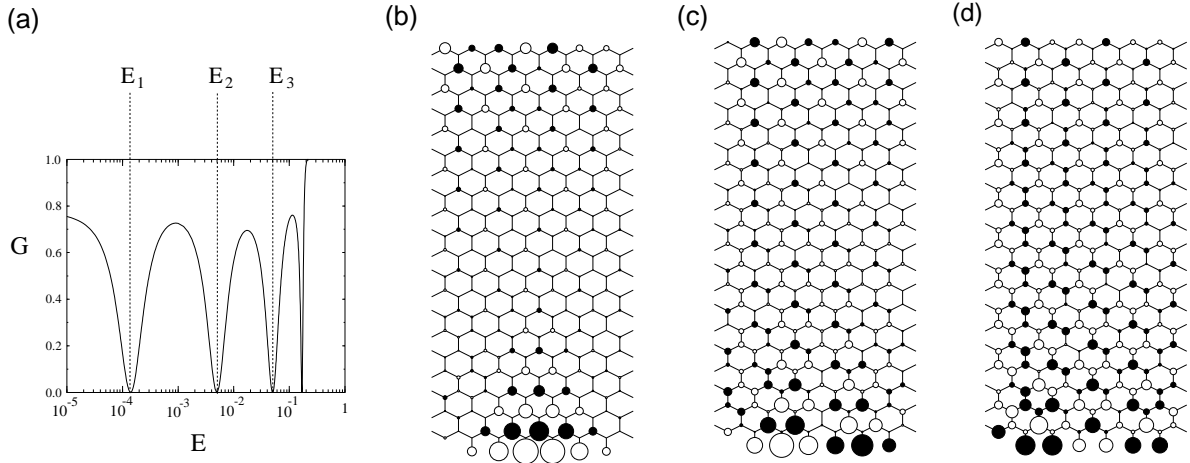


Figure 4.9: (a) The energy dependence of the conductance of the junction I with  $N = 20$  and  $l = 6$ . The electron waves of this junction at the energy (b)  $E_1$ , (c)  $E_2$  and (d)  $E_3$ . Here the radius of a circle and the black and white of a circle means the amplitude and sign of the electron waves.

In Fig 4.9 (a), we show the energy dependence of the conductance of the junction I with  $N = 20$  and  $l = 6$ , where the energy points of zero-conductance are marked with  $E_1$ ,  $E_2$  and  $E_3$  from lower energy side. The electron waves at  $E_1$ ,  $E_2$  and  $E_3$  are depicted in Fig.4.9 (b), (c) and (d), respectively. The radius of circles and the black and white of circles denote the amplitude and sign of the electron waves, respectively. In all of these figures, we can clearly see the formation of standing waves at the bearded edge in the M-region. Thus the appearance of the zero-conductance is connected with the formation of the standing waves in the M-region. The number of nodes of the standing wave increases with increasing energy. Shorter wave vectors correspond to higher energy. It should be also noted that the standing waves penetrate toward the inner sites of the ribbons with increasing the energy and the overlapping between two edge states coming from both edges becomes larger.

From now on, we call the standing-wave state with  $m$  hills as  $n = m$  state. Following this notation, the states of Fig.4.9 (b), (c) and (d) are called  $n = 1$ ,  $n = 2$  and  $n = 3$  state, respectively. This notation will be used again in later subsection concerning the negative magneto-resistance.

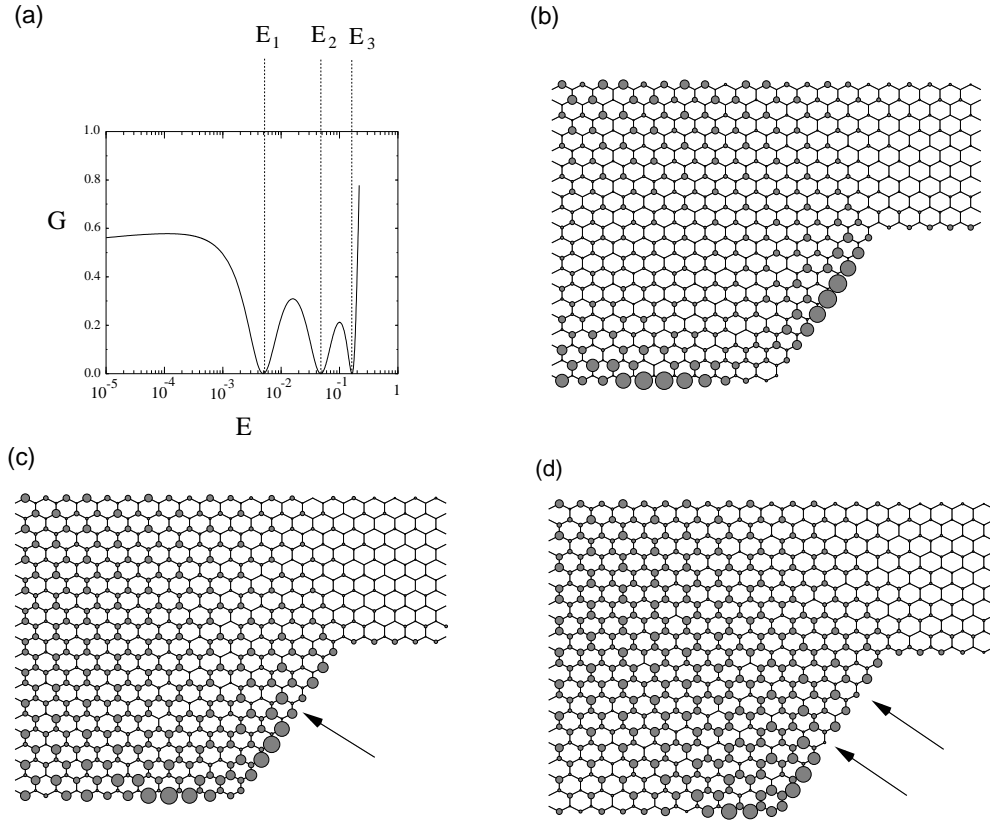


Figure 4.10: (a) The energy dependence of the conductance of the junction II with  $N_L = 20$  and  $N_R = 10$ . The electron waves of this junction at the energy (b)  $E_1$ , (c)  $E_2$  and (d)  $E_3$ .

Next we shall see the behavior of electron waves in the junction II. In Fig.4.10(a), the energy dependence of the conductance of the junction II with  $N_L = 20$  and  $N_R = 10$ . We again mark the energy points of zero-conductance with  $E_1$ ,  $E_2$  and  $E_3$  from the lower energy side. The electron waves at  $E_1$ ,  $E_2$  and  $E_3$  are depicted in Fig.4.10 (b), (c) and (d), respectively. We can see the clear formation of standing waves near the tilted zigzag edge in the M-region. Thus the appearance of the zero-conductance is due to the formation of the standing waves in M-region. The number of nodes of standing wave increases with increasing the Fermi energy analogous to the junction I.

Thus, also here the appearance of zero-conductance can be attributed to the formation of standing-waves in M-region of the junction. Hence the M-region of the junctions plays a role of single potential barrier for electron tunneling. In general, when the length of the potential barrier gets longer, the energy of the long-wavelength standing waves in M-region become smaller. This is the reason why the number of zero-conductance dips increases with increasing the length of the M-region. Of course, if the length of the M-region gets longer, the electron transmission is reduced, resulting in the decrease of the height of the conductance. The reason why the tilted armchair of the junction III does not show the standing waves is that the armchair edges do not have edge localized states at low-energy which could form this type of resonant standing wave.

#### 4.2.4 Flux states and large induced current vortex

In the previous subsection, we have pointed out the cause for the appearance of the zero-conductance from the viewpoint of the standing wave formations. This explanation is quite simple and reasonable. Here, we consider the behavior of currents near the zero-conductance dips. We find that the currents form the Kekulé-like vortex pattern in the M-region. We call this state “flux state”. We would like to demonstrate here that standing wave occurs due to the superposition of two flux states with time reversed current patterns.

We start with the study of the distribution of the currents in the M-region when the conductance is very close to zero. The currents flowing on each bond are calculated in terms of the current operator. In Fig.4.11(a),

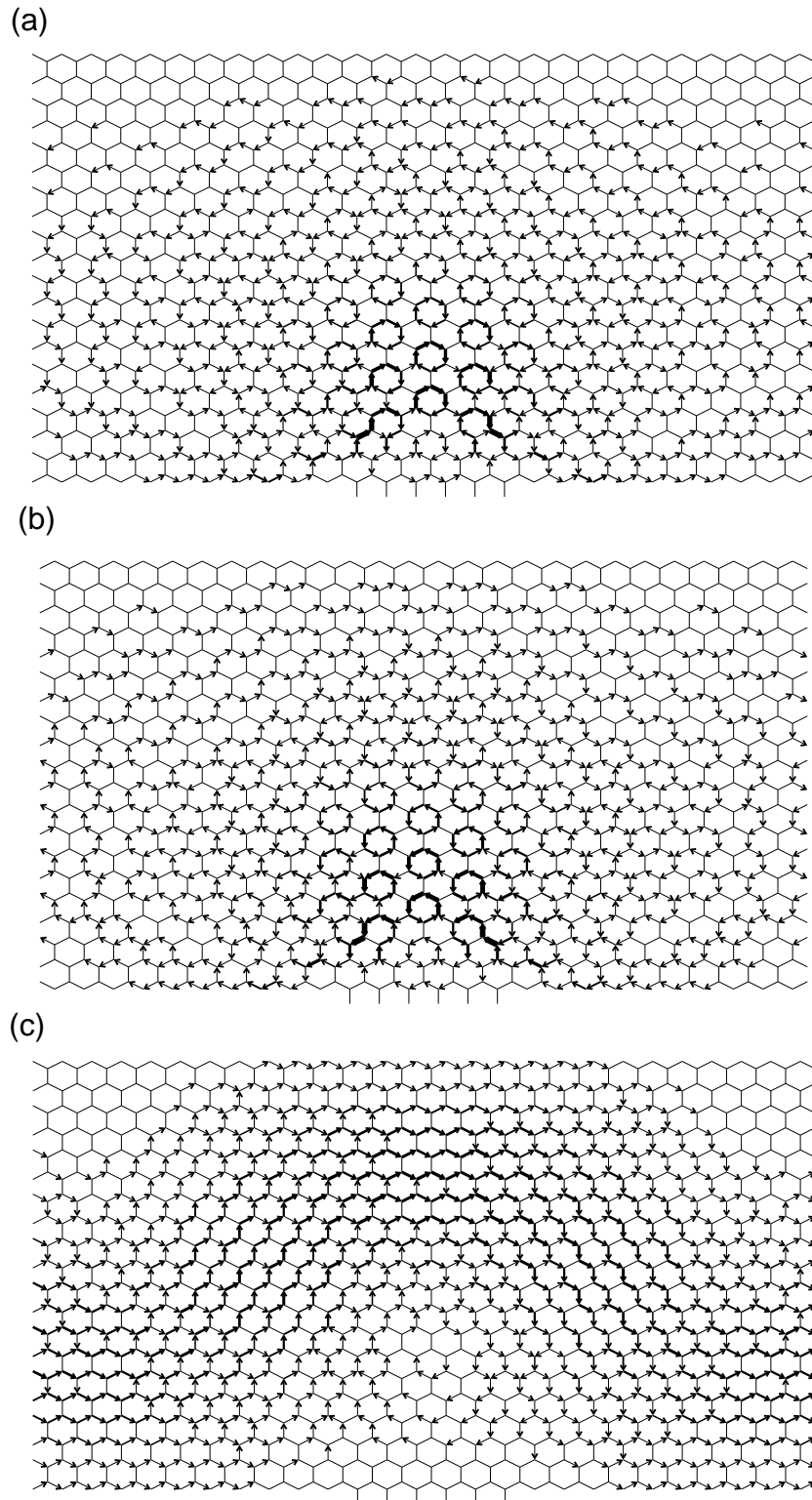


Figure 4.11: The distribution of currents in the M-region of the junction I with  $N = 20$  and  $l = 6$ , at (a)  $E = 0.049565t$  (immediately below  $E_2$  in the Fig.4.9), (b)  $E = 0.050289t$  (immediately above  $E_2$ ), and (c)  $E = 0.21517t$  where  $G = 0.72636$ .

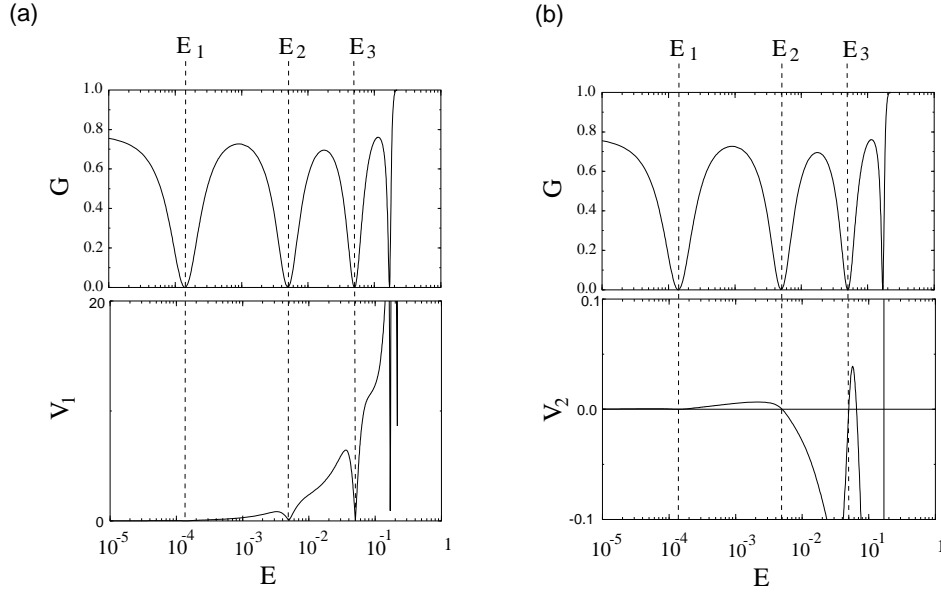


Figure 4.12: The Fermi energy dependence of (a)  $V_1$  and (b)  $V_2$ , together with the conductance, for the junction I of  $N = 20$  and  $l = 6$ .

we show the distribution of the currents for the junction I of  $N = 20$  and  $l = 6$ , at  $E = 0.049565t$  (immediately below  $E_2$  in the Fig.4.9(a).) The currents give rise to clockwise vorticity. When we look at the M-region carefully, we can observe the circulating currents which form a triangular Kekulé pattern. Interestingly we see large circulating currents in the M-region as a result of interference between the incoming electron waves and the reflected electron waves, while the magnitude of the net currents is very small. In Fig.4.11(a), we show the distribution of the currents for the same junction at  $E = 0.05029t$  (immediately above  $E_2$  in the Fig.4.9(a).) The overall circular current direction is reversed, i.e anti-clockwise. In Fig.4.11(c), we show the current distribution at  $E = 0.21517t$  far away from the zero-conductance dip, where  $G = 0.72636$ . Obviously no circulating current pattern appears in the M-region in this case.

In order to analyze the flux states quantitatively, we introduce the local “vorticity” in the following way. The vorticity is defined on the dual (triangular) lattice as the clockwise sum of the currents flowing on the bonds of each hexagonal ring. The local vorticity on the  $p^{\text{th}}$  hexagonal ring is given by

$$V_p = \sum_{i=1}^6 I_{i,p}, \quad (4.44)$$

where  $I_{i,p}$  means the current on the  $i^{\text{th}}$  bond of  $p^{\text{th}}$  hexagonal ring. In order to quantify the total of all circulating currents flowing in the junction, we take an average of  $|V_p|$ . Thus this quantity,  $V_1$ , is given by

$$V_1 = \langle |V_p| \rangle = \frac{\sum_p |V_p|}{\sum_p 1}. \quad (4.45)$$

The summation over plaquettes is taken not only in the M-region of the junction, but also including several columns on both sides of the M-region, because there is a “proximity effect” of the current pattern, i.e., the components of circulating currents penetrate into both the left and the right lead lines. Similarly, we also define the total vorticity of the junction,  $V_2$ , as

$$V_2 = \langle V_p \rangle = \frac{\sum_p V_p}{\sum_p 1}. \quad (4.46)$$

This physical quantity represents the direction of the total circulating current component of the junction. In Fig.4.12, the Fermi energy dependence of vorticity  $V_1$  and  $V_2$  is depicted for the junction I with  $N = 20$  and  $l = 6$  in the single conducting channel region. Both  $V_1$  and  $V_2$  linearly become zero at each energy of zero-conductance, i.e. not only the total vorticity  $V_2$  vanishes, but also no circular currents can be formed in each individual plaquette ( $V_1 = 0$ ). It should be noted that the vorticity  $V_2$  changes the sign at each zero-conductance energy point.

As we have shown in chapter 3, graphene ribbons with armchair edges can form a triangular Kekulé pattern of circular current driven by an external magnetic field. This reminds us of the fact that a hexagonal network is susceptible to a formation of a triangular Kekulé pattern of circular current. This can be examined by analyzing the susceptibilities in junctions for the formation of a triangular Kekulé pattern of circular current. We define two “response functions”, called  $\chi_V^{(1)}$  and  $\chi_V^{(2)}$ , as

$$\chi_V^{(1)} = \frac{V_1}{J} \quad \text{and} \quad \chi_V^{(2)} = \frac{V_2}{J}. \quad (4.47)$$

The first function is a measure for the presence of circular currents and the second for the overall vorticity of the system. Here  $J$  is the current passing through the junction from lead  $L$  to lead  $R$ . In a single-conducting channel region,  $J$  is written as

$$J = (1 - |r|^2)J_{\text{lead}} = |t|^2 J_{\text{lead}}, \quad (4.48)$$

where  $J_{\text{lead}}$  is the incoming component of the current on the source lead line from one of the reservoirs. Since in expression of  $J$  the currents coming back to the left lead due to the reflection are subtracted, the  $J$  is the net current flowing into the junction from the left lead line. In Fig.4.13, we show the Fermi energy dependence of the lead current ( $J_{\text{lead}}$ ) and incoming current ( $J$ ). The magnitude of the lead current is proportional to the group velocity of the conducting channel. Since the energy dispersion gets flatter with decreasing the Fermi energy, the lead current decreases. The current,  $J$ , becomes zero at each zero-conductance energy. Around each zero-conductance energy, the energy dependence of  $J$  is quadratic, i.e.  $J \propto (E - E_i)^2$  with  $i = 1, 2, \dots$ .

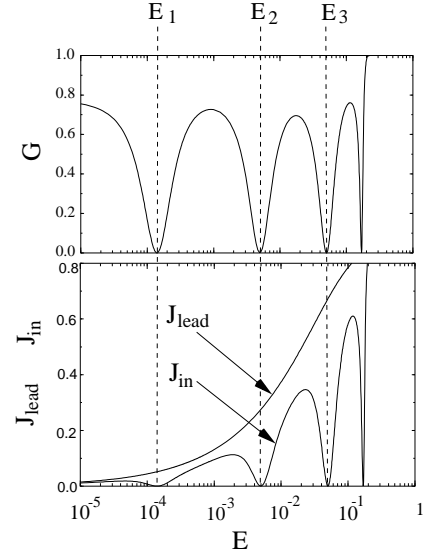


Figure 4.13: The Fermi energy dependence of the lead current,  $J_{\text{lead}}$ , and incoming current,  $J_{\text{in}}$  for the junction I of  $N = 20$  and  $l = 6$ .

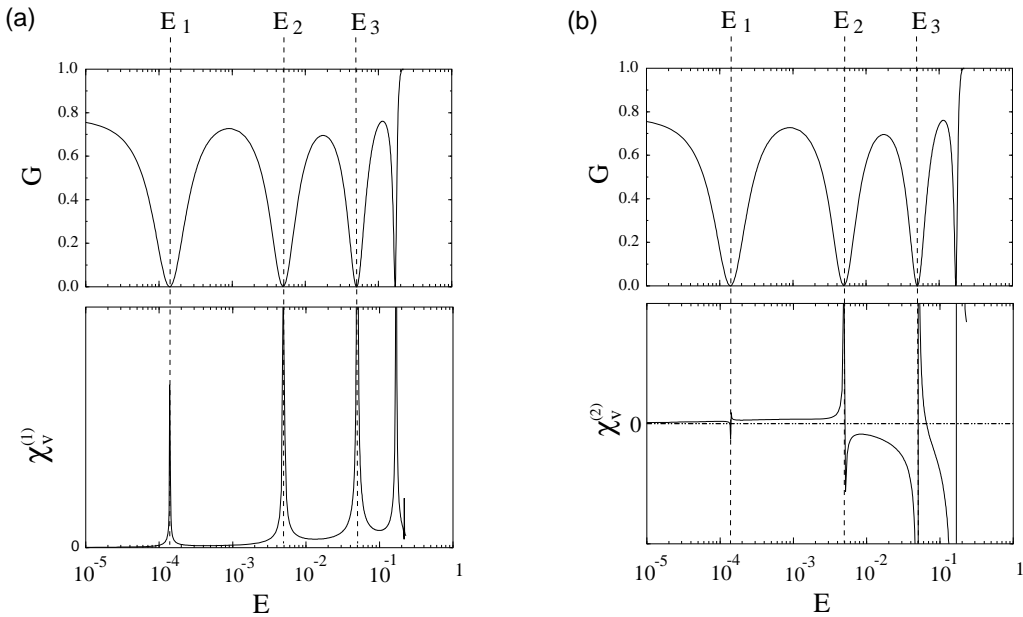


Figure 4.14: The Fermi energy dependence of (a)  $\chi_V^{(1)}$  and (b)  $\chi_V^{(2)}$  for the junction I with  $N = 20$  and  $l = 6$ .

At each zero-conductance point, the vortex  $V_1$  is a linear function of the Fermi energy, i.e.  $V_1 \propto |E - E_i|$  ( $i = 1, 2, \dots$ ), while  $J$  goes quadratically to zero. Therefore, the vortex  $V_1$  goes to zero more slowly than the incoming current. In Fig. 4.14, we show the Fermi energy dependence of two response functions,  $\chi_V^{(1)}$  and  $\chi_V^{(2)}$ , for the junction I with  $N = 20$  and  $l = 6$ . The susceptibilities  $\chi_V^{(1,2)}$  show sharp divergences, when  $E$  approaches the energy values of a zero-conductance dip. This means that small driving current  $J$  induce large circulating

currents in the M-region of the junction. We would like to emphasize that  $\chi_V^{(1,2)}$  are not defined at exact zero-conductance energies, because no driving current  $J$  can flow. Despite the fact that there is still a finite lead current and a current reflected from the junction at each zero-conductance energy, circular currents are exactly canceled. Consequently, the standing wave as a resonant level is formed by the superposition of a circular current state and its time-reversed state. The total vorticity measured by  $\chi_V^{(2)}$  changes sign at each resonance. Therefore, two flux states with opposite vorticity are degenerate at each zero-conductance energy point, resulting in the formation of the standing wave in the M-region.

The formation of Kekulé-like circulating current vortex pattern can be seen in the Fourier transform

$$F(\mathbf{k}) = \sum_p \frac{V_p}{J_{\text{in}}} \cos(\mathbf{k} \cdot \mathbf{r}_p), \quad (4.49)$$

where  $\mathbf{r}_p$  is the coordinate of the hexagonal ring center, and  $k_x(k_y)$  is wave number along (perpendicular to) zigzag lines in the junction. When the Kekulé-like trigonal lattice correlation of current vortex develops, the Bragg peaks appear at  $\mathbf{q}_1 = \frac{2\pi}{a} \left( \frac{1}{\sqrt{3}}, \frac{1}{3} \right)$  (or  $\mathbf{q}_2 = \frac{2\pi}{a} \left( 0, \frac{2}{3} \right)$ ) and  $\mathbf{q}_3 = 0$ . In Fig.4.15, we show the Fermi energy dependence of the  $F(\mathbf{k})$  at  $\mathbf{k} = 0$  and  $\mathbf{k} = \mathbf{q}_1$ . Clearly, the Bragg peaks are well developed in the vicinity of conductance zeros. Thus, we may characterize the quantum states associated with the resonances as *flux states*, in the sense that there is a pronounced correlation among the circular currents of the hexagonal rings. In Fig.4.15(c), the 3D plot of  $F(\mathbf{k})$  close to  $E = E_2$  is depicted. The pronounced trigonal correlation is confirmed.

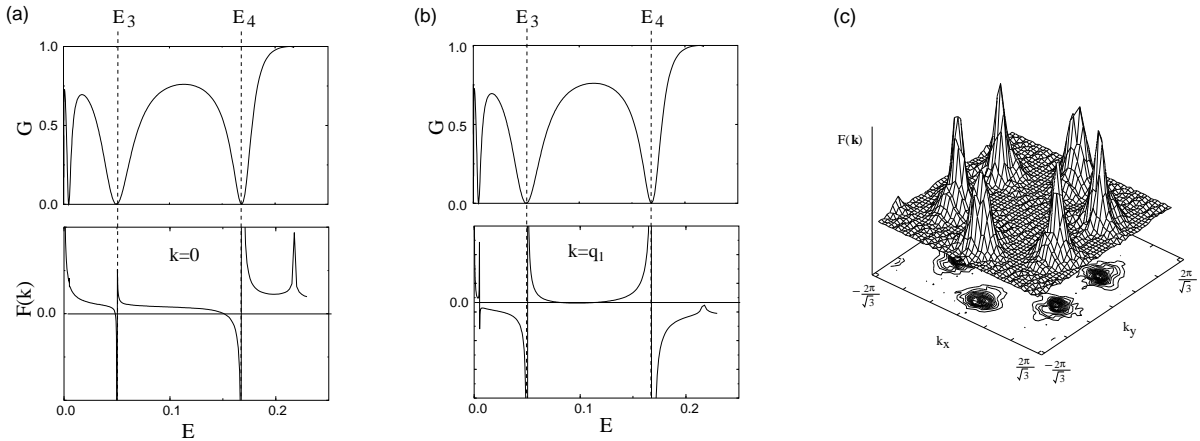


Figure 4.15: The Fermi energy dependence of the response functions, (a)  $\chi_V^{(1)}$  and (b)  $\chi_V^{(2)}$ , of the junction I with  $N = 20$  and  $l = 6$ . (c) The 3D plot of the correlation of circular current pattern in the M-region close to  $E = E_2$ .

#### 4.2.5 Origin of the zero-conductance resonance

In the previous section, we have seen that the appearance of zero-conductance resonances is related with the existence of resonant states in the M-region, which is visible as the formation of standing waves in the M-region. In this section, we explain the appearance of zero-conductance resonances in terms of standard scattering matrix approach considering the quantum waveguide systems with attached resonator [129, 130], following Shao [131] and Xu [132].

In order to introduce the scattering matrix theory, we first consider the quantum wire with a branch as shown in Fig.4.16(a). For this three-way geometry, where the branches are denoted by L, R, S for left, right and side branch, the three outgoing amplitudes with  $(O_S, O_L, O_R)$  are related to the three incoming waves with  $(I_S, I_L, I_R)$  through the  $3 \times 3$  scattering matrix,

$$\begin{bmatrix} O_S \\ O_L \\ O_R \end{bmatrix} = \mathbf{S} \begin{bmatrix} I_S \\ I_L \\ I_R \end{bmatrix} = \begin{bmatrix} r_{SS} & t_{SL} & t_{SR} \\ r_{LS} & r_{LL} & t_{LR} \\ r_{RS} & t_{RL} & r_{RR} \end{bmatrix} \begin{bmatrix} I_S \\ I_L \\ I_R \end{bmatrix}. \quad (4.50)$$

The elements of the scattering matrix represent the reflection amplitudes,  $r_{ij}$ , and the transmission amplitudes,  $t_{ij}$ , and from branch  $j$  to branch  $i$ . Here we implicitly assume that each branch has a only single conducting

channel. Current conservation requires that the scattering matrix is unitary, and time-reversal invariance constrains  $\mathbf{S}^* = \mathbf{S}^{-1}$ , i.e. the scattering matrix to be symmetric. Therefore, in general, there are five independent parameters under these constraints, and we can express the scattering matrix [133] as

$$\mathbf{S} = \begin{bmatrix} -(a+b) & \epsilon^{1/2} & \epsilon^{1/2} \\ \epsilon^{1/2} & a & b \\ \epsilon^{1/2} & b & a \end{bmatrix}, \quad (4.51)$$

where  $a = \frac{1}{2} [\sqrt{1-2\epsilon} - 1]$  and  $b = \frac{1}{2} [\sqrt{1-2\epsilon} + 1]$ . The parameter  $\epsilon$ , which varies in the range  $0 < \epsilon < \frac{1}{2}$ , measures the strength of the coupling between left, right and side wires. Next we close off the side wire, so that the outgoing wave  $O_S$  and the incoming wave  $I_S$  are forced to satisfy the relation

$$O_S = \lambda(E)I_S, \quad (4.52)$$

where  $\lambda = e^{i\Phi(E)}$  is the phase factor which describes the scattering in the resonator S. The energy-dependent phase  $\Phi(E)$  depends on the details of the resonator geometry.

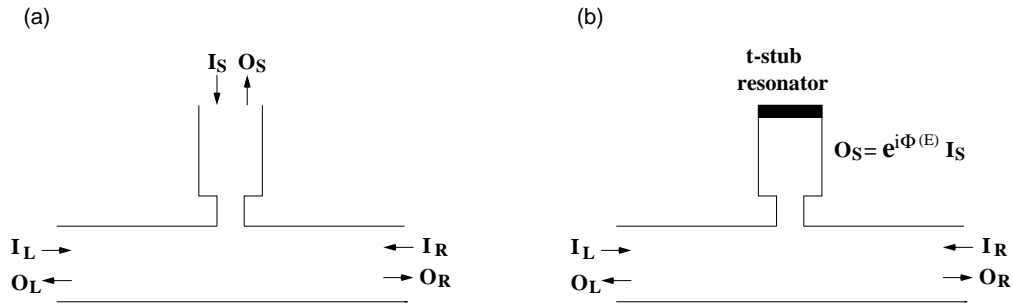


Figure 4.16: Schematic figure of a wire with a coupled cavity: (a) the quantum wire with a sidearm, (b) the quantum wire with a t-sub resonator which is obtained by closing off the sidearm.

Combining Eqs.(4.50) and (4.52), the above  $3 \times 3$  scattering matrix can be rewritten as

$$\begin{bmatrix} O_L \\ O_R \end{bmatrix} = \begin{bmatrix} \mathcal{R}_{LL} & \mathcal{T}_{LR} \\ \mathcal{T}_{RL} & \mathcal{R}_{RR} \end{bmatrix} \begin{bmatrix} I_L \\ I_R \end{bmatrix}, \quad (4.53)$$

where  $\mathcal{T}_{RL}$  denotes the transmission amplitude from left to right, and  $\mathcal{R}_{LL}$  is the reflection amplitude for the left-hand wire. The matrix elements are written as follows.

$$\mathcal{T}_{RL} = t_{RL} + \frac{t_{RS}t_{SL}}{\lambda - r_S}, \quad (4.54)$$

$$\mathcal{T}_{RL} = t_{RL} + \frac{t_{RS}t_{SL}}{\lambda - r_S}. \quad (4.55)$$

Note that the transmission amplitudes depend on the characteristics of the side-wire resonator, i.e.  $\lambda(E)$ . Let us expand the second term of Eq.(4.54) as follows,

$$\mathcal{T}_{RL} = t_{RL} + t_{RS} \left[ \frac{1}{\lambda} + \frac{1}{\lambda} r_S \frac{1}{\lambda} + \frac{1}{\lambda} r_S \frac{1}{\lambda} r_S \frac{1}{\lambda} + \dots \right] t_{SL}. \quad (4.56)$$

The geometric series in the brackets describe multiple reflections in the sidearm. Each round-trip in the sidearm involves a phase factor  $1/\lambda$ . The amplitude  $t_{SL}$  ( $t_{RS}$ ) represents the transmission from the left wire (sidearm) to the sidearm (right wire),  $t_{RL}$  denotes the transmission without a detour into the sidearm resonator. Thus, in general, the transmission through the scattering region consists of two independent terms: (i) the straight-through transmission without detour to the resonator, (ii) the transmission with multiple-scattering in the resonator. Consequently, this structure of the transmission amplitude gives the following properties in the complex-energy plane: (i) poles are possible in the geometric series of Eq.(4.56) in analogy to double-barrier resonant tunneling, and (ii) these poles induce the transmission zeros due to the cancellation of two terms. Therefore, we can represent the anti-resonance feature in terms of the following Breit-Wigner form,

$$t(E) = \tilde{t}(E) \left( 1 - \frac{i\Gamma/2}{E - E_0 + i\Gamma/2} \right) = \frac{\tilde{t}(E)(E - E_0)}{E - E_0 + i\Gamma/2}. \quad (4.57)$$

where  $\tilde{t}(E)$  is a regular complex function of  $E$  and  $\Gamma$  is the width of the resonance [134]. By using  $a$  and  $b$ , we can rewrite the transmission amplitudes as

$$\mathcal{T}_{\text{RL}} = b + \frac{\epsilon}{\lambda + a + b}, \quad (4.58)$$

$$\mathcal{R}_{\text{L}} = a + \frac{\epsilon}{\lambda + a + b}. \quad (4.59)$$

In this form of  $\mathcal{T}_{\text{RL}}$ , the transmission zeros occur at  $\lambda = -1$ . For the 1D resonator with an infinite potential barrier at its end,  $\lambda = \exp(-i2kL)$ , where  $k$  is the wave vector. Here  $L$  is the length of the attached resonator. Thus, the transmission zeros occur under the condition for which standing waves form in the resonator, i.e. at  $k = k_n$  with  $k_n = \frac{n}{L}\pi$  and  $n = 1, 2, \dots$

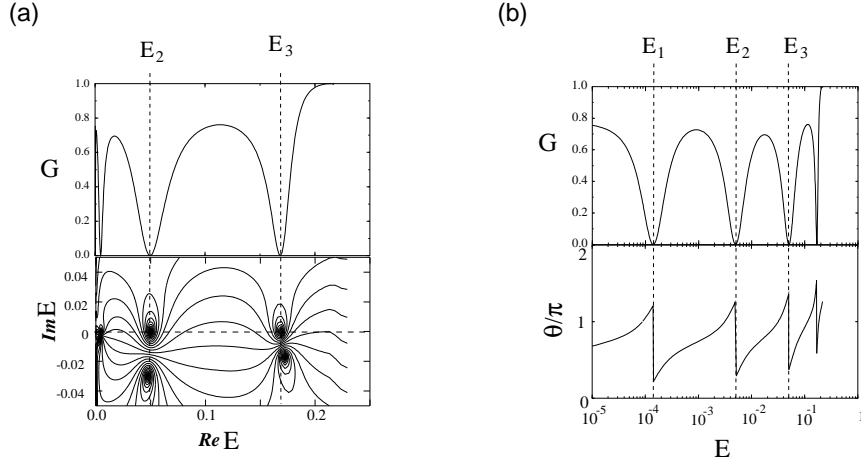


Figure 4.17: Numerical results for the junction I with  $N = 20$  and  $l = 6$ : (a) the contour plot of the absolute value of the transmission amplitude in the complex energy plane. The zero-pole pairs appear at each zero-transmission energy. (b) The energy dependence of the phase of the transmission.

Next let us consider the behavior of the phase,  $\theta_{\text{RL}}$ , acquired by the transmission, which is defined by

$$\theta_{\text{RL}} = \tan^{-1} \left[ \frac{\Im(t_{\text{RL}})}{\Re(t_{\text{RL}})} \right]. \quad (4.60)$$

Our main interest is the behavior of the phase when the transmission  $|t_{\text{RL}}|^2$  passes through zero. Let us consider the transmission coefficient  $t_{\text{RL}}$  in the close neighborhood of a transmission zero,  $2kL = 2n\pi + \delta$ . This gives  $\lambda = -e^{-i\delta}$ . The Eq.(4.58) expanded to the second order in  $\delta$ ,

$$t_{\text{RL}} = \frac{b^2}{D}\delta^2 + i\frac{2ab}{D}\delta, \quad (4.61)$$

where  $D = (a+b)^2 + 1 - 2(a+b)$ . Thus, for an infinitesimal value of  $\delta$ ,

$$\theta_{\text{RL}} = \tan^{-1} \left[ \frac{2a}{b\delta} \right]. \quad (4.62)$$

Note that  $a/b < 0$ . Thus,  $\theta_{\text{RL}} = \frac{\pi}{2}$  when  $\delta \rightarrow 0^-$  and  $\theta_{\text{RL}} = -\frac{\pi}{2}$  when  $\delta \leftarrow 0^+$ . Therefore,

$$\theta_{0^+} - \theta_{0^-} = -\pi. \quad (4.63)$$

This means that the phase abruptly changes by  $\pi$  when the transmission passes through zero.

The junction-I is a more complicated system than the quantum waveguide with attached resonator. Nevertheless, our numerical data are well fitted by the above arguments. In Fig.4.17(a), we show the contour plot of the absolute value of the transmission amplitude in the complex energy plane for the junction I with  $N = 20$  and  $l = 6$ . We can clearly find the zero-pole pair at each conductance energy points. In Fig.4.17(b), the phase of the transmission is depicted, where clear  $\pi$  phase jumps are observed at each conductance energy points.

### 4.2.6 Negative magneto-resistance

As we have seen, the appearance of conductance zeros is due to the time-reversal symmetry, where the standing waves form as a result of superposition of two flux states with different chirality. Since the application of magnetic field destroys the time reversal symmetry, the degeneracy of two flux states is lifted. Thus the zero-conductance features disappear resulting in a pronounced negative magneto-resistance.

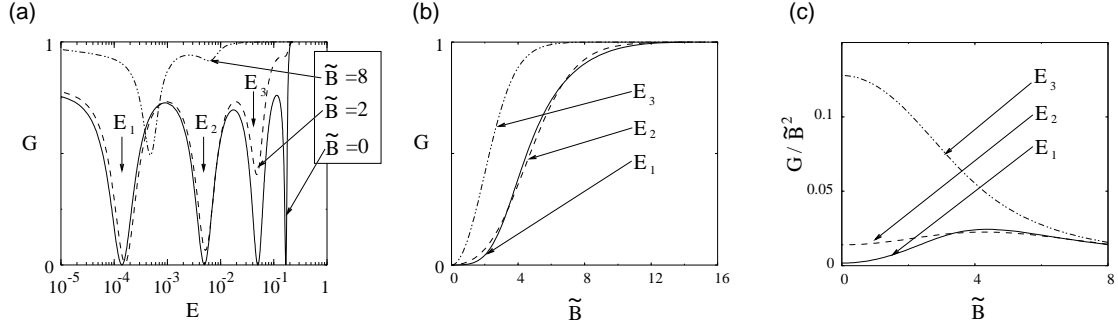


Figure 4.18: (a) The Fermi energy dependence of the conductance of the junction I with  $N = 20$  and  $l = 6$  when  $\tilde{B} = 0$  (bold line),  $\tilde{B} = 2$  (dashed line) and  $\tilde{B} = 8$  (broken line), within the single channel region. (b) The effective magnetic field dependence of the conductance at  $E = E_1, E_2$  and  $E_3$ . (c) The plots of  $G/\tilde{B}^2$  vs  $\tilde{B}$ .

For the case of the junction I with  $N = 20$  and  $l = 6$ , we show the Fermi energy dependence of the conductance in Fig.4.18(a), where the normalized magnetic field is set to 0, 4 and 16. The normalized magnetic field  $\tilde{B}$  is given as

$$\tilde{B} = \left(\frac{W}{d}\right)^2 \alpha B, \quad (4.64)$$

where  $W$  is the ribbon width in the L-region and  $d$  is the cyclotron diameter. As shown in Fig.4.18(a), the application of the magnetic field indeed removes the zero-conductance dips. In Fig.4.18(b), the magnetic field dependence of the conductance is shown at the energies of  $E = E_1, E_2$  and  $E_3$  for the same junction. The indices  $E_1, E_2$  and  $E_3$  specify the energy points of zero-conductance, given in Fig.4.18(a). In the strong magnetic field limit, the conductance becomes one in the whole single-channel region. Thus the application of the magnetic field removes the zero-conductance dips, and the system becomes a perfect conductor.

In Fig.4.18(c), the ratio of  $G/\tilde{B}^2$  vs  $\tilde{B}$  are shown. In the region of  $\tilde{B} < 1$ , the  $G/\tilde{B}^2$  becomes almost constant. In the region of  $\tilde{B} > 1$ , the conductance clearly has the dependence of the square of  $B$ . Thus, the conductance has the quadratic magnetic field dependence,

$$\frac{G}{\tilde{B}^2} = \alpha + (\text{higher order terms}) \quad (4.65)$$

where  $\alpha$  is a constant factor which represents the susceptibility of the conductance to the magnetic field. In Fig.4.19,  $L \ln(\alpha)$  is plotted versus the index  $n$  which specifies the resonant state of the standing wave. The bold (dashed) line represents the case of the junction I with  $N = 20$  ( $N = 30$ ). Here we plotted the case of  $L = 6, 8, 10$ . Interestingly, all data have approximately the same slope  $\gamma$ . Thus, the factor  $\alpha$  has the scaling relation,

$$\alpha = A(N, L) \exp\left(\gamma \frac{n}{L}\right). \quad (4.66)$$

This relation means that the zero-conductance dips at higher energies show stronger magneto-resistance, which is understood as follows. Leaving from  $E = 0$ , the coupling between two edge states is increasing, so that the strength of currents  $\mathbf{j}_B$  driven by the external magnetic field become larger. Since the magnetic field couples to the currents  $j_B$  through the vector potential  $\mathbf{A}$  with  $\mathbf{j}_B \cdot \mathbf{A}$ , the conductance-dips with higher energy show stronger magneto-resistance.

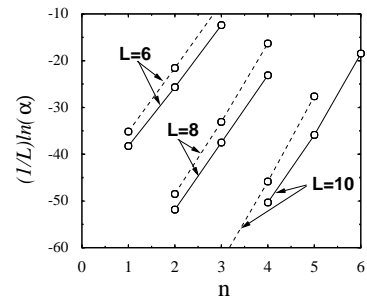


Figure 4.19: Scaling properties of magneto-resistance(see text).

### 4.3 Effects of Single Non-magnetic Impurity or a Lattice Vacancy

Since the flux states originate from the intrinsic chiral feature of graphite, flux states appear if we introduce the imbalance between two sublattices. Therefore, we can induce flux states not only in the nanographite ribbon junctions, but also in the zigzag ribbons with strong non-magnetic impurities or a lattice vacancy. As we have seen in previous section, some of nanographite junctions shows the zero-conductance dip structures in their single conducting channel region. The origin of zero-conductance is due to the destructive interference of a conventional and a resonant transmission channel, which is visible as flux states. The appearance of the flux state is due the imbalance of two sublattices introduced at the M-region. The imbalance of two sublattices can also be introduced by the existence of non-magnetic impurities or lattice vacancies in a nanographite ribbon. Thus we expect that these defects also induce the flux states, resulting in a zero-conductance dip. Furthermore, because of the extension to the 1-dimensional Anderson localization problem and the technological application, the impurity problem is of importance. Therefore, I study the impurity problem in this section.

#### 4.3.1 Single non-magnetic impurity in graphene sheet

Prior to the discussion of impurity problem in nanographite ribbons, let us consider a single impurity problem in a graphene sheet. The  $\mathbf{k} \cdot \mathbf{p}$  Hamiltonian having on-site potential impurity on a B site located at  $\mathbf{r}_0$  is given by

$$\begin{pmatrix} 0 & \hat{k}_x - i\hat{k}_y \\ \hat{k}_x - i\hat{k}_y & U\delta(\mathbf{r} - \mathbf{r}_0) \end{pmatrix} \begin{pmatrix} F_A(\mathbf{r}) \\ F_B(\mathbf{r}) \end{pmatrix} = \varepsilon \begin{pmatrix} F_A(\mathbf{r}) \\ F_B(\mathbf{r}) \end{pmatrix}, \quad (4.67)$$

where  $U$  is the magnitude of the impurity potential. We adopt the following Fourier transformation to the above  $\mathbf{k} \cdot \mathbf{p}$  equation,

$$\begin{pmatrix} F_A(\mathbf{r}) \\ F_B(\mathbf{r}) \end{pmatrix} = \frac{1}{\sqrt{N}} \sum_{\mathbf{k}} \begin{pmatrix} a_{\mathbf{k}} \\ b_{\mathbf{k}} \end{pmatrix} \exp(i\mathbf{k} \cdot \mathbf{r}). \quad (4.68)$$

Let us rewrite the onsite potential term in terms of the above Fourier transformation as follows,

$$U\delta(\mathbf{r} - \mathbf{r}_0) F_B(\mathbf{r}) = \frac{U}{N} \sum_{\mathbf{q}} \exp[i\mathbf{q} \cdot (\mathbf{r} + \mathbf{r}_0)] \sum_{\mathbf{k}} b_{\mathbf{k}} \exp(i\mathbf{k} \cdot \mathbf{r}_0) = \frac{U}{N} \sum_{\mathbf{k}} \exp[i\mathbf{k} \cdot (\mathbf{r} + \mathbf{r}_0)] G_0, \quad (4.69)$$

where  $G_0 = \sum_{\mathbf{k}} b_{\mathbf{k}} e^{i\mathbf{k}\mathbf{r}_0}$ . Therefore we can rewrite the  $\mathbf{k} \cdot \mathbf{p}$  equation as follows,

$$\begin{cases} \epsilon a_{\mathbf{k}} - (k_x - ik_y) b_{\mathbf{k}} & = & 0 \\ -(k_x + ik_y) a_{\mathbf{k}} + \epsilon b_{\mathbf{k}} & = & \frac{U}{\sqrt{N}} \exp(i\mathbf{k} \cdot \mathbf{r}_0) G_0 \end{cases}. \quad (4.70)$$

Then we obtain the following set of equations,

$$\begin{cases} a_{\mathbf{k}} = \frac{(k_x - ik_y) U}{\sqrt{L}} \frac{e^{i\mathbf{k}\mathbf{r}_0} G_0}{\epsilon^2 - (k_x^2 + k_y^2)} \\ b_{\mathbf{k}} = \frac{\epsilon U}{\sqrt{L}} \frac{e^{i\mathbf{k}\mathbf{r}_0} G_0}{\epsilon^2 - (k_x^2 + k_y^2)} \end{cases}. \quad (4.71)$$

From the definition of  $G_0$ ,

$$G_0 = \sum_{\mathbf{k}} b_{\mathbf{k}} e^{i\mathbf{k}\mathbf{r}_0} = \frac{\epsilon U}{\sqrt{L}} \sum_{\mathbf{k}} \frac{e^{2i\mathbf{k}\mathbf{r}_0} G_0}{\epsilon^2 - (k_x^2 + k_y^2)} \quad (4.72)$$

we obtain the self-consistent equation

$$\frac{1}{U} = \frac{\epsilon}{\sqrt{L}} \sum_{\mathbf{k}} \frac{e^{2i\mathbf{k}\mathbf{r}_0}}{\epsilon^2 - (k_x^2 + k_y^2)}. \quad (4.73)$$

The normalization of the wave functions is given as

$$\frac{1}{N} \sum_{\mathbf{k}} |a_{\mathbf{k}}|^2 = \frac{1}{N^2} U^2 G_0^2 \sum_{\mathbf{k}} \frac{|\epsilon_{\mathbf{k}}|^2}{[\epsilon^2 - |\epsilon_{\mathbf{k}}|^2]^2} = (\text{constant}) \times G_0^2 U^2 = 1 \quad (4.74)$$

and

$$\frac{1}{N} \sum_{\mathbf{k}} |b_{\mathbf{k}}|^2 = \frac{\epsilon^2}{N^2} U^2 G_0^2 \sum_{\mathbf{k}} \frac{1}{[\epsilon^2 - |\epsilon_{\mathbf{k}}|^2]^2} = (\text{constant}) \times G_0^2 U^2 \epsilon^2 = 1, \quad (4.75)$$

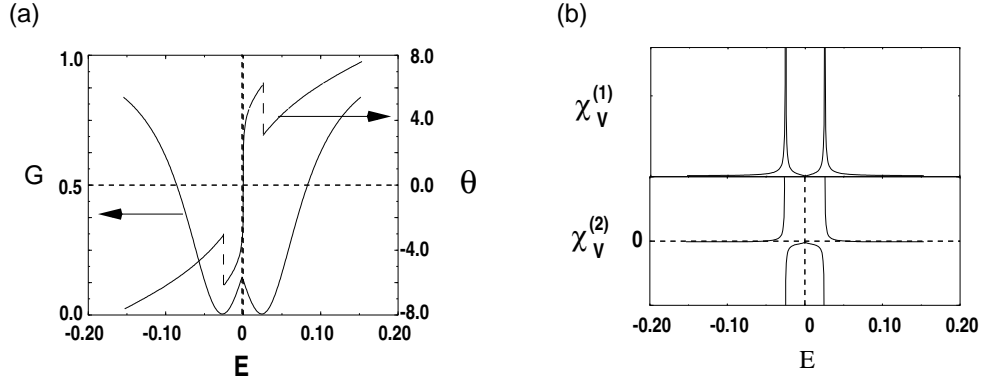


Figure 4.20: (a) The Fermi energy dependence of the conductance together with the phase of the transmission coefficient, within the single conducting channel region. Here a lattice vacancy is located at the 8A site of zigzag ribbon of  $N = 20$ . (b) The Fermi energy dependence of  $\chi_V^{(1)}$  and  $\chi_V^{(2)}$  of the same system.

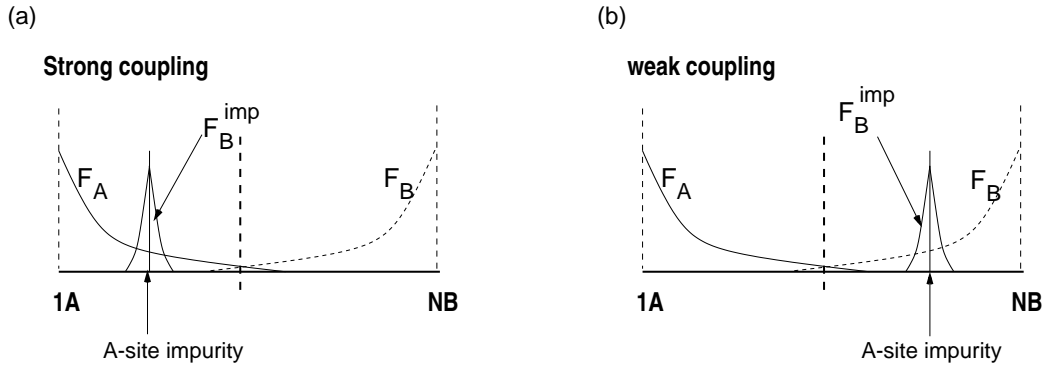


Figure 4.21: The schematic figures of the envelope functions for the zigzag ribbon with a single vacancy at A-site. The case of (a) strong coupling and (b) weak coupling.

Therefore,  $b_{\mathbf{k}} \propto \epsilon$ . In the limit of  $U \rightarrow \infty$ , i.e. the case of a lattice vacancy, from Eq.(4.73) a bound state appears at  $\epsilon = 0$ . In this limit, the nodes of the wavefunction lie on the B-sites, and only A-sites have amplitude, which is localized around the vacancy and decays exponentially. Thus, a single vacancy makes a bound state at  $E = 0$ . If the vacancy is located at the A(B)-sites, A(B)-sites are nodal site and the wave functions of B(A)-sites are localized around the vacancy and exponentially decay leaving from the vacancy. If the onsite potential energy  $U$  has finite value, the bound state energy deviate from zero.

### 4.3.2 Influence on transport properties

In this subsection, let us consider the transport properties of the zigzag ribbons with a single lattice vacancy, i.e. the onsite potential  $U = \infty$ . Here we fix the width of the zigzag ribbon at  $N=20$ . The variation of the ribbon width does not qualitatively change the properties discussed in the following.

In Fig.4.20, we show the Fermi energy dependence of the conductance for the zigzag ribbon with a vacancy at the 8A-site. As expected, the zero-conductance appears, where we can see clear  $\pi$ -phase jumps of the phase of the transmission coefficient. We can also see the clear divergence of  $\chi_V^{(1,2)}$  approaching each zero-conductance point. The reason why we have two zero-conductance points is simple: the vacancy at the 8A-site makes a impurity level whose charge density has amplitudes only at B-sublattice. This impurity state couples with the edge state coming from the 1st zigzag line, whose charge density has amplitudes on A-sublattice, and makes a bonding state and an anti-bonding state. These two levels correspond to the two zero-conductance points.

The amplitude of the edge states decays exponentially leaving from the edge. This character of the edge state causes that the strength of the coupling between an edge state and a single impurity state depends on the position of the impurity. In Fig.4.21, we show schematic figures of envelope functions for edge states and the single impurity state due to an A-site vacancy. The A-site vacancy makes an impurity state whose charge density is localized at B-sites near the impurity, while the amplitudes of wavefunction on A-sites are zero. Therefore, the

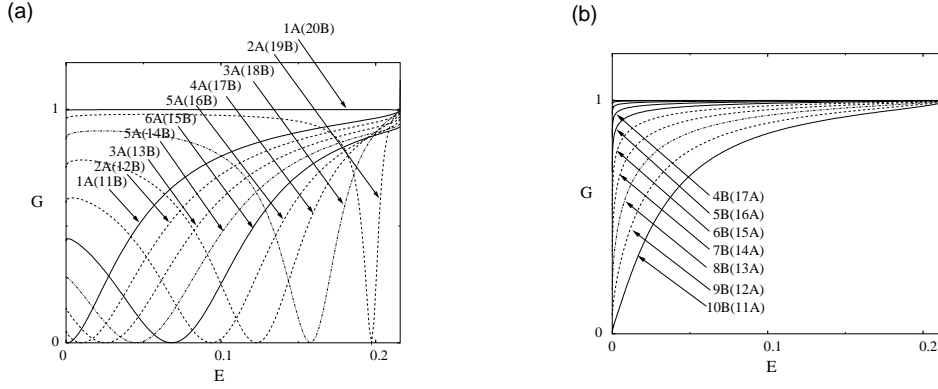


Figure 4.22: The Fermi energy dependence of the conductance of the zigzag ribbon with a single vacancy for (a) strong coupling case and (b) weak coupling case.

A-site vacancy located close to 1A-site, as shown in the Fig.4.21(a), the bonding and anti-bonding configuration is well developed, then the zero-conductance point will appear high energy. Let us call this situation strong coupling case. On the other hand, the A-site vacancy located close to NB-site, as shown in the Fig.4.21(b), the bonding and anti-bonding configuration is not well developed, then the zero-conductance point will appear near  $E = 0$ . Let us call this situation weak coupling case.

In Fig.4.22(a), it is shown the Fermi energy dependence of the conductance for various vacancy site in the strong coupling case. As expected, the position of the vacancy gets closer to 1A edge, the position of zero-conductance point appear higher energy. In Fig.4.22(b), we show the Fermi energy dependence of the conductance for the weak coupling case, where the bonding and bonding configuration is not well developed. Thus, the zero-conductance appears only around  $E = 0$ . Interestingly, the position of the vacancy gets closer to the edge, the system becomes almost ballistic.

## 4.4 Summary

In this chapter, we studied the transport properties of nanographite ribbon junctions, based on the Landauer approach.

A single edge state cannot contribute the electron transport due to the non-bonding character, however in the zigzag ribbon systems the bonding and anti-bonding configuration between two edge states can provide a single conducting channel. Firstly, we analyzed the single-barrier nanographite ribbon junctions, where we found the sharp zero-conductance dip structures when we changed the Fermi energy in the single-conducting channel region. We presented the interpretation of these conductance zeros in terms of the interference effects involving resonant transmission through resonant states characterized by (i) the formation of standing waves in the M-region, and (ii) the formation of the Kekulé-like current vortex pattern, i.e. flux states. This allows us to analyze the conductance zeros in terms of a quantum waveguide with a t-sub resonator. The conductance zeros can be interpreted by the interference of two conducting channels: (i) the conventional tunneling from left to right, and (ii) the resonant tunneling which takes a detour through the resonator.

Therefore, the non-magnetic impurity or a lattice vacancy can produce the conductance zeros accompanied with the flux states. In the cases of non-magnetic impurities, the energy points of the conductance zeros depends on the strength of overlapping between edge states and the impurity state.

---

## Chapter 5

# Conclusions and Outlooks

---

In this thesis, we have studied the various aspects of low-energy physical properties of nanosize carbon systems with open boundaries, called “nanographites”. We have found that the existence of graphite edges and their shapes strongly affects the  $\pi$  electronic states in nanosize carbon systems, and showed that nanographites form a new class of nanoscopic systems. Here I present the conclusions of this thesis and the outlook for the future studies.

- **Electronic properties**

The electronic states crucially depend on the topology of  $sp^2$  carbon networks, especially existence of the edges and their shapes. A remarkable feature is the appearance of the non-bonding edge localized states, “edge states”. The edge states appear at zigzag, bearded and cove edges, while they are completely absent for armchair edges. The condition of the edge states can be also discussed by the formal analogy to the condition of the Andreev bound states in anisotropic superconductors. According to these criteria, in general, edges which are not parallel to the armchair edge possess the non-bonding states. When the system size is of nanometer scale, the edge states make a sizable sharp peak at  $E = 0$  in the density of states. Since such peaks are completely absent in aromatic molecules, carbon nanotubes and bulk graphite, nanographites represent a class of nanoscopic systems with new characteristic properties.

- **Magnetic properties**

The sharp peak in the density of states due to edge states gives strong Pauli paramagnetic response at low-temperature. The Pauli paramagnetic susceptibility has the form of  $1/T^\alpha$  ( $\alpha = 1 - 1/N$ ). In the nanometer-size systems, this contribution competes with the orbital diamagnetic susceptibilities, so that the crossover from low-temperature paramagnetic to high-temperature diamagnetic response occurs. We have also shown the possibilities of spin polarization at the edges due to the electron-electron interactions. Thus our results show that nanographites have magnetic properties more complex than the aromatic molecules and bulk graphites which show only diamagnetic response.

- **Transport properties**

Because of the non-bonding character of the edge state, a single edge state cannot contribute to the electron transport. However, in zigzag ribbons, the edge states can provide a single conduction channel for electron transport due to the bonding and anti-bonding configuration of two edge states which overlap from the both edges. In the single-barrier systems of nanographite-ribbon junctions, the conductance shows rich structures as a function of the chemical potential, in contrast to the carbon nanotubes and usual quantum wire systems. A remarkable feature is the appearance of antiresonance conductance zeros. The origin of the conductance zeros is due to the interference of two channels in the junctions: one is the ordinary transmission through the junction and the other is a resonant channel in the junction. We also found that each conductance zero is connected with a resonant state; a standing wave which is the superposition of two degenerate flux states. The flux states, which are visible as the Kekulé-like current vortex pattern, are susceptible to the current in the vicinity of each conductance zero. Because the origin of the flux states is due to the intrinsic chiral feature of graphite, i.e. K and K' have opposite chirality, a single non-magnetic impurity or vacancy can introduce the flux states with zero-conductance dip. We

also found that each zero-conductance dips show pronounced negative magneto-resistance, because the zero-conductance originates from the time-reversal symmetry.

In spite of the long scientific and industrial history of the carbon-related materials, it is surprising that still many new physical properties can be found in the graphite systems. After the discovery of fullerene molecules and carbon nanotubes, much research effort has been devoted to nanosize carbon systems with closed boundaries, where many exotic electronic properties, have been found. However, our work has revealed that the existence of graphite edges and their shapes in nanosize carbon systems induce the quite different physical properties not only from bulk graphite and aromatic molecules but also from fullerene molecules and carbon nanotubes. Therefore, we conclude that nanographite systems form a new class of nanoscopic systems.

Our studies have not only revealed fundamental physical properties in nanosize carbon systems with open boundaries, but also show that the physics of nanographites can be connected to the fields of meso-, nanoscopic physics and anisotropic superconductivity. In the rest of this chapter, I will briefly discuss the outlooks for future studies on nanographites.

(1) Recent tremendous progress in the nanofabrication techniques has made it possible to develop the ultrasmall devices with nanometer-length scale. The promising goal of this research effort is the development of atomic or molecular scale electronic devices, which not only could increase the device density in an integrated circuit enormously, but also the operation principles of a single transistor could be fundamentally different from ordinary electronic devices [135, 136]. Actually, a three-terminal switching device that consists of one carbon nanotube was developed. As we have seen in the Chapter 4, nanographite ribbon junctions show very rich behavior of conductance as a function of the chemical potential. Since the chemical potential can be controlled by the gate voltage, these conductance features provide a wide range application of nanographite junctions for the electronic devices. For example, in a single barrier junction, a state can be switched from “on-state” of conducting state to “off-state” of conductance zeros, or vice versa, by controlling the gate voltage. A single barrier nanographite junction provides anti-resonance conductance zeros, however, we can also produce the resonance transmission in the double barrier nanographite junctions, in which the spacing between resonances can be controlled by the distance between two barriers. These pronounced features of resonant transmission can be used as carbon-based quantum dots. Thus, the nanographite junctions could serve as the carbon-based nanosize switching electronic devices.

(2) In the chapter 4, we have discussed the effect of short-range impurities on transport properties, where we find that the conductance depends on the position of the impurity. However we have to consider the weak onsite disorder problem in future in order to examine the possibilities of the application of nanographene ribbons as nano-quantum wires. Since the weak disorder problem is closely connected to the Anderson localization problem, it is interesting not only from viewpoint of technological application, but also from a purely scientific viewpoint.

(3) Although, in the nanosize carbon systems, the topology of the network is crucial for the electronic properties, recently the effects of electron correlations in carbon nanotubes is discussed based on the concept of Tomonaga-Luttinger liquids. As we have seen in the chapter 3, the mean field treatment of the electron correlation causes the opening of a small gap at the Fermi level with a spin polarization. Of course there is not real order in the one-dimensional system. However, this implies that there are possibilities that the electron correlation causes the significant influence on the low-energy magnetic and transport properties. This problem is quite challenging for future studies. Furthermore, it was reported recently that some fluorinated carbon systems induces a spin polarization, leading to the interaction between conduction electron and magnetic impurity, i.e. the Kondo problem.

(4) In the chapter 2, we have revealed that quasiparticle spectrum of the graphite can be viewed as that of an odd-parity (f-wave) superconductor within a formal analogy. Thus this system exhibits also a kind of Andreev reflection like superconductors though the “electron” and “hole” are different quasiparticles. It would be interesting to study the system in contact with superconductors. In particular, the Josephson effect through nanographite ribbons might have interesting new properties in mesoscopic systems.

Finally, we have investigated the low-energy physical properties of edge states in nanographite systems. We have found that nanographites form a new class of nanoscopic carbon systems due to the existence of the edge states, where the edge states play a crucial role in the electronic, magnetic and transport properties. Up to now, the manipulation of graphite in the nanoscale encounters various difficulties. However, the recent rapid progress of nano-fabrication techniques will allow for the control of graphite in the nanoscale. So I believe that our theoretical studies of the edge states will be confirmed in the next century.

# Bibliography

- [1] M. S. Dresselhaus, G. Dresselhaus, K. Sugihara, I. L. Spain, H. A. Goldberg, *Graphite Fibers and Filaments*, (Springer-Verlag, Berlin, 1988).
- [2] M. S. Dresselhaus, G. Dresselhaus, and P. C. Eklund, *Science of Fullerenes and Carbon Nanotubes*, (Academic Press, San Diego, 1996).
- [3] R. Saito, G. Dresselhaus, and M. S. Dresselhaus, *Physical Properties of Carbon Nanotubes*, (Imperial College Press, London, 1998).
- [4] S. Yoshimura, and R. P. H. Chan eds. *Supercarbon*, (Springer-Verlag, Berlin, 1998).
- [5] W. E. Billups, and M. A. Ciufolini eds., *Buckminsterfullerenes*, (VCH, 1993).
- [6] H. Ehrenreich, and F. Spaepen eds., *Solid State Physics*, **48**, (Academic Press, 1994).
- [7] O. Gunnarsson, *Superconductivity in fullerenes*, *Rev. Mod. Phys.* **69**, 575 (1997).
- [8] J. Robertson, *Amorphous carbon*, *Advances in Physics*, **35**, 317-374 (1986).
- [9] M. S. Dresselhaus, and G. Dresselhaus, *Intercalation Compounds of Graphite*, *Advances in Physics*, **30**, 139-326 (1981).
- [10] R. R. Haering, S. Mrozowski, *The Band Structure and Electronic Properties of Graphite Crystals*, *Prog. Semicond.* **5**, 274 (1960).
- [11] P. M. Ajayan, and T. W. Ebbesen, *Nanometre-size tubes of carbon*, *Rep. Prog. Phys.* **60**, 1025-1062 (1997).
- [12] C. Dekker, *Carbon Nanotubes as Molecular Quantum Wires*, *Physics Today* **52**, 22 (1999).
- [13] H. W. Kroto, J. R. Heath, S. C. O'Brien, R. F. Curl, R. E. Smalley, *Nature* **318**, 162 (1985).
- [14] W. Krätschmer, L. D. Lamb, K. Fostiropoulos, and D. R. Huffman, *Solid C<sub>60</sub>: a new form of carbon*, *Nature* **347**, 354 (1990).
- [15] S. Iijima, *Helical microtubules of graphitic carbon*, *Nature* **354**, 56 (1991).
- [16] R. Saito, M. Fujita, G. Dresselhaus and M. S. Dresselhaus, *Electronic structure of chiral graphene tubules*, *Appl. Phys. Lett.* **60**, 2204 (1992)
- [17] R. Saito, M. Fujita, G. Dresselhaus and M. S. Dresselhaus, *Electronic structure of graphene tubes based on C<sub>60</sub>*, *Phys. Rev. B* **46**, 1804 (1992).
- [18] N. Hamada, S. Sawada, and A. Oshiyama, *New One-Dimensional Conductors: Graphitic Microtubules*, *Phys. Rev. Lett.* **68**, 1579 (1992).
- [19] J. W. G. Wildöer, L. C. Venema, A. G. Rinzler, R. E. Smalley, and C. Dekker, *Electronic structure of atomically resolved carbon nanotubes*, *Nature* **391**, 59 (1998).
- [20] T. W. Odom, J. Huang, P. Kim, and C. M. Lieber, *Atomic structure and electronic properties of single-walled carbon nanotubes*, *Nature*, **391**, 62 (1998).
- [21] H. A. Schwartz, *Gesammelte Mathematische Abhandlungen*, (Springer, Berlin, 1890).
- [22] A. L. Mackay, *Periodic minimal surfaces*, *Nature* **314**, 604 (1985).

- [23] T. Lenosky, X. Gonze, M. Teter, and V. Elser, *Energetics of negatively curved graphitic carbon*, Nature **355**, 333 (1992).
- [24] D. Vanderbilt, and J. Tersoff, *Negative-curvature fullerene analog of C<sub>60</sub>*, Phys. Rev. Lett. **68**, 511 (1992).
- [25] A. L. Mackay, and H. Terrones, *Diamond from graphite*, Nature **352**, 762 (1991).
- [26] M. Fujita, M. Yoshida, and K. Nakada, *Polymorphism of Extended Fullerene Networks: Geometrical Parameters and Electronic Structures*, Fuller. Sci. Tech. **4**, 565 (1996).
- [27] M. Fujita, T. Umeda, and M. Yoshida, *Polymorphism of carbon forms: Polyhedral morphology and electronic structures*, Phys. Rev. B **51**, 13778 (1995).
- [28] N. Shima, and H. Aoki, *Electronic Structure of Superhoneycomb Systems: A Peculiar Realization of Semimetal/Semiconductor Classes and Ferromagnetism*, Phys. Rev. Lett. **71**, 4389 (1993).
- [29] K. Tanaka, S. Yamashita, H. Yamabe, and T. Yamabe, Synth. Met. **17**, 143 (1987).
- [30] H. Hosoya, Y.-D. Gao, K. Nakada, and M. Ohuchi, *Fundamental Analysis of the Topological Dependency of the Electronic Structure of Conductive Polymer Networks*, New Functionality Materials, Vol.C, Synthetic Process and Control of Functionality Materials, T. Tsuruta, M. Doyama, M. Seno (Eds.), Elsevier Science Publishers B. V., pp.27-34 (1993).
- [31] H. Hosoya, *Application of Graph Theory for Chemical Physics*, Kotai Butsuri (in Japanese), **32**, 549 (1997); **32**, 629 (1997); **32**, 721 (1997); **32**, 801 (1997); **32**, 884 (1997); **32**, 965 (1997); **33**, 10 (1998); **33**, 181 (1998); **33**, 523 (1998); **33**, 603 (1998).
- [32] M. Fujita, K. Wakabayashi, K. Nakada, and K. Kusakabe, *Peculiar localized state at zigzag graphite edge*, J. Phys. Soc. Jpn. **65**, 1920 (1996).
- [33] P. R. Wallace, *The Band Theory of Graphite*, Phys. Rev. **71**, 622 (1947).
- [34] C. A. Coulson, and R. Taylor *Studies in Graphite and Related Compounds I: Electronic Band Structure in Graphite*, Proc. Phys. Soc. Lond. **A65**, 815 (1952).
- [35] C. A. Coulson, *Energy Bands in Graphite*, Nature **159**, 265 (1947).
- [36] W. M. Lomer, *The valence bands in two-dimensional graphite*, Proc. Roy. Soc. (L), **A227**, 330 (1955).
- [37] J. C. Slonczewski, and P. R. Weiss *Band Structure of Graphite*, Phys. Rev. **109**, 272 (1958).
- [38] K. Kobayashi, *Electronic structure of a stepped graphite surface*, Phys. Rev. B **47**, 1757 (1993)
- [39] K. Nakada, M. Fujita, G. Dresselhaus, and M. S. Dresselhaus, *Edge state in graphene ribbons: Nanometer size effect and edge shape dependence*, Phys. Rev. B **54**, 17954 (1996).
- [40] Y. Takagi, M. Fujita, and K. Kusakabe, *Novel semimetallic superstructure: Hyper Graphite*, Mol. Cryst. Liq. Cryst. ( in press ).
- [41] Y. Takagi, M. Fujita, K. Wakabayashi, M. Igami, S. Okada, K. Nakada, and K. Kusakabe, *The Hyper-graphite: A possible extension of graphitic network*, cond-mat/0001027.
- [42] K. Kaneko, Solid State Physics ( *Kotai Butsuri*, in Japanese ), **27**, 403 (1992).
- [43] K. Kaneko, C. Ishii, M. Ruike, and H. Kuwabara, Carbon **30**, 1075 (1991).
- [44] M. S. Dresselhaus, A. W. P. Fung, A. M. Rao, S. L. di Vittorio, K. Kuriyama, G. Dresselhaus, and M. Endo, Carbon **30**, 1065 (1992).
- [45] A. Nakayama, K. Suzuki, T. Enoki, C. Ishii, K. Kaneko, M. Endo, and N. Shindo, *Anomalous helium-gas-induced energy relaxation and the evidence for ultra micropores in microporous carbon*, Solid State Comm., **93**, 323 (1995).
- [46] A. W. P. Fung, M. S. Dresselhaus, and M. Endo, *Transport properties near the metal-insulator transition in heat-treated activated carbon*, Phys. Rev. B **48**, 14953 (1993).
- [47] A. W. P. Fung, Z. H. Wang, M. S. Dresselhaus, G. Dresselhaus, R. W. Pekala, and M. Endo, *Coulomb-gap magnetotransport in granular and porous carbon structures*, Phys. Rev. B **49**, 17325 (1994).

- [48] A. Nakayama, K. Suzuki, T. Enoki, K. Koga, M. Endo, and N. Shindo, *Electronic and Magnetic Properties of Activated Carbon Fibers*, Bull. Chem. Soc. Jpn. **69**, 333 (1996).
- [49] A. Nakayama, *Study on Magnetic and Electronic Properties of Activated Carbon Fiber*, Doctor Thesis, Department of Chemistry, Tokyo Institute of Technology, (1996).
- [50] A. Nakayama, K. Suzuki, T. Enoki, S. L. di Vittorio, M. S. Dresselhaus, K. Koga, M. Endo and N. Shindo, *Magnetic Properties of Activated Carbon Fibers*, Synth. Met. **55-57**, 3736 (1993).
- [51] Y. Shibayama, *Structure and Electronic Properties of Nano-Graphites, and Their Iodine Doping Effects*, Doctor Thesis, Department of Chemistry, Tokyo Institute of Technology, (2000).
- [52] Y. Shibayama, H. Sato, T. Enoki, and M. Endo, *Spin Glass Behavior at the Metal-Insulator Threshold in Nano-Graphite-Based Carbon Materials*, submitted to Phys. Rev. Lett.
- [53] Y. Shibayama, H. Sato, T. Enoki, X.-X. Bi, M. S. Dresselhaus, and M. Endo, *Novel Electronic Properties of a Nano-Graphite Disordered Network and Their Iodine Doping Effects*, submitted to J. Phys. Soc. Jpn.
- [54] T. Enoki, Y. Shibayama, B. L. V. Prasad, and H. Sato, *Nano-Graphite and its Intercalation Compounds*, Proceeding of the 4th Int. Russian Workshop on Fullerenes and Atomic Clusters, St. Petersburg, Oct. (1999).
- [55] O. E. Andersson, B. L. V. Prasad, H. Sato, T. Enoki, Y. Hishiyama, Y. Kaburagi, M. Yoshikawa, S. Bandow, *Structure and electronic properties of graphite nanoparticles*, Phys. Rev. B, **58**, 16387 (1998).
- [56] Y. Nishi, *Carbonaceous Materials for Lithium Ion Battery Anodes*, Mol. Cryst. Liq. Cryst. ( in press ).
- [57] A. Yoshino, *Development of Lithium Ion Battery*, Mol. Cryst. Liq. Cryst. ( in press ).
- [58] T. Nagaura, and T. Tozawa, Prog. Batteries Sol. Cells, **9**, 315 (1990).
- [59] M. Noguchi, K. Miyashita, M. Endo, Tanso, **155**, 315 (1992).
- [60] K. Sato, M. Noguchi, A. Demachi, N. Oki, and M. Endo, *A Mechanism of Lithium Storage in Disordered Carbons*, Science **264**, 556 (1994).
- [61] M. Yagi, R. Saito, T. Kimura, G. Dresselhaus, and M. S. Dresselhaus, *Excess Li Ions in a Small Graphite Cluster*, J. Mater. Res. **12**, 1367 (1997).
- [62] M. Yagi, R. Saito, T. Kimura, G. Dresselhaus, and M. S. Dresselhaus, *Electronic States in Heavily Li-doped Graphite Nanoclusters*, J. Mater. Res. No. 9 (1999).
- [63] K. Takai, H. Sato, T. Enoki, N. Yoshida, F. Okino, H. Tohara, and M. Endo, *Fluorine-introduced  $sp^3$ -carbon sites in a nano-sized  $\pi$ -electron conjugated system and their effect on the electronic properties*, Mol. Cryst. Liq. Cryst. ( in press ).
- [64] R. Saito, M. Yagi, T. Kimura, G. Dresselhaus, and M. S. Dresselhaus, *Chemical Reaction of Intercalated Atoms at the Edge of Nano-Graphene Cluster*, Mol. Cryst. Liq. Cryst. ( in press ).
- [65] T.W. Ebbesen, and H. Hiura, *Graphene in 3-Dimension: Towards Graphite Origami*, Adv. Mater., **7**, 582-586 (1995).
- [66] H. Hiura, T. W. Ebbesen, J. Fujita, K. Tanigaki, and T. Takada, *Role of  $sp^3$  defect structures in graphite and carbon nanotubes*, Nature **367**, 148 (1994).
- [67] H. Hiura, Spring Meeting of the Physical Society of Japan, Meijo University, March, Nagoya (1997); private communication.
- [68] A. Nagashima, H. Itoh, T. Ichinokawa, C. Oshima, and S. Otani, *Change in the electronic states of graphite overlayers depending on thickness*, Phys. Rev. B **50**, 4756 (1994).
- [69] M. Terai, N. Hasegawa, M. Okusawa, S. Otani, and C. Oshima, *Electronic states of monolayer micrographite on TiC(111)-faceted and TiC(410) surfaces*, Appl. Sur. Sci. **130-132**, 876 (1998).
- [70] C. Oshima, private communication.
- [71] R. Peierls, *Zur Theorie des Diamagnetismus von Leitungselektronen*, Z. Phys. **80**, 763 (1933)

- [72] F. London, *Theorie quantique des courants interatomiques dans les combinaisons aromatiques*, J. Phys. Rad. **8**, 397 (1937).
- [73] P. G. Harper, Proc. Phys. Soc. Lond. A **68**, 874 (1955)
- [74] W. Y. Hsu, and L. M. Falicov, *Level quantization and broadening for band electrons in a magnetic field: Magneto-optics throughout the band*, Phys. Rev. B **13**, 1595 (1976).
- [75] J. M. Luttinger, *The Effect of a Magnetic Field on Electrons in a Periodic Potential*, Phys. Rev. **84**, 814 (1951).
- [76] W. Kohn, *Theory of Bloch Electrons in a Magnetic Field: The Effective Hamiltonian*, Phys. Rev. **115**, 1460 (1959).
- [77] J. W. McClure, *Diamagnetism of Graphite*, Phys. Rev. **104**, 666 (1956).
- [78] H. Ajiki and T. Ando, *Electronic states of carbon nanotubes*, J. Phys. Soc. Jpn. **62**, 1255 (1993).
- [79] H. Ajiki and T. Ando, *Energy Bands of Carbon Nanotubes in Magnetic Fields*, J. Phys. Soc. Jpn. **65**, 505 (1996).
- [80] H. Ajiki, Carbon Nanotubes in Magnetic Fields, Doctor Thesis, Department of Physics, University of Tokyo (1995).
- [81] E. I. Blount, *Bloch Electrons in a Magnetic Field*, Phys. Rev. **126**, 1636 (1962).
- [82] G. H. Wannier, *Dynamics of Band Electrons in Electric and Magnetic Fields*, Rev. Mod. Phys. **34**, 645 (1962).
- [83] R. Rammal, *Landau level spectrum of Bloch electrons in a honeycomb lattice*, J. Phys. **46**, 1345 (1985).
- [84] D. R. Hofstadter, *Energy levels and wave functions of Bloch electrons in rational and irrational magnetic fields*, Phys. Rev. B **14**, 2239 (1976).
- [85] G. H. Wannier, *A Result Not Dependent on Rationality for Bloch Electrons in a Magnetic Field*, Phys. Stat. Sol. (B) **88**, 757 (1978).
- [86] G. H. Wannier, *Energy Spectrum for Bloch Electrons in a Magnetic Field*, Int. J. Quantum. Chem., **13**, 413 (1979).
- [87] F. H. Claro, and G. H. Wannier, *Magnetic subband structure of electrons in hexagonal lattices*, Phys. Rev. B **19**, 6068 (1979).
- [88] H. Aoki, M. Ando, and H. Matsumura, *Hofstadter butterflies for flat bands*, Phys. Rev. B **54**, R17296 (1996).
- [89] M. Kohmoto, *Zero modes and the quantized Hall conductance of the two-dimensional lattice in a magnetic field*, Phys. Rev. B **39**, 11943 (1989).
- [90] Y. Hatsugai, and M. Kohmoto, *Energy spectrum and the quantum Hall effect on the square lattice with next-nearest-neighbor hopping*, Phys. Rev. B **42**, 8282 (1990).
- [91] D. Langbein, *The Tight-Binding and the Nearly-Free-Electron Approach to Lattice Electrons in External Magnetic Fields*, Phys. Rev. **180**, 633 (1969).
- [92] W. G. Chambers, *Linear-Network Model for Magnetic Breakdown in Two Dimensions*, Phys. Rev. **140**, A135 (1965).
- [93] H. W. Capel, *On the Broadening of Landau Levels*, Physica, **54**, 361 (1971).
- [94] K. Nakao, *Landau Level Structure and Magnetic Breakthrough in Graphite*, J. Phys. Soc. Jpn. **40**, 761 (1976).
- [95] A. H. MacDonald, *Edge states and quantized Hall conductivity in a periodic potential*, Phys. Rev. B **29**, 6563 (1984).
- [96] Y. Hatsugai, *Edge states in the integer quantum Hall effect and the Riemann surface of the Bloch function*, Phys. Rev. B **48**, 11851 (1993).

- [97] R. Rammal, G. Toulouse, M. T. Jaekel and B. I. Halperin, *Quantized Hall conductance and edge states: Two-dimensional strips with a periodic potential*, Phys. Rev. B **27**, 5142 (1983).
- [98] C. R. Hu, *Midgap surface states as a novel signature for  $d_{x^2-y^2}$ -wave superconductivity*, Phys. Rev. Lett. **72**, 1526 (1994).
- [99] Y. Tanaka, and S. Kashiwaya, *Theory of Tunneling Spectroscopy of d-Wave Superconductors*, Phys. Rev. Lett. **74**, 3451 (1995).
- [100] M. Sigrist, *Time-Reversal Symmetry Breaking States in High-Temperature Superconductors*, Prog. Theor. Phys. **99**, 899 (1998).
- [101] P. G. de Gennes, *Superconductivity of Metals and Alloys*, Chapter 5, (Benjamin, New York, 1966).
- [102] A. F. Andreev, Sov. Phys-JETP, **19**, 1228 (1964).
- [103] K. Wakabayashi, M. Fujita, H. Ajiki, and M. Sigrist, *Electronic and magnetic properties of nanographite ribbons*, Phys. Rev. B **59**, 8271 (1999).
- [104] R. M. White, *Quantum Theory of Magnetism*, (Springer-Verlag).
- [105] J. P. Lu, *Novel magnetic properties of carbon nanotubes*, Phys. Rev. Lett. **74**, 1123 (1995).
- [106] H. Ajiki, and T. Ando, *Magnetic Properties of Carbon Nanotubes*, J. Phys. Soc. Jpn. **62**, 2470 (1993).
- [107] M. Fujita, M. Igami and K. Nakada, *Lattice distortion in nanographite ribbons*, J. Phys. Soc. Jpn. **66** (1997) 1864.
- [108] Y. Miyamoto, K. Nakada, and M. Fujita, *First-principles study of edge states of H-terminated graphitic ribbons*, Phys. Rev. B **59**, 9858 (1999) [Errata: **60**, 16211 (1999)].
- [109] E. H. Lieb, *Two theorems on the Hubbard model*, Phys. Rev. Lett. **62**, 1201 (1989) [Errata: **68**, 1927 (1989)].
- [110] L. Pitaevskii and S. Stringari, J. Low. Temp. Phys. **85**, 377 (1991).
- [111] For a review see E. Dagotto and T.M. Rice, *Surprises on the way from one- to two-dimensional quantum magnets: The ladder materials*, Science **271** (1996) 618.
- [112] T. Moriya, *Spin Fluctuations in Itinerant Electron Magnetism*, (Springer-Verlag).
- [113] K. Wakabayashi, and M. Sigrist, *Zero-Conductance Resonances due to Flux States in Nanographite Ribbon Junctions*, Phys. Rev. Lett. (in press).
- [114] P. W. Anderson, D. J. Thouless, E. Abrahams, D. S. Fisher, *New method for a scaling theory of localization*, Phys. Rev. B **22**, 3519 (1980).
- [115] M. Büttiker, Y. Imry, R. Landauer, and S. Pinhas, *Generalized many-channel conductance formula with application to small rings*, Phys. Rev. B **31**, 6207 (1985).
- [116] R. Landauer, *Electrical Transport in Open and Closed Systems*, Z. Phys. B **68**, 217 (1987).
- [117] Y. Imry, *Introduction to Mesoscopic Physics*, (Oxford University Press, 1997).
- [118] S. Datta, *Electronic Transport in Mesoscopic Systems*, (Cambridge University Press, 1995).
- [119] H. Fukuyama eds., *Physics in Mesoscopic Systems* (in Japanese), (Maruzen, 1996).
- [120] S. Kurihara eds., *Tunnelling Effects* (in Japanese), (Maruzen, 1994).
- [121] T. Ando eds., *Quantum Effect and Magnetic Field* (in Japanese), (Maruzen, 1995).
- [122] A. Kawabata, *Physics in Mesoscopic Systems* (in Japanese), (Baifukan, 1997).
- [123] A. M. Zagoskin, *Quantum Theory of Many-Body Systems* (Springer-Verlag, 1998).
- [124] P.A. Lee, and D.S. Fisher, *Relation between conductivity and transmission matrix*, Phys. Rev. B **47**, 882 (1981).

- [125] A. MacKinnon, *Z. Phys. B* **59**, 385 (1985).
- [126] T. Ando, *Quantum point contacts in magnetic fields*, *Phys. Rev. B* **44**, 8017 (1991).
- [127] T. Nakanishi, *Informal seminar on the recursive Green function techniques and the transport properties of carbon nanotubes*, Institute of Materials Science, Tsukuba University, Nov. (1997).
- [128] R. Tamura, and M. Tsukada, *Analysis of quantum conductance of carbon nanotube junctions by the effective-mass approximation*, *Phys. Rev. B* **58**, 8120 (1998).
- [129] P. S. Deo, and A. M. Jayannavar, *Quantum waveguide transport in serial stub and loop structures*, *Phys. Rev. B* **50**, 11629 (1994).
- [130] R. Sordan, and K. Nikolić, *Quantum interference resonator: Effects of disorder*, *Phys. Rev. B* **52**, 9007 (1995).
- [131] Z. Shao, W. Porod, and C. S. Lent, *Transmission resonances and zeros in quantum waveguide systems with attached resonators*, *Phys. Rev. B* **49**, 7453 (1994).
- [132] H. Xu, and W. Sheng, *Discontinuity in the phase evolution of electron transport in a quantum channel with attached quantum dots*, *Phys. Rev. B* **57**, 11903 (1998).
- [133] M. Büttiker, Y. Imry, and M. Ya. Azbel, *Quantum oscillations in one-dimensional normal-metal rings*, *Phys. Rev. A* **30**, 1982 (1984).
- [134] W. Porod, Z. Shao, and C. S. Lent, *Resonance-antiresonance line shape for transmission in quantum waveguides with resonantly coupled cavities*, *Phys. Rev. B* **48**, 8495 (1993).
- [135] R. P. Feynman, *Science*, **254**, 1300, (1991).
- [136] L. Kouwenhoven, *Single-Molecule Transistors*, *Science*, **275**, 1896, (1997).

# Curriculum Vitae

- 4/1995-present    Doctoral Program in Engineering, University of Tsukuba, Japan
- 1/2000    Dissertation on  
*Low-Energy Physical Properties of Edge States in Nano-Graphites*
- 8/1999    Invited talk at the 22nd Conference on Low Temperature Physics,  
entitled *Transport Properties of Nanographite Ribbon Junctions*
- 9/1998-present    Graduated student exchange program,  
at the Yukawa Institute for Theoretical Physics, Kyoto University, Japan
- 5/1998-8/1998    Atom researcher at the Yukawa Institute for Theoretical Physics,  
Kyoto University, Japan
- 8/1996    Financial Support from the Foundation Advanced Technology Institute, Japan
- 4/1996-present    Research Fellow of the Japan Society for the Promotion of Science
- 2/1997    Master in engineering, thesis on  
*Magnetic Properties of Nanographites*,  
with Prof. Mitsutaka Fujita
- 8/1996-9/1996    Visiting scientist, at the Institute for Theoretical Physics,  
Eidgenössische Technische Hochschule (ETH), Zürich, Switzerland
- 4/1991-3/1995    The College of Engineering Sciences,  
Third Cluster, University of Tsukuba, Japan
- 2/1995    Bachelor in engineering
- 18/12/1972    Born in Nara, Japan



# List of Publications

## Regular Article

- K. Wakabayashi, and M. Sigrist,  
*Zero-Conductance Resonances due to Flux States in Nanographite Ribbon Junctions*,  
Phys. Rev. Lett. in press, cond-mat/9907212.
- K. Wakabayashi, M. Fujita, H. Ajiki, and M. Sigrist  
*Electronic and Magnetic Properties of Nanographite Ribbons*,  
Phys. Rev. B. 59 (1999) 8271.
- K. Wakabayashi, M. Sigrist, and M. Fujita,  
*Spin Wave Mode of Edge-Localized Magnetic States in Nanographite Zigzag Ribbons*,  
J. Phys. Soc. Jpn. **67** 2089 (1998).
- C. Honerkamp, K. Wakabayashi, and M. Sigrist,  
*Instabilities at [110] Surfaces of  $d_{x^2-y^2}$  Superconductors*,  
Euro. Phys. Lett. submitted, cond-mat/9902026.
- M. Fujita, K. Wakabayashi, K. Nakada, and K. Kusakabe,  
*Peculiar Localized State at Zigzag Graphite Edge*,  
J. Phys. Soc. Jpn. **65**, 1920 (1996).
- Y. Takagi, M. Fujita, K. Wakabayashi, M. Igami, S. Okada, K. Nakada, and K. Kusakabe  
*The Hypergraphite: A possible extension of graphitic network*,  
Phys. Rev. B, submitted, cond-mat/0001027

## Conference Proceeding

- K. Wakabayashi, and M. Sigrist  
*Electronic Transport through Nanographite Ribbon Junctions*,  
Physica B, in press.
- K. Wakabayashi, M. Fujita, H. Ajiki, and M. Sigrist  
*Magnetic Properties of Nano-graphites at Low Temperature*,  
Physica B, in press.
- K. Wakabayashi,  
*Transport and Magnetic Properties of Nanographites*,  
Mol. Cryst. Liq. Cryst., in press.
- K. Wakabayashi, M. Igami, Y. Takagi, S. Okada, M. Fujita, K. Nakada and K. Kusakabe,  
*Novel electronic properties of nanographite, hypergraphite and topological defects*,  
Proceeding of 24th International Conference on Physics of Semiconductor,  
Aug. 1998. Jerusalem, Israel., published by World Scientific Singapore, March, 1999.

- K. Wakabayashi, M. Fujita, K. Kusakabe, and H. Ajiki,  
*Magnetic Field Effect on Graphite Ribbons*,  
J. Mag. Mat., **177-181** 1494-1485 (1998).
- K. Wakabayashi, M. Fujita, K. Kusakabe, and K. Nakada,  
*Magnetic Structure of Graphite Ribbon*,  
Czech. J. Phys., **46** 1865(1996).
- K. Wakabayashi, M. Fujita, K. Nakada, and K. Kusakabe,  
*Electronic and Magnetic Structure of Micro-Graphite*,  
Transactions of the Materials Reserch Society of Japan, Vol.20, 490(1996).
- K. Nakada, M. Fujita, K. Wakabayashi, and K. Kusakabe,  
*Localized electronic states on graphite edge*,  
Czech. J. Phys., **46** 2429(1996).
- K. Kusakabe, K. Wakabayashi, M. Igami, K. Nakada, and M. Fujita,  
*Magnetism of Nanometer-Scale Graphite with Edge or Topological Defects*,  
Molecular Crystals and Liquid Crystals, **305** (1997) 445-454.
- M. Fujita, M. Igami, K. Wakabayashi, and K. Nakada,  
*Electron-Phonon and Electron-Electron Interactions in Nanographite Ribbons*,  
Mol. Cryst. Liq. Cryst., 310, 173-178 (1998).
- K. Nakada, M. Igami, K. Wakabayashi, and M. Fujita,  
*Localized  $\pi$  Electronic Edge State in Nanographite*,  
Mol. Cryst. Liq. Cryst., 310, 225-230 (1998).

### Japanese Articles

- M. Fujita, K. Wakabayashi, M. Igami, K. Nakada, and K. Kusakabe,  
*Electronic Properties of Nanographite*, *Kotai Butsuri* **32** (1997) 179 – 188.
- M. Fujita, M. Igami, K. Wakabayashi K. Nakada, and K. Kusakabe,  
*Edges and Defects in Graphites*,  
*Hyoumen Kagaku* **19** (1998) 35-42